THE UNIVERSITY OF CHICAGO

NONLINEAR X-RAY PROPAGATION PHENOMENA IN DENSE GASES

A DISSERTATION SUBMITTED TO
THE FACULTY OF THE DIVISION OF THE PHYSICAL SCIENCES
IN CANDIDACY FOR THE DEGREE OF
DOCTOR OF PHILOSOPHY

DEPARTMENT OF PHYSICS

BY
KAI LI

CHICAGO, ILLINOIS
DECEMBER 2023

For my parents

Nature is a piece of art

that will always surprise you with its beauty.

TABLE OF CONTENTS

LIST OF FIGURES

ACKNOWLEDGMENTS

I would like to thank my supervisor Prof. Linda Young for taking me as her PhD student and giving me the opportunity to work on this exciting project. It has been a wonderful journey these past five years and I have learned so much not only on the specific project but also on how to attack problems and how to do research. Her ways of thinking and living have been a real encouraging model in my career. I highly appreciate her patience and kind support these years.

I would also like to take this opportunity to thank all the members of our AMO group at Argonne National Laboratory. The people I have worked with: Phay J. Ho, Gilles Doumy, Stephen H. Southworth, Anne Marie March, Shuai Li, Eetu Pelimanni, Adam E A Fouda, Christopher J. Otolski, and Dimitris Koulentianos. It has been a pleasure to work with you and I have a lot of fun discussing with you all.

I would also like to thank our cooperators around the world: Mette Gaarde, Marie Labeye, Michael Meyer, Jan-Erik Rubensson, Marc Simon, Thomas Pfeifer, Christian Ott, Nina Rohringer, Marcus Agaker, Tommaso Mazza, Joakim Laksman, Alberto DeFaris, Alex Magunia, Marc Rebholz and the team at European XFEL and LCLS. Without the help from you, the research would not be possible.

I am thankful to my classmates at UChicago. It has been a great time to learn, discuss, and live with you all. Thanks to the people in the physics department who have supported the PhD program. Special thanks to Kwang-Je Kim who has encouraged and helped me to apply to this program, and I am glad I could be part of it.

I am very grateful for all the help from my family and friends. Especially my wife and our son, who have tremendously supported me to complete this PhD.

ABSTRACT

The last decades have witnessed the thriving investigation into understanding fundamental light-matter interactions and a rapid advance in atomic molecular, and optical experimental techniques. Nonlinear phenomena enabled by intense light sources in the optical, infrared, and microwave regions have been utilized to control electronic, nuclear, and spin degrees of freedom which have led to breakthroughs across many fields of science, such as medical imaging, telecommunication, and the creation and manipulation of novel materials. The advent of X-ray free-electron lasers (XFELs) offers unprecedented high-intensity x-ray pulses, thus opening the pathway to nonlinear light-matter interaction in the x-ray regime. The successful observation of several nonlinear x-ray optical phenomena and the emerging techniques based on nonlinear x-ray physics have suggested that transferring nonlinear optics to x-ray regimes is a feasible and fruitful approach.

The sub-femtosecond XFEL pulses are suitable for tracking ultrafast molecular dynamics via pump-probe techniques. In contrast to the optical photons, which mainly interact with the valence electrons, the high-energy x-ray photons interact strongly with the core electrons, which provides elemental sensitivity and site specificity. with these unique properties, XFELs have long promised the observation of ultrafast electronic motions in complex materials at their natural timescales with atomic resolution.

Among these new techniques, stimulated x-ray Raman scattering (SXRS) is an essential building block of x-ray nonlinear spectroscopy. Unlike the x-ray absorption and emission spectroscopies, whose bandwidth is limited by the ultrafast lifetime of core-excited states, the SXRS energy resolution is determined by the incident pulse. Similar to the optical femtosecond stimulated Raman spectroscopy, attosecond SXRS with XFELs can simultaneously achieve the sub-femtosecond time resolution as well as sub-lifetime energy resolution. These unique properties make attosecond SXRS a powerful tool to probe the long-range charge transfer and electronic coherences through a conical intersection.

In this thesis, the resonant propagation of XFEL pulses through a dense medium is studied theoretically and experimentally. A three-dimensional model, which solves the coupled time-dependent Schrodinger equation and Maxwell wave equation, is developed for simulating the resonant propagation process. Interesting nonlinear x-ray phenomena such as exponential growth of SXRS and x-ray lasing signal by eight orders of magnitude are observed. The x-ray self-induced transparency and self-focusing are also predicted. The simulations with XFEL pulses supported a proposal that was accepted by European XFEL. An experiment of SASE XFEL resonant propagation through dense neon gas was performed. The transmitted SASE and stimulated emission spectrum were measured by a grating spectrometer after the gas cell. The novel method of covariance analysis gives the SXRS with unprecedented energy resolution. Supercomputer simulations confirmed our observations and provided insights into SXRS. As a result of these insights, a suggested approach to further improve the SXRS spectrum is by including information of the incident SASE spectrum. A demonstration of the ghost-imaging (GI) method to non-invasively characterize the single-shot SASE spectrum was carried out in the European XFEL SQS (Small Quantum System endstation). The correlations between the photoelectron spectrum (PES) and grating spectrum were used in the GI formula to extract a response matrix for the PES array, which can then be applied to obtain a prediction of the SASE spectrum with higher energy resolution.

The work done in this thesis has improved the small spontaneous XRS signals by orders of magnitude through stimulated amplification in a dense medium, and it has lessened the requirements for narrow bandwidth coherent X-ray beams by taking advantage of the correlation properties in stochastic SASE pulses. The high-resolution SXRS spectrum achieved here is expected to contribute to the development of nonlinear x-ray spectroscopy using XFELs.

CHAPTER 1

INTRODUCTION

X-ray free-electron lasers (XFEL) generate high-intensity x-ray pulses with brightness ten orders of magnitude larger than synchrotron radiation. XFELs have opened the pathway to explore nonlinear light-matter interaction in the x-ray regime. The sub-femtosecond XFEL pulse duration combined with continuously tunable wavelength in the soft and hard x-ray regimes makes it a promising tool to explore ultrafast electronic dynamics. Several demonstrations of nonlinear x-ray phenomena with XFEL have proved that extending the existing optical nonlinear techniques to x-ray regimes is a feasible and fruitful path. Transferring nonlinear optical spectroscopic techniques to x-ray regimes would not only enable the tracking of ultrafast molecular dynamics on their natural femtosecond time scale but also provide atomic scale spatial resolution since the x-ray resonantly interacts with core electrons whose energy is element sensitive.

One of the essential building blocks of nonlinear x-ray spectroscopy is stimulated x-ray Raman scattering (SXRS) which promises the simultaneous achievement of sub-femtosecond temporal and sub-core-hole lifetime energy resolution. Unlike the x-ray absorption and emission spectroscopies, x-ray Raman scattering promotes an electron from the ground state to a meta-stable valence-excited state whose lifetime is much longer than core-excited states. As confirmed with optical Raman (Kukura et al. [2007]), the energy resolution of SXRS should be limited by the incident pulse bandwidth instead of the ultrashort core-excited states lifetime. The x-ray Raman scattering cross-section, however, is extremely small. To achieve a bigger signal, the exponentially amplified SXRS through the dense medium has been demonstrated to provide eight orders of magnitude amplification from the spontaneous Raman scattering (Weninger et al. [2013]).

The attosecond SXRS was proposed to follow the long-range ultrafast charge transfer in complex systems such as proteins (Zhang et al. [2014]). With the TRUECARS (Transient redistribution of ultrafast electronic coherences in attosecond Raman signals) technique, the electronic coherence at conical intersections can be measured free from backgrounds. To circumvent the requirements of the multiple delay controllable coherent x-ray pulses, the novel covariance analysis method that takes advantage of the correlation between the SASE spectrum and the SXRS is proposed and explored (Cavaletto et al. [2021]).

1.1 Free-electron laser

A free-electron laser (FEL) is a light source that generates high-brightness radiation with variable wavelengths from terahertz to hard x-rays (Huang and Kim [2007], Kim [1986b]). FELs were conceived by John Madey (Madey [1971]) and subsequently demonstrated experimentally by his group at Stanford University in the 1970s (Deacon et al. [1977]). The world's first x-ray FEL - Linac Coherent Light Source (LCLS) - generated its first light in 2009 (Emma et al. [2010]). Since then several other XFELs around the world have been built or proposed.

Instead of producing stimulated emission from bound electrons in atoms, molecules, or materials, as in the case of optical lasers, the radiation in FEL comes from high-energy free-electron beams. FELs usually contain an electron gun, where a metal target is photoionized by a laser beam to generate high-brightness electron beams. The electron beams then pass through a linear accelerator to gain energy from microwave fields. The relativistic electron beams then go through periodic magnetic fields, i.e. undulator or wiggler, and photons are generated by the motion with acceleration in the undulators.

An FEL produces light pulses with ten orders of magnitude higher brightness compared to the previous generation of light sources, i.e. synchrotron radiation. The reason for the high-intensity radiation is mainly due to the coherent stimulated emission from the bunched electron beams, instead of spontaneous radiations from individual electrons. The electron beams entering the undulator are deflected transversely in the magnetic fields and spon-

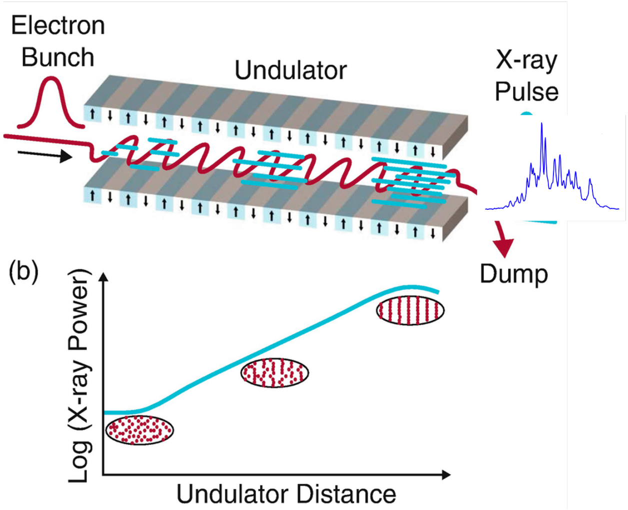

Figure 1.1: The schematic electron beam passing the undulator and the x-ray pulse energy grow exponentially due to the formation of micro-bunching. Figure adapted from Bostedt et al. [2016].

taneous radiation is produced due to the acceleration. The initial spontaneous radiation interacts with the electrons within the undulator. If the resonance relation is satisfied, the electron beam will develop microbunching structures at the radiation wavelength, and stimulated coherent emission starts. This means that the radiation fields from the different electrons constructively interfere with each other thus generating strong FEL pulses (Kim et al. [2017]).

The radiation wavelength λ_r of an FEL is determined by the resonant relation (Pellegrini and Reiche [2004]):

$$\lambda_r = \frac{\lambda_u}{2\gamma^2}\left(1 + \frac{K^2}{2}\right) \tag{1.1}$$

where λ_u is the periodic of the undulator magnetic fields; γ is the relativistic Lorentz factor of electron beams; K is a dimensionless parameter that relates to the undulator strength. For undulators made by permanent magnets, which generate magnetic fields with a strength of a few Tesla and the K factor is usually of the order of 1. The magnetic field period is around a few centimeters determined by the size of the magnets. The electron beam energy varies from MeV to GeV, which gives a relativistic factor up to $\gamma \sim 10^4$. The radiation wavelength could reach around 0.1 nm according to the FEL resonant equation (1.1). The gap between the magnets is designed to be adjustable, thus the field strength or K value is changed and the wavelength of the radiation is continuously adjustable in FELs.

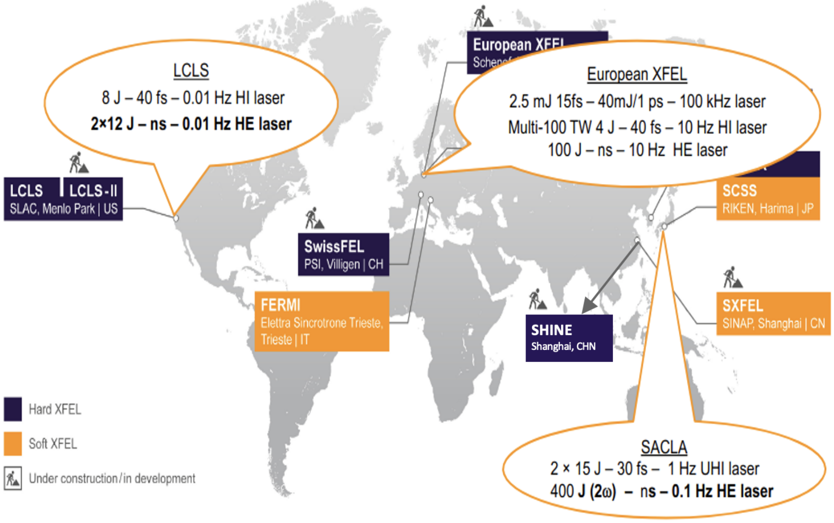

Figure 1.2: The X-ray FEL facilities around the world.

There are several X-ray FEL facilities around the world. Most of them are working in the self-amplified spontaneous emission (SASE) mode. The SASE FEL starts from the spontaneous radiation of the electron within the undulators, and then the part of the radiation that is resonant with the undulator setup is amplified exponentially to obtain high-power at saturation (Kondratenko and Saldin [1980], Bonifacio et al. [1982], Kim [1986a,b]). The SASE mode does not require an incident laser to seed the lasing process, which makes it easy to apply. The main XFELs working in SASE operation mode are the Linac Coherent Light Source (LCLS) in the USA (Nuhn [2002]), European XFEL in Germany (Decking et al. [2020]), SwissFEL in Switzerland (Milne et al. [2017]), Pal-XFEL in South Korea (Kang et al. [2017]), and SACLA in Japan (Yabashi et al. [2015]). More XFELs, such as Shanghai High Repetition Rate XFEL and Extreme Light Facility (SHINE) in China (Zhu et al. [2017]), are under construction.

The SASE FEL produces x-ray pulses with poor longitudinal coherence since the emission starts from a randomly distributed electron beam. One method to obtain coherent FEL pulses is by high-gain harmonic generation (HGHG), in which a seeded laser is applied to modulate the electron beam to create microbunching (Yu et al. [2000]). The electron beam is then lasing at a harmonic frequency in subsequent undulators. Some FELs working in HGHG mode are FERMI FEL (Allaria et al. [2012]) in Italy and SXFEL (Zhao et al. [2017]) in China. Another way to improve the coherence is called self-seeding, in which a monochromator is inserted between two segments of undulators to generate a mono-beam as a seed for amplification. A new method, an x-ray free-electron laser oscillator (XFELO), has been proposed to use an optical cavity based upon the Bragg reflection from crystal to generate highly coherent XFEL pulses (Kim et al. [2008]).

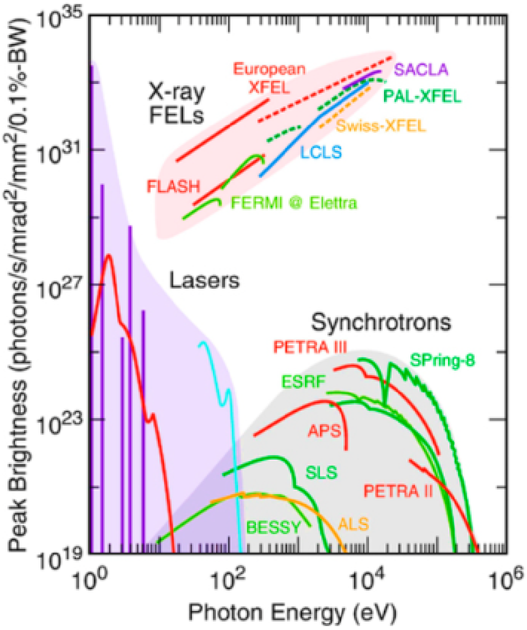

Figure 1.3: The brightness of FEL pulses compared to the laser-based light sources and synchrotron radiation. Figure from Ullrich et al. [2012].

The FEL pulses have unique properties that offer new opportunities in material science, chemistry, and biology. As shown in Fig. 1.3, the FELs generate pulses with 10 orders of magnitude higher brightness than synchrotron radiation in x-ray regime. FELs generate photons with photon energy continuously tunable up to 25 keV. The light sources based on laser high harmonic generation (HHG) have a photon energy cut-off, which makes it hard to push to the high-energy x-ray regime. The conversion efficiency from optical pulses is $\sim 10^{-8}$ giving less than nanojoule pulse energies in the soft x-ray range (Seres et al. [2005]). FEL generates x-ray pulses with pulse energy up to a few mJ and peak power reaches 10^{18} W/cm^2. With this high peak intensity, it opens the opportunity to explore nonlinear light-matter interaction in x-ray regime. The FEL pulse duration is around tens of femtoseconds, which is determined by the electron bunch duration and the slippage between light and electron beam in the undulators. With the new electron beam self-modulation and nonlinear compression technique, the pulse duration is shortened to sub-femtosecond (Duris et al. [2020]), which makes XFEL an appealing tool for investigating ultrafast electronic and nuclear dynamics in molecules and materials. The XFEL pulses are fully transverse coherent, which is essential for coherent diffraction imaging (Gaffney and Chapman [2007], Ho and Santra [2008], Ho et al. [2021]). The combination of high pulse energy and transverse coherence makes XFEL a potential tool for single-molecule imaging and even making molecular movies (Fratalocchi and Ruocco [2011]).

1.2 Nonlinear optical and x-ray spectroscopy

The last decades have witnessed a thriving investigation into understanding fundamental light-matter interactions and a rapid advance in atomic, molecular, and optical experimental techniques. Nonlinear phenomena enabled by intense light sources in the optical, infrared, and microwave regions have been utilized to control electronic, nuclear, and spin degrees of freedom which have led to breakthroughs across many fields of science, such as medical imaging, telecommunication, and the creation and manipulation of novel materials. The advent of XFELs offers unprecedented high-brightness x-ray pulses, thus opening the pathway to nonlinear light-matter interactions in the x-ray regime. The successful observation of several nonlinear x-ray optical phenomena and ultrafast pump/probe experiments using XFELs have suggested that transferring nonlinear optical spectroscopy to x-ray regimes is a feasible and fruitful approach.

Nonlinear optics focuses on the studies of the nonlinear modification of the properties of the light passing through the material system. It occurs when the response of the material system subjected to the radiation scales nonlinearly with the strength of the field applied. The investigation of nonlinear optics started with the discovery of second-harmonic generation by Franken et al. [1961], shortly after the demonstration of the laser by Maiman et al. [1960]. The occurrence of nonlinear modification of the light requires sufficient high laser fields, usually at the order of 10^{11} V/m or 10^{16} W/cm^2, which is comparable to the electric field experienced by the electron in an atom $E_{at} = e/(4\,\pi\,e_0\,a_0^2)$. The response of the medium to the electromagnetic fields is characterized by the susceptibilities, which are the coefficients connecting the polarization induced by the electric field (Boyd et al. [2008]):

$$P = e_0 \left[\chi^{(1)}E + \chi^{(2)}E^2 + \chi^{(3)}E^3 + \cdots\right] \tag{1.2}$$

The reason why polarization plays an essential role is that the time-varying polarization acts as a source term of radiation in the Maxwell wave equation, which generates new fields at new frequencies as the laser pulse propagates through the medium. For example, the generation of the second harmonic 2ω from the incident laser with frequency ω depends on the second order susceptibility $\chi^{(2)}$ of the material.

There are many interesting nonlinear optical phenomena that have wide applications. Sum-frequency generation (SFG) takes two incident light fields $E = E_1\,e^{i\,\omega_1\,t} + E_2\,e^{i\,\omega_2\,t}$ with different frequencies ω_1 and ω_2 to produce light at the sum frequency $\omega_3 = \omega_1 + \omega_2$. This can be seen from Eq. (1.2), where the second term E^2 would have a frequency at $\omega_1 + \omega_2$. The dipole oscillation at this frequency generates light at ω_3. SFG could be used to obtain photons at a higher frequency. A dense medium is usually applied to increase the conversion efficiency and momentum conservation required which makes the emission from different atoms add constructively thus generating a strong emission. It has been shown that the infrared-visible light SFG is a versatile tool for studying many kinds of surfaces and interface dynamics and reactions with sub-picosecond time resolution (Shen [1989]). Also, second harmonic generation (SHG) is widely used. SHG has been used even with FELs to get surface sensitivity with elemental tags.

The inverse process of sum-frequency generation is parametric down-conversion, where the incident photon is converted to two photons with lower frequencies. Under certain circumstances, the two photons generated are entangled with each other (Kwiat et al. [1995]). This entangled photon pair source is an important tool to test some fundamental quantum mechanics principles such as Bell inequality (Bell [1964]) and a useful tool in quantum teleportation (Bouwmeester et al. [1997]).

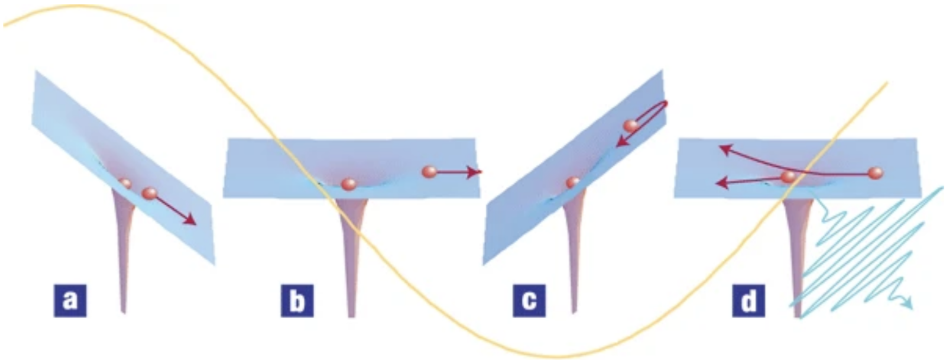

Figure 1.4: The schematic of the three-step model of HHG: (a) strong laser field (orange line) modifies the electron binding potential and leads to tunneling ionization; (b, c) electron accelerate in the laser filed and heading back toward the ion; (d) electron collision with the ion it freed from and emit high harmonic photons (green line). Figure from Corkum and Krausz [2007]

High harmonic generation is a technique that takes advantage of the nonlinear optical response of a material to generate ultrashort high-energy photon pulses (Corkum [1993], Corkum and Krausz [2007]). The strong incident field modifies the electric field that binds the electrons and the electron tunnels through the potential well tilted by the laser field (see Fig. 1.4). The tunnel-ionized electrons keep accelerating and gain energy in the incident laser field. When the field changes direction, the electron comes back and collides with the ion and creates higher harmonic photons. Since the process is driven by the coherent incident laser pulse, the radiations from different harmonics are in phase with each other. The ultra-broad bandwidth high harmonic pulse corresponds to an ultra-short pulse in the time domain.

The attosecond pulse generated by HHG is a powerful tool for studying ultrafast atomic and molecular dynamics in real-time (Li et al. [2020a]). For example, HHG was applied to observe the coherent valence electron motion in krypton atoms (Goulielmakis et al. [2010]). The incident infrared (IR) laser pulse is used to pump dense neon gas, and high harmonic sub-fs extreme-ultraviolet (EUV) pulses are generated. One important feature is that the IR and EUV pulses are naturally synchronized and the time delay can be adjusted by a mirror assembly. The dynamics of the target was initiated by the IR pulse by strong-field ionization, and the absorption spectrum of the EUV pulse was measured at different time delays to map out the ultra-fast electronic dynamics. The few femtosecond IR pulse has a bandwidth that is broad enough to cover several ionic states, which induces a coherent superposition state (Rohringer and Santra [2009]). The ultrafast oscillation of the superposition state is observed in real-time from the EUV absorption spectrum. Following this demonstration, HHG was extended to follow the ultrafast dynamics in bigger systems, i.e. SF6 and CF4 molecules (Pertot et al. [2017]), and even control the charge migration in ionized iodoacetylene (Kraus et al. [2015]).

Other nonlinear optical processes describe the laser pulse reshaping when passing through the medium. The attenuation of light in a material is described by Beer-Lambert law, which says that the intensity of light decreases exponentially with respect to the penetration depth. However, for a high-intensity pulse, the medium tends to absorb less light. This phenomenon is called self-induced transparency (SIT) (McCall and Hahn [1967]). It occurs when the pulse that passes through a resonance medium has integrated intensity close to or larger than a

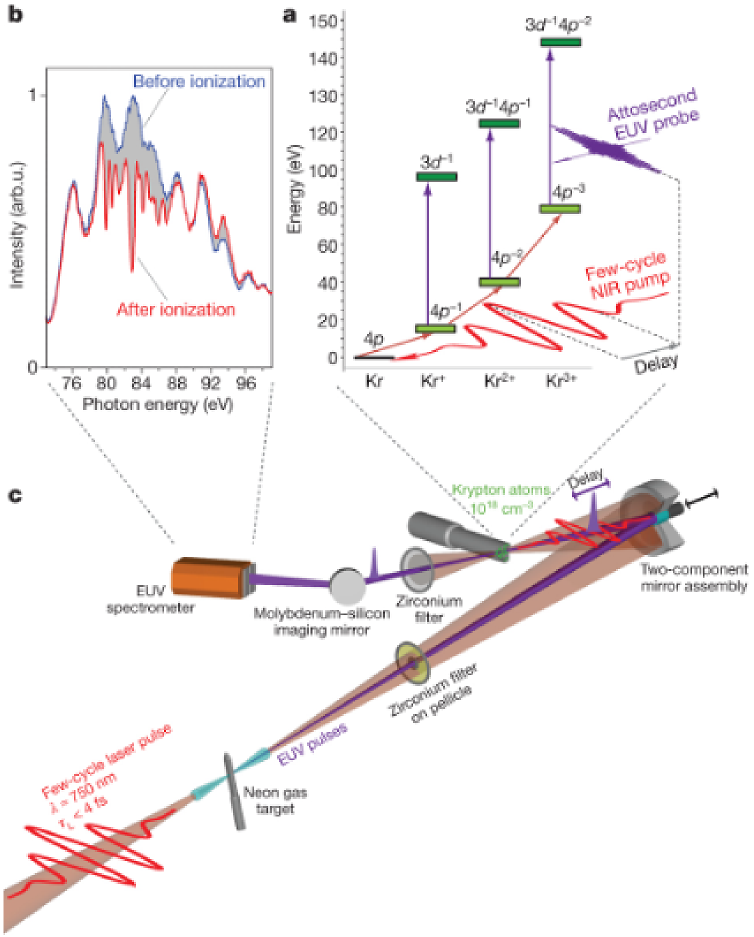

Figure 1.5: The IR/EUV HHG pump-probe experiment to track the ultrafast valence electron motion in Krypton ions. Figure from Goulielmakis et al. [2010].

pi-pulse, which leads to a full population transition from ground state to excited state (see Fig. 1.8). Basically, an intense pulse excites most electrons from the ground states to the excited states, which saturates the absorption capability of the material. The large change in the excited population violates the small perturbation of the population assumed in the Beer–Lambert law. When resonant SIT occurs, the incident pulse is temporally reshaped to have oscillating structures (Chiao et al. [1964], Crisp [1970]).

Self-focusing (SF) is another nonlinear process when the incident light is spatially reshaped by the medium (Akhmanov et al. [1968], Wright and Newstein [1973], Gibbs et al. [1976]). For some materials, the susceptibility is a function of the field intensity. Different transverse positions of the pulse experience different refractive indexes, thus the wavefront of the incident pulse is modified as it propagates. In the case when the high-intensity inner fields have a higher refractive index than the outer fields, the pulse is focused. SF can increase the laser peak intensity and induce damage to the gain medium in the laser oscillator, which was an obstacle that prevented the further improvement of the laser power. The problem was solved by the chirped pulse amplification technique demonstrated by Strickland and Mourou [1985].

The advent of XFELs opens the pathway to expand the nonlinear optical techniques mentioned above to the x-ray regime. The nonlinear x-ray techniques can exploit several unique properties of x-ray matter interaction. First, x-rays can probe materials with element sensitivity. In contrast to an optical laser, whose photon energy is resonant with valence electron transitions, x-ray photons can excite core electrons. The energy of core electrons varies from element to element, thus x-ray has element sensitivity. By choosing the x-ray energy resonant with a specific element in a molecule, one can control the initial excitation site or the probing site with atomic spatial resolution. Second, high energy resolution x-ray spectroscopy is sensitive to the chemical environment surrounding the atom, since the chemical bond shifts the energy levels. This was widely used to probe the transient species in ultrafast chemical reactions. Third, x-ray photons are energetic enough to photoionize the atom, thus photoelectrons or Auger electrons can be detected thus providing more information about the samples. In addition, hard x-ray photon has energy higher than most of the inner-shell electrons of light elements, which enables it to penetrate through the surface of the sample and make the probe sensitive to the bulk properties. Finally, the wavelength of the hard x-ray is much shorter than the optical wave, which means it is able to image samples with higher resolution.

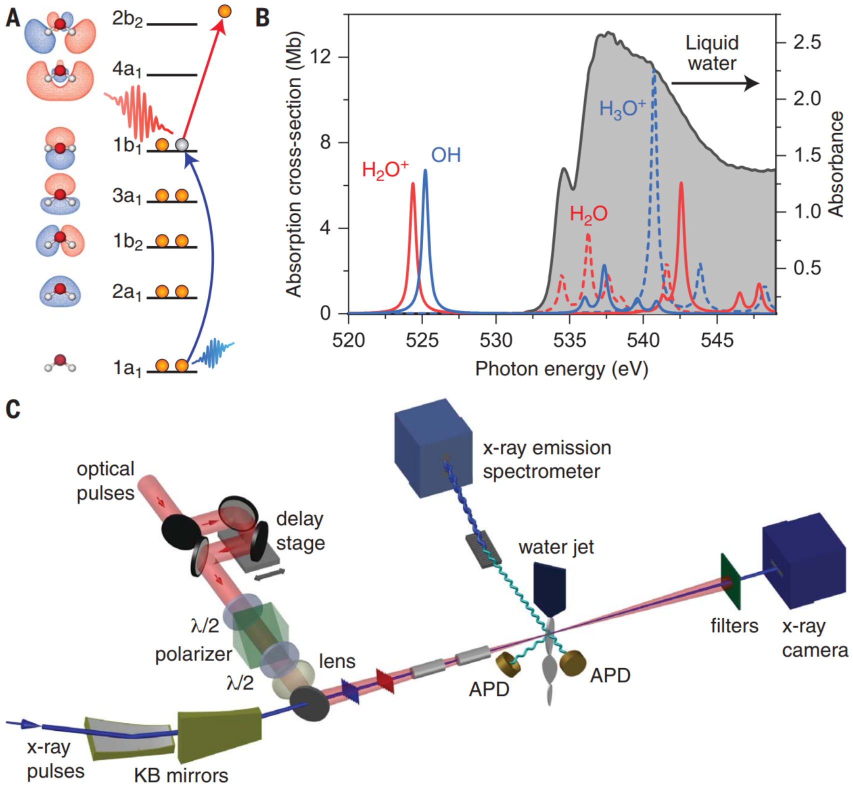

Figure 1.6: The IR pump/x-ray probe experiment to investigate the ultrafast proton transfer after strong field ionization of liquid water. Figure from Loh et al. [2020]

Besides the unique properties of x-rays, the ultrashort femtosecond XFEL pulses are suitable for tracking ultrafast electronic and molecular dynamics. The x-ray promotes the core electron to the unoccupied valence states, thus XFEL absorption spectroscopy can be used to map the ultrafast dynamics after electronic transition with femtosecond time resolution.

The laser pump/x-ray probe is similar to the study by Goulielmakis et al. [2010], except here the XFEL is used as the probe rather than HHG. For example, the IR pump/XFEL probe is applied to observe the fastest chemical process - proton transfer reaction - in the radiolysis of water (Loh et al. [2020]). Liquid water is valence ionized by the strong IR field, and XFEL pulses with central photon energy around the oxygen core valence transition are used to probe the x-ray absorption spectrum. By scanning the pump/probe time delay, the ultrafast proton transfer process $H_2O^+ + H_2O \to OH + H_3O^+$ is shown to occur around 50 fs after the valence ionization. These studies all use x-rays as a linear ultrafast probe of dynamics.

However, transferring nonlinear optical techniques to x-ray regimes using XFEL is not straightforward. The x-ray photon is energetic enough to ionize the electrons, thus with high-intensity x-ray beams, sequential photoionization happens (Rohringer and Santra [2007], Young et al. [2010], Doumy et al. [2011], Ho et al. [2014]). The high energy core excited states undergo ultrafast decay through spontaneous photon emission or ejecting Auger electrons. Instead of generating higher harmonics as in the optical case, the combination of x-ray photoionization and ultrafast Auger decay creates highly charged states. Nonlinear two-photon absorption is observed with XFEL. However, the cross-section is typically much smaller than the sequential multi-photon processes (Tamasaku et al. [2014]).

In addition to being absorbed and transferring the photon energy to photoelectrons, the x-ray photon scatters from the atom. For optical photons, where the energy is lower than the resonant energy levels, Rayleigh scattering happens with a cross-section proportional to ω^4. For the x-ray photon energies higher than the resonance, Thomson scattering happens with a constant cross-section. The refractive index, related to the scattering of photons, reduces by a factor of $1/\omega^2$ above the resonance, thus the refractive index of materials for x-rays is typically very small, differing from the vacuum value by only $\sim 10^{-4} - 10^{-6}$. This small refractive index makes nonlinear phenomena such as harmonic generation with x-rays

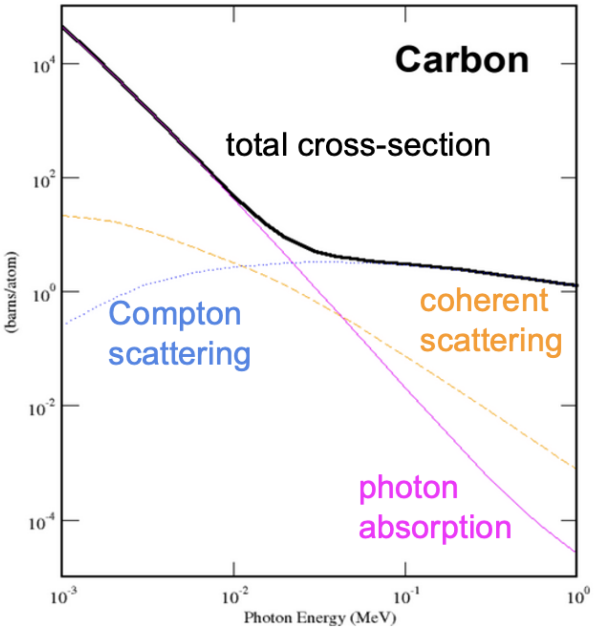

Figure 1.7: The cross-section of different processes in the interaction of x-ray photon and carbon atom. Figure adapted from Thompson et al. [2001].

very challenging.

With the high intensity of XFEL pulses, these challenges can be overcome. X-ray and optical wave mixing was demonstrated (Glover et al. [2012]) in a single-crystal diamond. This sum-frequency generation provides an atomic-scale probe of optical light-matter interactions. The x-ray second harmonic generation (SHG) was studied theoretically more than 40 years ago, which indicates that it is possible to observe SHG in the x-ray regime if pulse peak intensity exceeds 10^{16} W/cm^2. Using XFEL pulses, hard x-ray SHG was demonstrated in diamond crystal (Shwartz et al. [2014]). The signal was generated within a narrow phase-matching condition and the intensity scales quadratically with the incident intensity. The x-ray SHG is an emerging tool for probing the material surface with elemental tags (Zong et al. [2023]).

In contrast to off-resonance nonlinear x-ray physics, the resonant light-matter interaction is much stronger and easier to achieve. For a two-level system resonantly irradiated by a strong x-ray pulse, one important feature is that the population of the excited state will oscillate $|C_{ext}(t)|^2 \propto \sin^2(\Omega\, t/2)$, i.e. Rabi oscillation. Where $\Omega = d\, E_0/\hbar$ is the Rabi frequency, which is proportional to the transition dipole moment d and the incident field amplitude E_0. The pi-pulse is defined such that the field induces a full transfer of population from the ground state to the excited state. The definition of 2pi-pulse etc. follows the same rule.

Resonant nonlinear interactions differ from the off-resonant. The population transition from the ground state to excited states is typically small for off-resonance interaction. Thus perturbation theory is valid for calculating the off-resonance nonlinear processes, for example, when calculating the nonlinear polarization driven by the field. In contrast, a considerable amount of population transfer happens in resonance interaction, thus perturbation theory is not valid anymore. A full solution of the Schrodinger equation is needed to study the resonance nonlinear processes.

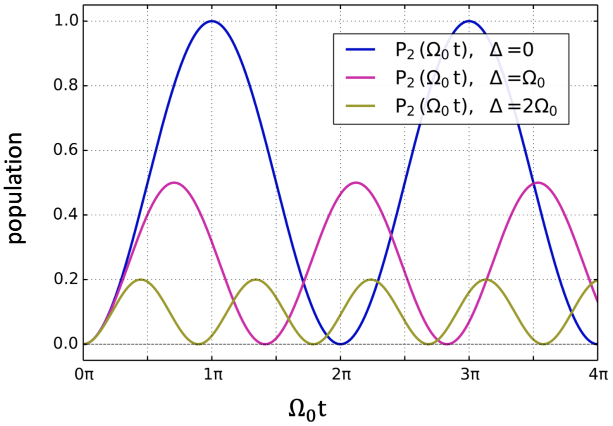

Figure 1.8: The excited state population of a two-level system oscillates when interacting with a resonant pulse - Rabi oscillation. The Rabi frequency Ω_0 increases and the maximum excited state population drops as the laser frequency detuning Δ increases.

The transition dipole moment is relatively small for core to excited state transitions. With XFEL pulses, the x-ray field is strong enough to induce large population transfer. The wavefunction of the quantum system has term $C_{ext}(t)\, e^{-i\,\omega_0\, t} = \sin(\Omega\, t/2)\, e^{-i\,\omega_0\, t}$, which provides the dipole oscillation with frequency $\omega_0 \pm \Omega/2$. This could modify the experimental observations, i.e. typically lead to additional sidebands in the spectroscopy. For example, the resonant Auger spectrum is predicted to develop sidebands when the x-ray radiation is sufficient ($\sim 10^{18}$ W/cm^2) to drive Rabi oscillation before the ultrafast decay of the neon core-excited states. The predicted broadening was observed in Auger spectroscopy with SASE FEL in Kanter et al. [2011]. Another theoretical study shows that the resonance fluorescence spectrum would be modified when radiated by intense ultrashort XFEL pulses (Cavaletto et al. [2012]).

With large resonant population transfer, the high-intensity XFEL pulses can saturate the resonant absorption. X-ray self-induced transparency is observed in resonant propagation of XFEL pulses in the Co film (Stöhr and Scherz [2015], Chen et al. [2018], Wu et al. [2016]). In the experiment, both the scattered photon distribution and the transmitted pulse spectrum are monitored. At high XFEL intensity, the amount of scattered photons is reduced while the transmitted pulse energy increases. The change of the stimulated resonant elastic and inelastic scattering spectrum is also observed (Higley et al. [2022]). These are explained by strong x-ray induced stimulated forward scattering, which competes with off-axis elastic scattering.

1.3 X-ray laser and stimulated Raman scattering

Among these nonlinear x-ray effects, x-ray lasing and stimulated Raman scattering are fundamental nonlinear processes happening in x-ray resonant propagation in a dense medium. Scientists have struggled to achieve the amplification on atomic transitions of increasingly shorter wavelengths, since the invention of the optical laser in the last century. The short lifetime of the core-excited states and the requirement of ultrahigh intense pump pulse make the achievement of an x-ray atomic laser challenging. In the soft-X-ray/vacuum-ultraviolet regime, population inversion is typically achieved by collisional excitation or recombination into excited states of highly ionized atoms in a hot, dense plasma (Suckewer and Jaegle

[2009]). X-ray laser from the rapid photoionization of inner-shell electrons in a dense medium was studied theoretically soon after the birth of the optical laser (Duguay and Rentzepis [1967]). However, the lack of sufficiently short and intense X-ray pulses had precluded the realization of the photo-ionization scheme in the X-ray regime.

The emergence of XFELs, delivering femtosecond high-intensity x-ray pulses, opens a new pathway to pump atomic x-ray lasers (XRL). The rate equation calculation shows that it is possible to induce population inversion in atomic inner-shell by XFEL pumping (Rohringer and London [2009]). The atomic inner-shell XRL at 1.46 nm pumped by XFEL was first realized at LCLS in 2012 (Rohringer et al. [2012]). SASE FEL pulses centered at 960 eV were used to pump a 500 torr neon gas target. A downstream spectrometer was installed to measure the photon spectrum passing through the gas cell. The lasing line at 849 eV corresponding to the 1s to 2p transition in the singly charged neon ion was observed. The lasing pulse energy increased exponentially as the incoming XFEL pulse energy was tuned up. This exponential gain confirmed the achievement of a population inversion and x-ray stimulated emission.

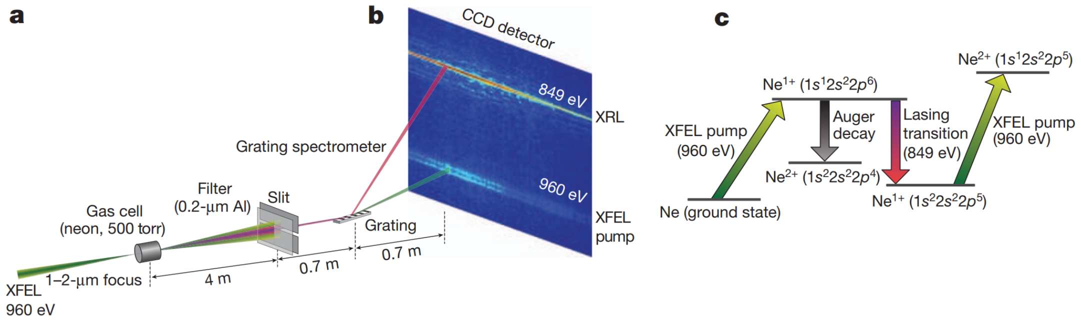

Figure 1.9: The schematic of XRL experiment. The strong lasing at 849 eV is measured by the spectrometer after the SASE XFEL pulse passes through a dense neon gas cell. Figure from Rohringer et al. [2012].

Efforts have been made to extend the x-ray-pumped XRL from atoms to molecules, which include additional nuclear degrees of freedom. The spectral and temporal output of a molecular XRL has been estimated by the generalized Maxwell-Bloch equation (Kimberg and Rohringer [2013], Kimberg et al. [2013, 2014]). But so far no observation of XRL in a diatomic molecule gas target has been reported. The amplified K_α x-ray emission from solutions of Mn(II) and Mn(VII) complexes was observed by using XFEL pulses to create the 1s core-hole population inversion (Kroll et al. [2018]). Amplified K_β emission was reported when adding a second x-ray pulse to seed the transition. The stimulated x-ray emission is shown to preserve the chemical sensitivity of the 3d transition metal systems. With the signal being amplified orders of magnitude, stimulated x-ray emission could be a powerful probe for electronic structure analysis and ultrafast nuclear dynamics. The x-ray-induced population inversion is also a new way to generate x-ray laser with improved longitudinal coherence from SASE. The population-inversion x-ray oscillator (XLO), which combines an x-ray crystal cavity with XRL, has been proposed to generate high brightness coherent x-ray pulses (Halavanau et al. [2020]).

Raman scattering is a kind of inelastic scattering of photons, where the energy of the scattered photon is different from that of the incident photon. Raman spectroscopy is widely used in characterizing the vibrational modes of molecules, which are a fingerprint to identify molecules. The spontaneous Raman scattering cross section is much smaller than the elastic Rayleigh scattering. As a result, it was a challenge to separate the Raman signal from the intense Rayleigh scattered photon. The laser-stimulated Raman emission was reported around 1962 soon after the laser was invented (Eckhardt et al. [1962], Minck et al. [1963]). Due to the gain from the dense medium, the stimulated Raman signal is much stronger than the spontaneous Raman.

Stimulated Raman spectroscopy (SRS) is a form of spectroscopy widely employed in physics, chemistry, biology, and other fields. This technique is based on stimulated Raman scattering, where two pulses are used. The pump pulse with frequency ω_p induces an upper transition to virtual states and a Raman pulse with frequency ω_r induces a down transition. After the Raman scattering, there is a vibrational excitation ω_v remains in the system. The

Raman signal is enhanced by the stimulated emission at the resonance $\omega_p - \omega_v = \omega_r$.

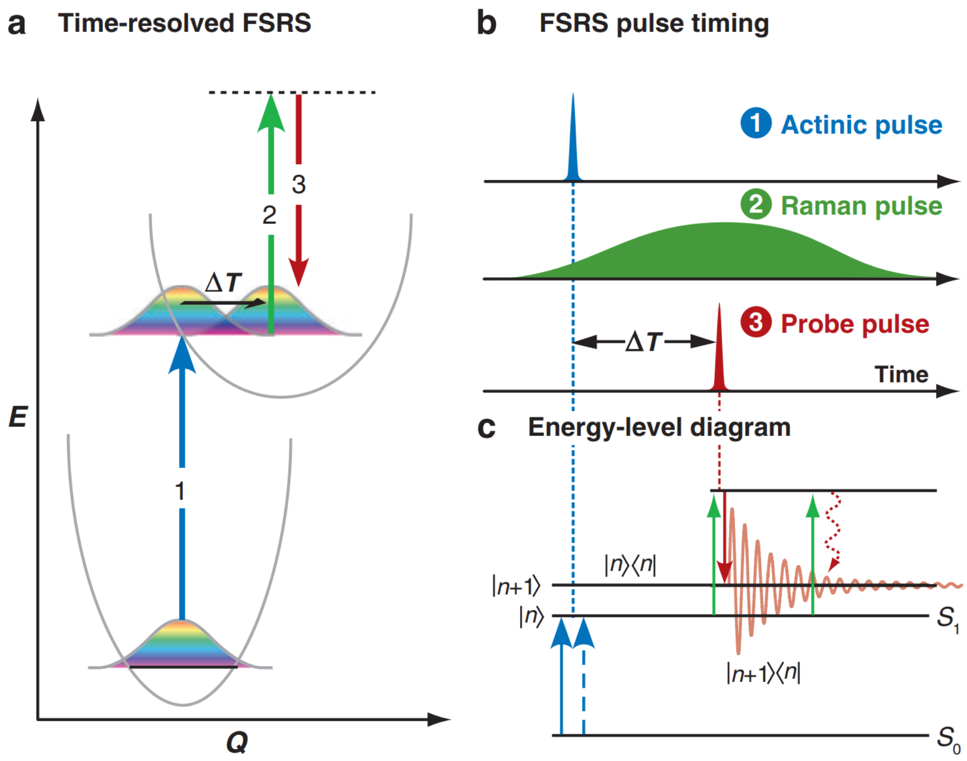

Figure 1.10: The principle of FSRS. The sample is first excited by the actinic pulse, and then the dynamic is detected by stimulated Raman spectroscopy with a long Raman pulse and an ultrashort probe pulse. The time resolution is defined by the delay ΔT and the spectral resolution is determined by the convolution of Raman pulse with the decay lifetime of the vibronic coherence. Figure from Kukura et al. [2007].

With the advent of femtosecond laser pulses, femtosecond stimulated Raman spectroscopy (FSRS) is a new ultrafast spectroscopic technique that provides vibrational structural information with high temporal (50 fs) and spectral (10 cm^{-1}) resolution (Kukura et al. [2007]). In FSRS, an actinic pulse is applied to initiate the electronic transition from a ground state to an excited state (see Fig. 1.10). The molecule wave packet evolves in the upper-level state. After a delay time ΔT, a stimulated Raman transition is driven by a long (ps) Raman pulse and a short (fs) probe pulse. By scanning the SRS as a function of the time delay, the electronic dynamics and nuclear motion could be mapped out. The temporal resolution of this technique is determined by the time delay, while the spectral resolution is defined by the bandwidth of a convolution between Raman pulse and the the decay of vibronic coherence. One of the critical advances of the FSRS is circumventing the limitation of the Heisenberg uncertainty principle. As a result of its unique capabilities, FSRS has proved to be a powerful tool in studies of chemical and biochemical reaction dynamics, giving new insights into the structural dynamics of reactively evolving systems with atomic spatial and femtosecond temporal resolution.

With the advent of XFELs, it is natural to extend stimulated Raman techniques into x-ray regime, which brings in unique x-ray properties. The ultrafast stimulated x-ray Raman spectroscopy (SXRS) resembles FSRS. But instead of probing the vibration in the molecules, SXRS is sensitive to the electronic coherence. SXRS is promised to be able to probe the electronic coherence and track the long-range electron transfer with atomic resolution and sub-fs temporal resolution (Zhang et al. [2014], Cavaletto et al. [2021]).

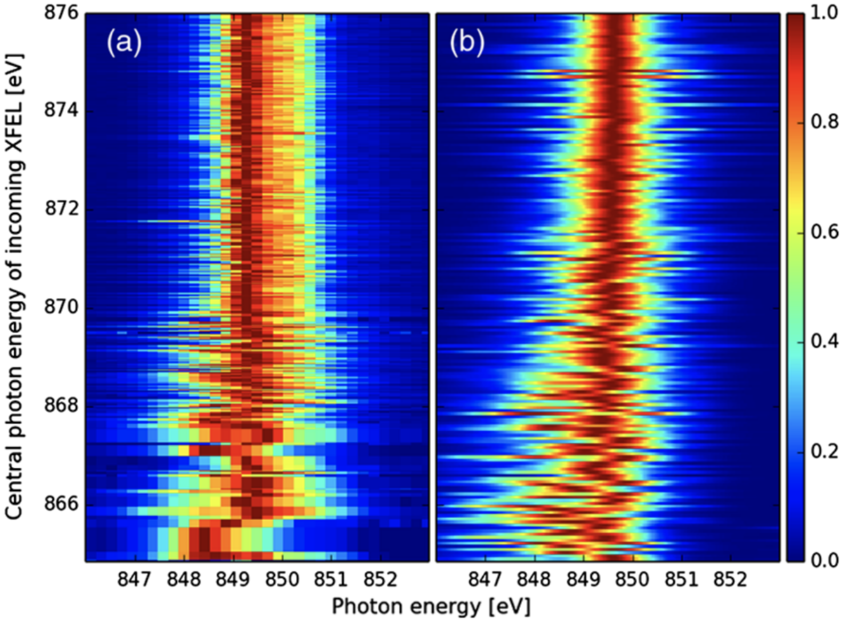

Figure 1.11: The experimental (a) and simulation (b) results of x-ray stimulated Raman spectrum from the dense neon gas when pumped by SASE XFEL pulses. The central photon energy of the incident pulse is scanned across the K edge. Figure from Weninger et al. [2013].

One challenge of the x-ray Raman spectroscopy is the extremely small scattering cross-section. To overcome this, the x-ray stimulated Raman in a dense medium can provide orders of magnitude gain in the forward Raman emission. The exponential amplification of an x-ray Raman signal was first demonstrated in a dense neon gas (Weninger et al. [2013], Weninger and Rohringer [2013]), where incident SASE FEL pulses were used to pump the neon electron from 1s state to unoccupied Rydberg states and then 2p electron fills the core hole and emits the Raman photon. This Raman transition leaves a valence excitation in the atom that equals the photon energy loss. An exponential gain of the scattered pulse energy was observed when increasing the incident pump intensity, which indicates the realization of population inversion. Yet, the unique dispersive feature of a Raman spectrum as a function of incident photon energy is not obvious, due to the random spikes in the SASE pulses. The clear evidence of stimulated Raman scattering and its cross-section as a function of different pump photon energy is shown by photon-recoil imaging (Eichmann et al. [2020]). The momentum transfer is measured after the photon-atom interaction. The signature of stimulated Raman scattering, which gives a fixed momentum transfer in the forward direction, stand out from the isotropic momentum transfer distribution in the spontaneous Raman scattering.

As a crucial building block for nonlinear x-ray spectroscopy (Kimberg et al. [2016], Rohringer [2019]), efforts have been made to achieve SXRS in different systems. Yet, extending the SXRS to molecular or more complex systems is challenging due to the ultrafast nuclear dynamics and the random molecular alignments. The nuclear vibration reduces the transition dipole moment of a specific Raman channel by the Franck–Condon factor and the ultrafast dissociation hinders the completion of the Raman process. The impulsive stimulated Raman was demonstrated in NO molecular by measuring a 2.6% enhanced NO^+ yield (O'Neal et al. [2020]). The gain of stimulated Raman signal is predicted to be possible in the dense molecular gas with two-color XFEL pulses(Kimberg and Rohringer [2016]), where the pump pulse induces an upward transition, while the Raman pulse stimulates the resonance down transition. However, the experiment showed no clear evidence of the stimulated Raman gain, which might be due to the random alignment of the molecule that is not favorable for the Raman transition with a linear polarized XFEL pump (Kimberg and Rohringer [2016]).

Meanwhile, to circumvent the stiff requirements of multiple delay-controllable coherent x-ray pulses in attosecond SXRS, the statistical properties of the stochastic SASE XFEL pulses may be exploited. The covariance analysis, which takes advantage of the the correlation between SASE spectrum and the SXRS spectrum, has been proposed to obtain high energy resolution SXRS (Kimberg and Rohringer [2016], Cavaletto et al. [2021]).

The thesis is organized as follows. Chapter 2 describes a theoretical model of x-ray resonant propagation through a dense gaseous medium. The three-dimensional coupled time-dependent Schrodinger equation and Maxwell wave equation are solved. The simulations with ultrashort Gaussian pulses show interesting nonlinear x-ray phenomena such as SXRS, XRL, SIT, and SF. More realistic simulations with XFEL pulses (SASE and XLEAP) are explored. In Chapter 3, we discuss the experiment on resonant propagation of SASE pulses through dense neon gas performed at the European XFEL. The transmitted and emitted x-ray spectra are measured by a grating spectrometer after the gas cell. Covariance analysis between the transmitted SASE and the Raman signal gives an unprecedented high-resolution SXRS spectrum. Supercomputer simulations confirmed our observation and provided insights into the SXRS process as well as the ways to improve the spectrum. Chapter 4 presents a novel method of non-invasive characterization of SASE spectra using a ghost-imaging (GI) algorithm. The correlation between photoelectron spectrometer (PES) array signal and grating spectrometer measurements is exploited to compute the response matrix of the PES array, which is then used to reconstruct a SASE spectrum with less noise and higher resolution. The experimental factors that influence the performance of the GI method and how to improve it are discussed. The high-resolution non-invasive characterization of the incident SASE spectrum shot-by-shot would benefit SXRS, attosecond transient absorption spectroscopy, and other x-ray spectroscopies. Finally, a summary and outlook are presented in Chapter 5.

CHAPTER 2

THEORETICAL MODEL OF X-RAY RESONANT PROPAGATION

A three-dimensional (3D) theoretical model is developed to simulate the resonant propagation of x-ray pulses through a dense medium. The time-dependent Schrodinger equation (TDSE) is solved in the temporal domain to compute the response of atoms to the fields. The Maxwell wave equation (MWE) is solved in the spectral domain to track the propagation and emission process. The coupled equations are solved step by step following the propagation of the fields.

As the x-ray intensity increases, the resonant propagation evolves from the linear regime to the nonlinear regime. Interesting phenomena, such as stimulated x-ray Raman scattering, x-ray lasing, self-induced transparency, and self-focusing are observed in the simulations. The influence of the pulse duration and peak intensity on these nonlinear phenomena is studied. The code is also used to carry out the resonant propagation simulations of XFEL pulses, which can be experimentally realized at XFELs.

2.1 Theoretical model

To simulate the propagation of x-ray pulses in the medium, we solve the coupled time-dependent Schrodinger equation (TDSE) and Maxwell wave equation (MWE). The TDSE computes the time evolution of the states of the medium, which is used to calculate the polarization. The interaction of the atoms in the gas medium is ignored, thus the macroscopic polarization equals the sum of the microscopic polarization from all atoms. The polarization calculated is a source term for the MWE, which is solved to get the new propagating fields. The new fields are then used as inputs for the TDSE equation for the calculation in the subsequent step.

The time-dependent Schrodinger equation describes the time evolution of wavefunction $\Psi(t)$ in atomic units:

$$i\frac{\partial}{\partial t}\left|\Psi(t)\right\rangle = [H_0 + H_{int}(t)]\left|\Psi(t)\right\rangle \tag{2.1}$$

where H_0 is the original interaction-free Hamiltonian of the quantum system; $H_{int} = r\,E(t)$ is the interaction Hamiltonian between the atomic electron at position r and the electromagnetic fields $E(t)$.

The wavefunction Ψ is solved for the neutral atom. To include the photoionization process in the simulation, the density matrix ρ is used to describe the ionized species:

$$i\frac{\partial\rho(t)}{\partial t} = [H_0 + H_{int}(t), \rho(t)] \tag{2.2}$$

The diagonal elements of the density matrix are the population of each state, while the off-diagonal elements are the coherences. We assume that the photoionization process populates the ionization species in an incoherent manner. Thus the diagonal elements of the density matrix are changed due to photoionization, while the off-diagonal elements remain the same.

The MWE for a frequency component ω is

$$[\nabla^2 + k^2]\vec{E}(\omega) = -\frac{k^2}{\epsilon_0}\vec{P}(\omega) \tag{2.3}$$

where $k = \omega/c$ is the wavenumber; $\vec{P}(\omega)$ is the frequency ω components of the polarization.

Following the derivation in Siegman [1986], after using slow-envelope approximation, one obtains the paraxial wave equation:

$$\nabla_\perp^2 + 2ik\,\frac{\partial\tilde{E}}{\partial z} = -\frac{k^2}{\epsilon_0}\tilde{P} \tag{2.4}$$

where $\tilde{E}$ and $\tilde{P}$ are the envelope of the field and the polarization, respectively. z is the propagation direction of the pulse, and $\nabla_\perp$ is the differential with respect to the transverse coordinates.

As an example, we consider an x-ray pulse resonantly propagating through a dense neon gas. The central photon energy is around 867.5 eV resonant with neon $1s \to 3p$ transition. The core-excited state $1s^{-1}3p$ can relax to the valence excited state $2p^{-1}3p$ at 18.2 eV and emit a Raman photon around 849 eV. The core-excited state $1s^{-1}3p$ can also undergo ultrafast Auger decay with a lifetime of $\Gamma_2 \sim 2.5$fs.

Photoionization happens when the incident photon energy is higher than the ionization threshold. The neon $1s$ and $2p$ ionization thresholds are 870 eV and 18.2 eV, respectively. The core electron ionization populates the core-hole state $1s^{-1}$ in Ne^+, and the valence ionization populates the valence-hole state $2p^{-1}$ in Ne^+. The Ne^+ core-hole state can transition to the $2p^{-1}$ state and emit a photon around 849 eV, or it can decay by ejecting an Auger electron. The Auger decay lifetime Γ_4 is assumed to be the same as the Auger decay in the neutral neon atom.

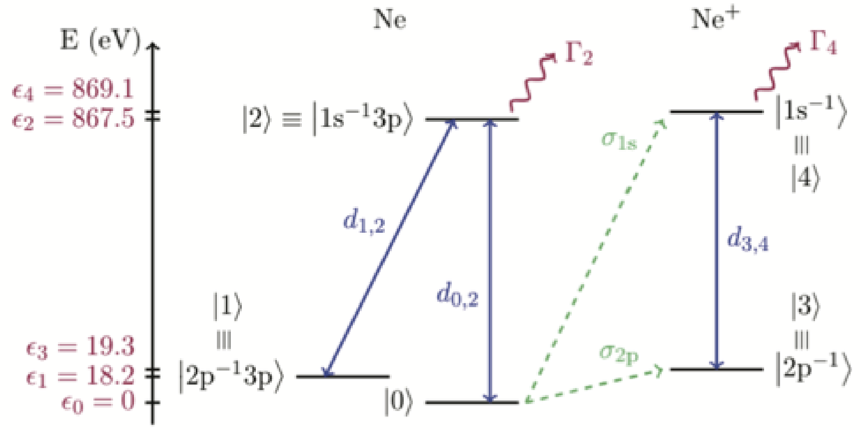

Figure 2.1: The energy level diagram of neutral neon and neon ion used in simulation. Figure from Li et al. [2020b].

As shown in Fig. 2.1, the states of neutral and ion neon included in the calculation are denoted by $|0\rangle, \cdots, |4\rangle$. Using the Schrodinger equation, we obtain a set of six coupled differential equations for the three wave function coefficients Ψ_0, Ψ_1, Ψ_2, the two populations

$\rho_{3,3}$ and $\rho_{4,4}$, and the coherence between the ionic states $\rho_{3,4}$, in atomic units:

$$i\dot{\Psi}_0(t) = -i\left(\frac{\Gamma_1(t)}{2} + \frac{\Gamma_2(t)}{2}\right)\Psi_0(t) + d_{0,2}\mathcal{E}(t)\Psi_2(t) \tag{2.5a}$$

$$i\dot{\Psi}_1(t) = \epsilon_1\Psi_1(t) + d_{1,2}\mathcal{E}(t)\Psi_2(t) \tag{2.5b}$$

$$i\dot{\Psi}_2(t) = \left(\epsilon_2 - i\frac{\Gamma_2}{2}\right)\Psi_2(t) + d_{0,2}\mathcal{E}(t)\Psi_0(t) + d_{1,2}\mathcal{E}(t)\Psi_1(t) \tag{2.5c}$$

$$\dot{\rho}_{3,3}(t) = \Gamma_2(t)|\Psi_0(t)|^2 - 2id_{3,4}\mathcal{E}(t)\,\mathrm{Im}(\rho_{3,4}(t)) \tag{2.5d}$$

$$\dot{\rho}_{4,4}(t) = \Gamma_1(t)|\Psi_0(t)|^2 - \Gamma_4\rho_{4,4}(t) + 2id_{3,4}\mathcal{E}(t)\,\mathrm{Im}(\rho_{3,4}(t)) \tag{2.5e}$$

$$\dot{\rho}_{3,4}(t) = \left[i\left(\epsilon_4 - \epsilon_3\right) - \frac{\Gamma_4}{2}\right]\rho_{3,4}(t) - id_{3,4}\mathcal{E}(t)(\rho_{4,4}(t) - \rho_{3,3}(t)). \tag{2.5f}$$

where the red terms are the self-evolution and spontaneous decay of the quantum states; the blue terms are the coherent dipole transitions coupled by the fields $\mathcal{E}(t)$ with dipole transition moments d denoted in the Fig. 2.1; the green terms are responsible for the population added into the ion by photoionization.

First, note that the density matrix is used to add the population of the ion from the neutral photoionization directly, without any coherence between neutral and ion, since we do not track the wavefunction of the photoelectron. Second, the Auger decay and photoionization are added phenomenologically, with rates Γ from experimental measurements. Third, the photoionization only changes the populations, i.e. the diagonal elements in the ion density matrix, without any coherence between core-hole and valence-hole. This excludes the additional dipole oscillation in the ion which prevents the miscalculation of the radiation. Finally, it is worth noting that the wavefunction formula is less computationally demanding than the density matrix, which is why the hybrid approach is applied.

The three-dimensional (3d) MWE is used to take into account the transverse profile changes of the pulse. The 3d MWE is solved in the frequency domain, by space marching through the medium in a frame that is moving with the speed of light. The incident light and the polarization induced are assumed to be linearly polarized, thus the vector wave equation can be simplified to a scalar equation. In SI units (used in the remainder of this article for MWE), and with all frequency-dependent quantities also functions of the cylindrical coordinates r and z, the MWE along the field polarization takes the form:

$$\begin{aligned}\nabla_\perp^2\tilde{\mathcal{E}}(\omega)+\frac{2i\omega}{c}\frac{\partial\tilde{\mathcal{E}}(\omega)}{\partial z}=&-\frac{\omega^2}{\epsilon_0c^2}\tilde{P}(\omega)\\&-i\frac{\omega}{c}\rho_{at}\tilde{\sigma}(\omega)\tilde{\mathcal{E}}(\omega).\end{aligned}\tag{2.6}$$

Here $\tilde{\mathcal{E}}(\omega)$ is the electric field which contains all the frequencies of the incoming and generated field, and the polarization source term $\tilde{P}(\omega)=\rho_{\mathrm{at}}\tilde{d}(\omega)$ is calculated from the single atom dipole moment $\tilde{d}(\omega)$, including both neutral and ion contribution, via Fourier transfer of the few-level TDSE solutions described above. The second term on the right-hand side represents the loss of energy of the fields due to ionization, where $\tilde{\sigma}(\omega)$ is the effective cross-section due to all ionization processes at frequency ω, and ρ_{at} is the density of neutral atoms.

To ensure the energy conservation of the fields+atom system, the last term in Eq. (2.6) is added to take into account the photon loss due to ionization. For each ionization channel i, the frequency-dependent ionization cross-section $\sigma_i(\omega)$ is taken as an arctangent function centered around the ionization threshold energy ω_{th}:

$$\sigma_i(\omega)=\sigma_i\left[\frac{1}{2}+\frac{1}{\pi}\arctan\left(2\frac{\omega-\omega_{\mathrm{th}}}{\Gamma_{\mathrm{ion}}}\right)\right],\tag{2.7}$$

where σ_i is the ionization cross-section, and Γ_{ion} is the inverse lifetime of the ionic state populated by the ionization process, which is equal to the Auger decay rate. The arctangent function is the convolution of the Lorentzian function with a step function across the K edge. This takes into account all the continuum states that can be populated by an ω photon, with the assumption that the ionized states all have the same lifetimes and that the cross-section is flat (Breinig et al. [1980]). We assume that the total instantaneous ionization cross-section is proportional to the field intensity $|\mathcal{E}(t)|^2$, i.e. the ionization rate in Eq. (2.5) is

$$\Gamma_i(t) = \alpha_i F^2(t) \tag{2.8}$$

$$F(t) = \frac{1}{\pi}\left|\int_0^\infty \tilde{\mathcal{E}}(\omega)e^{-i\omega t}\mathrm{d}\omega\right|. \tag{2.9}$$

where α_i is a constant factor. With more detailed derivation (Li et al. [2020b]) we have

$$\Gamma_i(t) = \frac{\varepsilon_0 c}{2\hbar\omega_i\rho_{\mathrm{at}}\Delta z}\frac{\int_{-\infty}^{\infty}|\tilde{\mathcal{E}}(\omega)|^2\left(1 - e^{-\rho_{\mathrm{at}}\sigma_i\Delta z}\right)\mathrm{d}\omega}{\int_{-\infty}^{\infty}|\tilde{\mathcal{E}}(\omega)|^2\mathrm{d}\omega}F^2(t) \tag{2.10}$$

In the code, the split-step algorithm is used to solve the TDSE equation efficiently (Arico et al. [2011]). The MWE is solved with a Crank-Nicolson algorithm (Crank and Nicolson [1947]). All Fourier transforms are computed with the FFTW package (Frigo and Johnson [2005]), and diagonalizations are performed using the LAPACK library (Anderson et al. [1999]).

There are several publications on the simulation of x-ray resonant propagation through dense medium. Interesting phenomena such as SXRS, XRL, and four-wave-mixing are predicted. In Sun et al. [2010], the 1d Maxwell-Bloch equation is solved with the finite-difference time-domain (FDTD) method for coherent Gaussian and sech pulses. They compared the two-level and three-level systems. The investigation focused on the stimulated Raman and ignored the photoionization effect. In Weninger and Rohringer [2013], the 1d Maxwell-Bloch equation is solved with slowly varying envelope approximation and rotating wave approximation. These approximations make the calculation much faster, yet the different nonlinear effects are not calculated on equal footing, i.e. the pump and probe pulse are treated in different manners and the four-wave-mixing effects are excluded. They included the photoionization effect, which is responsible for the XRL. Their work focused on the stimulated Raman and XRL spectrum evolution as propagation. Our theoretical model includes photoionization, and we extended the 1d simulation to 3d in order to track the evolution of the transverse profile of the beam. The wave cycling of the electric field is used in TDSE instead of the slowly varying envelope, thus all the different nonlinear effects are included and calculated on the same footing.

2.2 Resonant propagation of Gaussian pulse

The theoretical model is used to explore the resonant propagation of an ultrashort x-ray pulse through neon gas. The ultrafast pulse is chosen to allow the Raman transition before the Auger decay and the ultrashort pulse has a broad bandwidth in the spectral domain. Photoionization happens with photons that have energy above the neon ionization threshold. To gain some physical insights into the role of photoionization in the light-matter interaction, the population evolution without photoionization, with 1s ionization, and with 1s and 2p ionization are plotted in Fig. 2.2 at different propagation distances.

The incident pulse has a Gaussian profile with central photon energy at 867.5 eV resonant with $1s$ to $2p$ transition and FWHM of the pulse duration equals 0.25 fs. The Gaussian pulse is propagating through a 3 cm gaseous neon cell at an atmospheric pressure of 1 bar. The beam is focused at the center of the cell with a confocal parameter of 12.35 cm, which corresponds to a focus of 6.12 µm (FWHM) at the cell center. The peak intensity 10^{18} W/cm^2, which is available at XFELs, is strong enough to induce a population inversion between the ground state and the core-excited state. The transition dipole moments are from Weninger and Rohringer [2013] calculated by the method in Cowan [1981]. The photoionization cross sections are $\sigma_{2p} = 0.0084$ Mbarn and $\sigma_{1s} = 0.30$ Mbarn. Using these parameters, the x-ray absorption spectrum obtained by the code matches with the observation in Müller et al.

[2017].

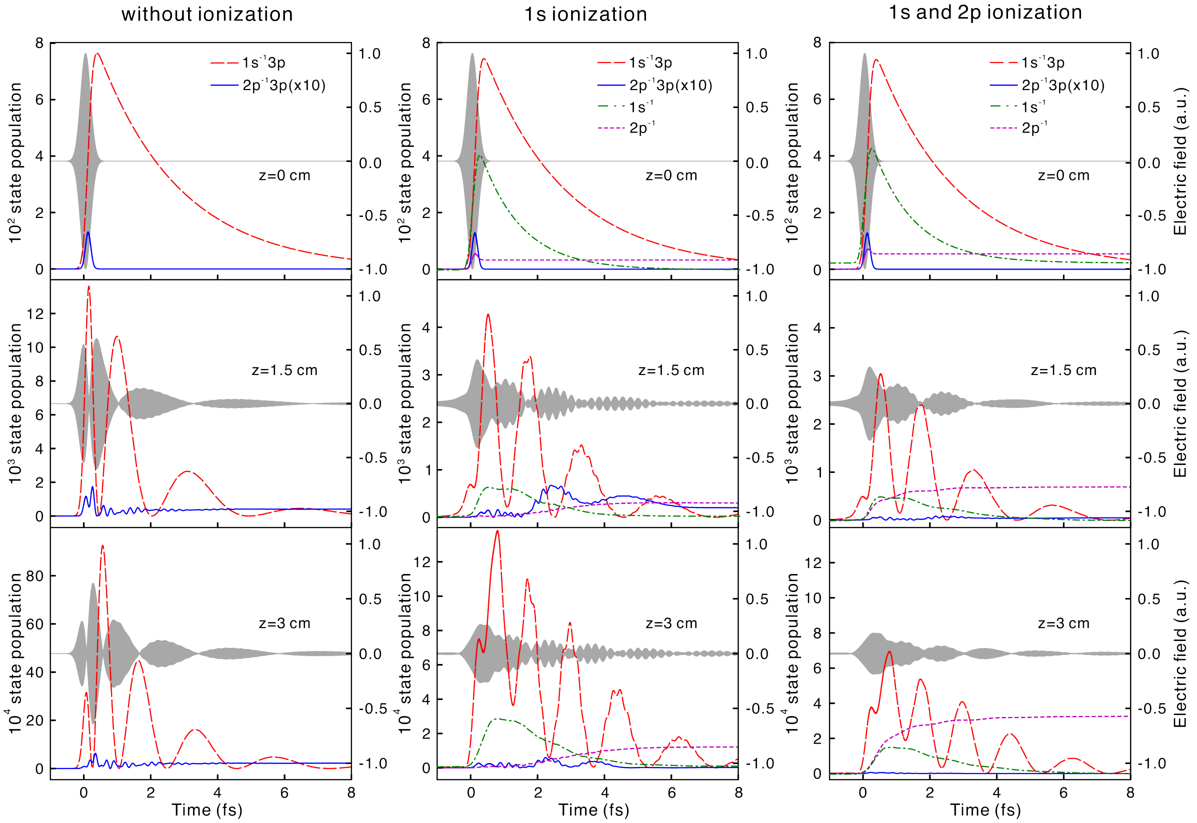

Figure 2.2: The population evolution of the different states at different propagation distance. A Gaussian pulse with 0.25 fs (FWHM) duration and 10^{18} W/cm^2 peak intensity is used as the input. The field profile is shown in grey-filled curves. The simulations without ionization, with 1s ionization, and with 1s and 2p ionization are presented in three columns. Figure from Li et al. [2020b].

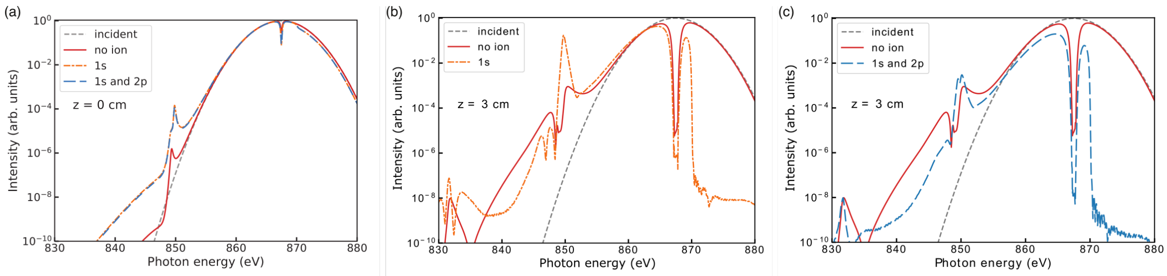

Figure 2.3: The spectrum at the beginning and the end of propagation for simulations without ionization, with 1s ionization, and with 1s and 2p ionization. Figure from Li et al. [2020b].

Fig. 2.2 and Fig. 2.3 show the difference between simulations with and without photoionization effects. Fig. 2.2 shows the populations of different states in the temporal domain. The grey-filled profile indicates the x-ray pulse. Without ionization, the pulse populates the $1s^{-1}3p$ state, which decays exponentially due to Auger decay. There is a small amount of population in $2p^{-1}3p$ state due to the Raman transition. The pulse is temporally reshaped as it propagates through the neon gas. There is ringing structure that appears at the tail of the pulse. This Burnham-Chiao oscillation has been studied in optical pulse resonant propagation (Burnham and Chiao [1969]). The formation of the ringing structure is due to the ultrashort x-ray pulse inducing a slow decay dipole oscillation which radiates with the opposite phase. The new field interferes with the initial field and introduces the new dipole radiation. These dipole radiations interfere with each other and generate the ringing structure.

The temporal and spectral profiles of the pulse changed when the ionizations were added. There is a considerable amount of the population transfer to the ion $1s^{-1}$ state due to inner shell photoionization. This ion core-hole states decay to the $2p^{-1}$ state and emit XRL photons at 849 eV. The XRL fields interfere with the transmitted fields leading to the finely oscillating structures. Both the field amplitude and the population decreased when adding the valence ionization. The effects of the ions can be clearly shown in the photon spectrum in Fig. 2.3, where more emission at 849 eV is observed.

In order to understand the peak intensity dependence of the resonant propagation, we simulated the resonant propagation of the 0.25 fs (FWHM) Gaussian pulse with peak intensity equals 10^{16}, 10^{18} and 10^{19} W/cm^2. As shown in Fig. 2.4, at low intensity, the incident Gaussian pulse is absorbed at the resonant frequency $\sim$ 867.5 eV with an absorption bandwidth equaling the core-excited state lifetime. The resonant absorption separates the spectrum into two parts which interfere with each other and lead to the ringing structure in the temporal domain. The photons with energy above the ionization threshold $\sim$ 870 eV are attenuated due to the photoionization. The spectral and temporal profile look different

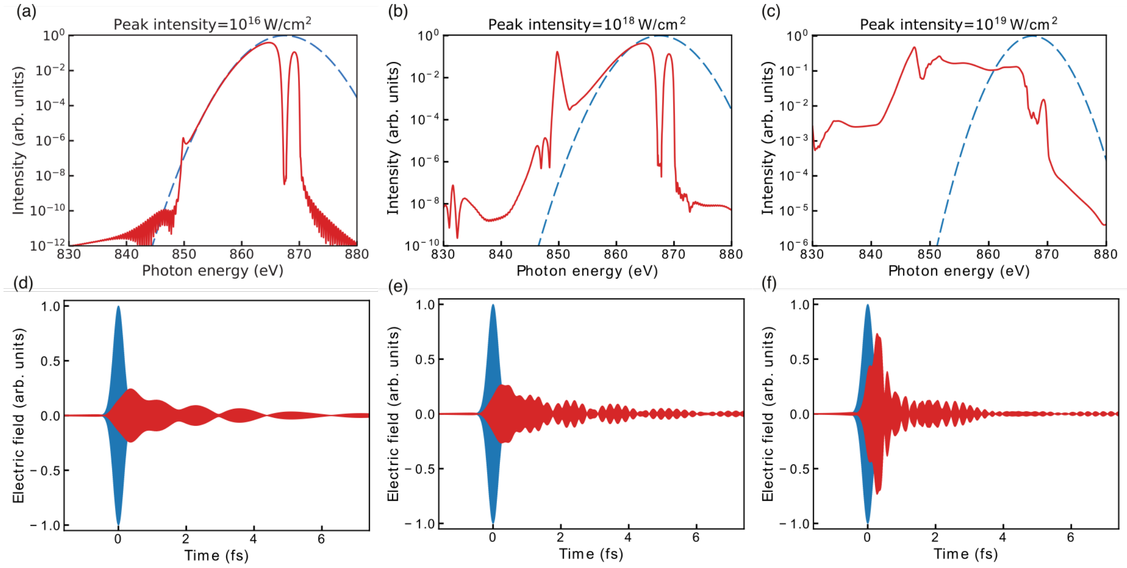

Figure 2.4: The simulation results for 0.25 fs Gaussian pulse with different peak intensities: 10^{16}, 10^{18} and 10^{19} W/cm^2. Figure from Li et al. [2020b].

at higher intensity. A strong emission including stimulated Raman and XRL peak appears at 849 eV, this leads to the fine interference structure in the temporal domain. With ultrahigh peak intensity at 10^{19} W/cm^2, Rabi oscillation occurs before Auger decay, which leads to the new emission at intermediate photon energies. This continuum emission leads to more transmission, as shown by the large transmitted pulse in the temporal domain.

The self-induced transparency (SIT) effect at different pulse intensities is shown in Fig. 2.5. The pulse energy decays as the x-ray propagates through the medium. Yet, the pulse energy attenuation deviates from the Beer–Lambert law, since the broad bandwidth pulse contains photons with energy out of the resonance absorption bandwidth that is not attenuated. However, the saturated absorption appears when the peak intensity is higher than the 10^{18} W/cm^2, which is close to a pi-pulse. Same as the optical SIT, the ultrahigh intensity pulse induces large population transfer. The depletion of the ground state population and the saturation of the excited states lead to a quench of transition and thus reduced absorption. This explanation is confirmed by the simulations with 2.5 fs (FWHM) pulses, in which the SIT happens near the pi-pulse area with lower peak intensity. It is shown in the lower

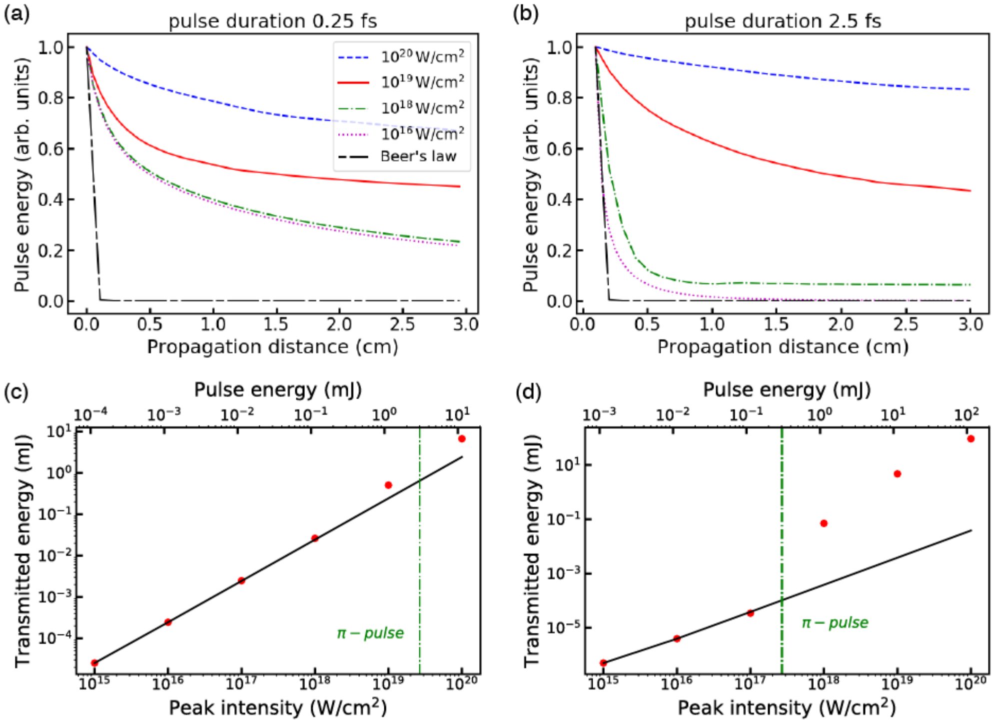

Figure 2.5: The pulse energy drops at the different propagation distances with 0.25 fs and 2.5 fs Gaussian pulses. The transmitted pulse energy deviates from the linear transmission when the incident peak intensity is close to or above the intensity corresponding to a pi-pulse. Figure from Li et al. [2020b].

panel that the transmitted pulse energy deviates from the linear transmission when the pulse is higher than the pi-pulse.

The influence of peak intensity in the spectrum is clearly shown in the 2d map of spectrum evolution with respect to the propagation distance in Fig. 2.6. With 10^{18} W/cm^2, the incident pulse with photon energy around $1s \rightarrow 3p$ is absorbed quickly at the beginning of propagation, and the narrow linewidth stimulated Raman signal grows as the pulse propagates. However, with 10^{19} W/cm^2, the resonant absorption happens slower, and the stimulated Raman line develops a continuum intermediate spectrum bridging the Raman and the transmitted incident. The stimulated Raman and the XRL pulse energy gain exponentially in the first 0.5 cm before saturation.

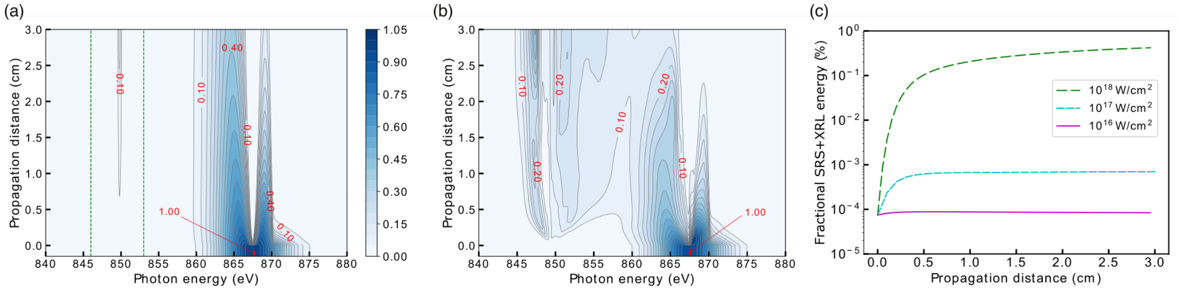

Figure 2.6: The 2d map of the spectrum as a function of propagation distances with peak intensity at 10^{18} (a) and 10^{19} W/cm^2 (b). (c) the gain of stimulated Raman and XRL pulse energy as the pulse propagates. Figure from Li et al. [2020b].

With the incident pulse duration shorter than the lifetime of core-excited states, the impulsive stimulated Raman and XRL process finished before the Auger decay, thus maximizing the emission signal. To explore the influence of the pulse duration, the Gaussian pulse with 2.5 fs (FWHM) duration is used in resonant propagation simulations with different peak intensities. As shown in Fig. 2.7, at low intensity, the incident pulse is drastically attenuated by the dense neon gas due to the resonance absorption. This leads to the ringing structure in the temporal domain. At higher intensity, a strong stimulated Raman and XRL are generated with an intensity higher than the transmitted incident pulse. This means that we obtain a pulse at the new photon energy. With 10^{19} W/cm^2 intensity, the self-induced transparency happens, and the pulse duration is compressed due to the nonlinear propagation.

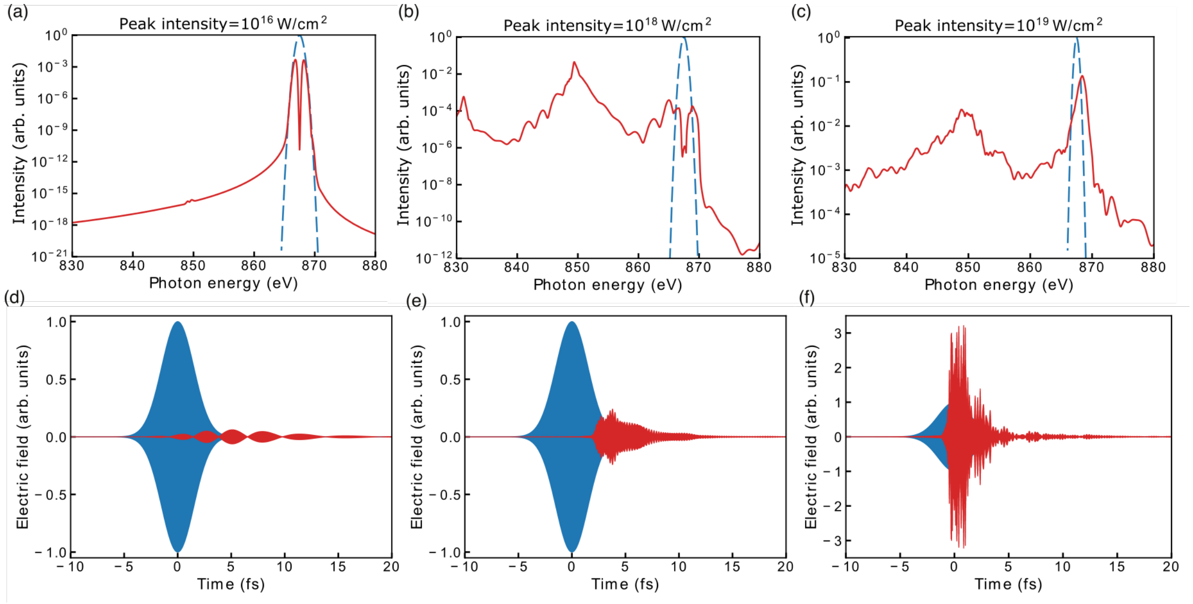

Figure 2.7: The output spectrum and temporal profile of the fields for a 2.5 fs (FWHM) Gaussian pulse with different peak intensities: 10^{16}, 10^{18} and 10^{19} W/cm^2. Figure from Li et al. [2020b].

Extending the 1d simulations to 3d offers us a unique opportunity to investigate the transverse profile reshaping in the resonant propagation. The evolution of the beam size for a 0.25 fs Gaussian pulse during the resonant propagation is shown in Fig. 2.8 (a). At low peak intensity, the pulse is focused to the center of the gas cell and then the beam size increases due to diffraction. At moderate intensity $\sim 10^{18}$ W/cm^2, the beam is focused down to a smaller size monotonically. With high peak intensities ($\sim 10^{19}$, 10^{20} W/cm^2), the beam size changes dramatically. It oscillates with a minimum of around 0.5-1.0 µm. The self-focusing (SF) effects are further confirmed by the increasing of the on-axis electric field amplitudes as the beam spot shrinks.

To gain insights into the physics behind the SF during resonant propagation, we simplify our neon atom to a 2-level system. Similar to before, a 0.25 fs (FWHM) Gaussian pulse with central photon energy resonant with the 2-level transition is used. The pulse energy, beam

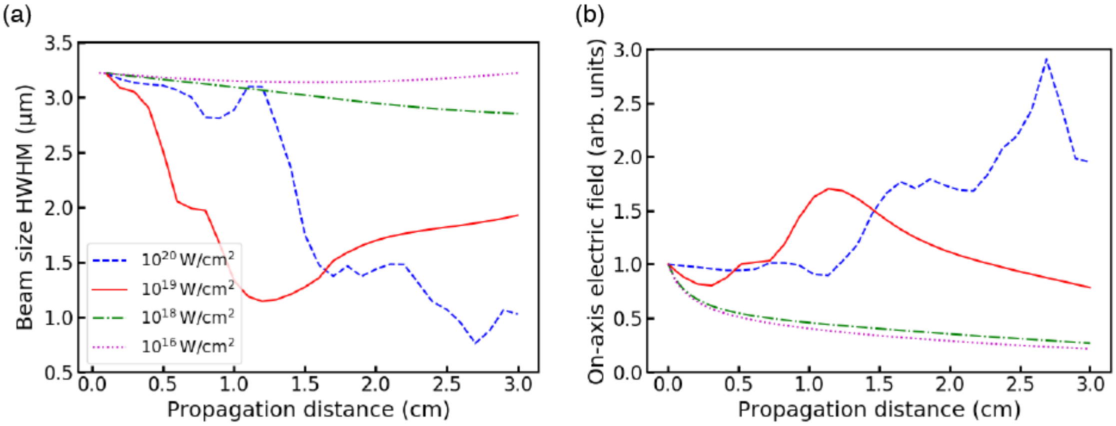

Figure 2.8: The beamsize and on-axis electric field amplitudes as a function of the propagation distances simulated for different incident peak intensities. Figure from Li et al. [2020b].

size, and the on-axis field intensity changes as a function of the propagation distance are shown in Fig. 2.9. As expected, the SIT and SF happen with high incident peak intensity. However, the beam size drops monotonically, instead of complex oscillation in the case of a 3-level system including Raman transition.

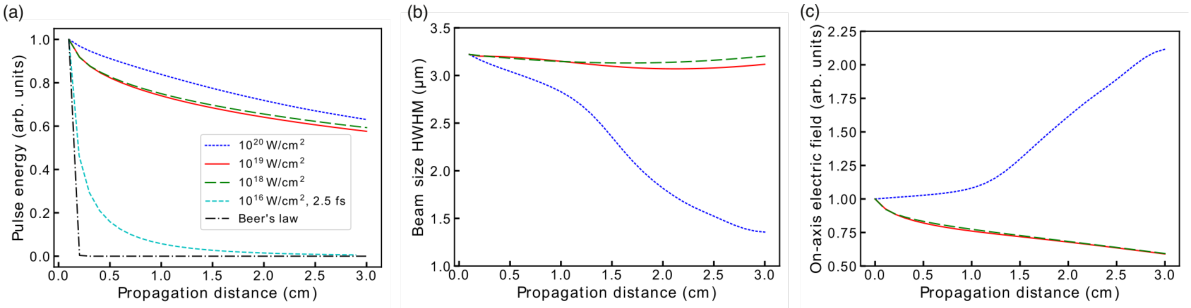

Figure 2.9: The pulse energy, beam size and on-axis electric field amplitude at different propagation distances. The simulation is performed with a 2-level system. Figure from Li et al. [2020b].

The SF can be explained by the wavefront modification of the field in the process of resonant propagation. The beam transverse profile and the phase at different propagation distances are shown in Fig. 2.10. The beam profile is reshaped from a broad input Gaussian to a triangle profile with a smaller size, where the high intensity at the center drops quickly as the radial distance increases. This could be explained by the change in the phase of the pulse at different radial positions. The different field intensities at the different radial coordinates experience a different modification of the phase. The change of the wavefront leads to the evolution of the beam size as it propagates. Note that this resonant phase changing due to strong field-matter interaction is different from the Kerr effect, which is the off-resonant self-focusing due to the intensity dependence of the susceptibility.

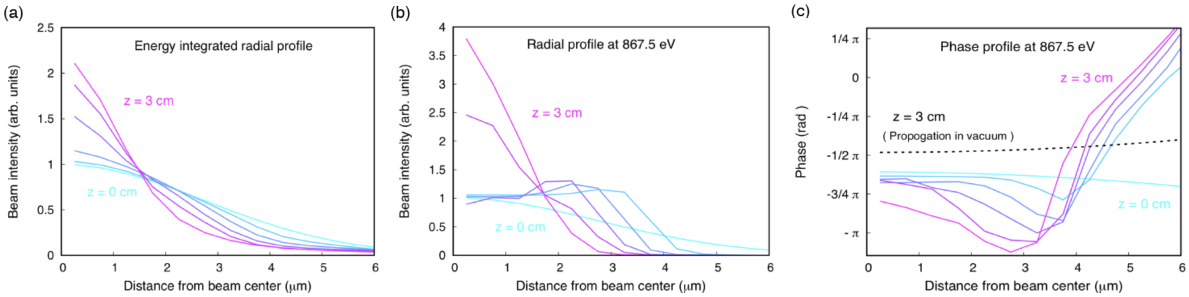

Figure 2.10: The transverse beam profile and the phase of the wavefront changes at different propagation distances. Figure from Li et al. [2020b].

2.3 Resonant propagation of XFEL pulses

The versatile code we developed is suitable for simulating the propagation of pulses with random profiles. The ultrashort Gaussian x-ray pulses used in the calculations above are not available yet. Most of the XFELs generate SASE x-ray pulses, that contain spikes that fluctuate randomly. The SASE pulses can be simulated by the chaotic radiation modeling algorithm (Vannucci and Teich [1980], Pfeifer et al. [2010]). The radiation field amplitudes of a SASE pulse at different frequencies are randomly generated by Gaussian sampling. At each frequency, the variation of the Gaussian sampling equals the intensity of the averaged power spectrum of the SASE. The phase of the spectrum varies randomly within $[0, 2\pi]$ from point to point. The SASE pulse is first generated in the frequency domain and then an inverse Fourier transform is applied to obtain the electric fields in the temporal domain. A Gaussian mask with a pulse duration equal to the averaged SASE is applied to obtain the right temporal pulse duration. The temporal field after masked is Fourier transformed back to the frequency domain to obtain the final spectrum.

The algorithm mentioned above is applied to generate SASE pulses with 10 fs (FWHM) duration. In XFELs, the averaged SASE spectrum has a bandwidth of around 0.5% of the central photon energy. Thus for central photon energy at 867.5 eV, a spectral bandwidth of 4.3 eV is used in the simulation. A typical simulated SASE pulse is shown in Fig. 2.11 by the blue lines, which have random spikes in the temporal and spectral domain. The duration of the coherent spike ($\sim$ 1 fs) is determined by the averaging bandwidth in the spectral domain, while the spectral spike bandwidth ($\sim$ 0.4 eV) is defined by the averaged duration of the pulse in the temporal domain.

The SASE pulse with central photon energy at 867.5 eV propagates through a 1 bar neon gas and the output of the simulation is shown in Fig. 2.11 by red lines. With pulse energy equal to 5 mJ, the peak intensity of the SASE is around 10^{19} W/cm^2. As in the case of Gaussian pulse, a strong XRL and stimulated Raman emission signal appear around 849 eV. The output pulse has inherent random fluctuating spikes from the SASE both in the temporal and spectral domains. Due to the dispersive relation in Raman scattering, the spikes in the Raman spectrum resemble the incident SASE. This feature is used to obtain a high-resolution stimulated Raman spectrum in the later chapter.

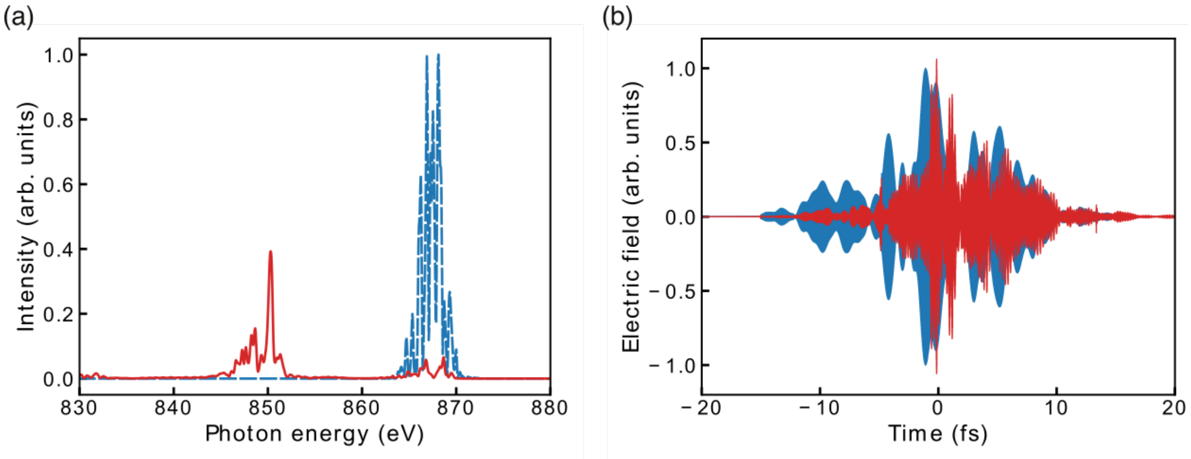

Figure 2.11: The resonant propagation simulation results of a SASE pulse with 10 fs (FWHM) duration and 10^{19} W/cm^2 peak intensity. Figure from Li et al. [2020b].

In order to observe the interesting pulse-reshaping phenomena revealed by Gaussian simulations, a high-intensity ultrashort coherent x-ray pulse is required. The generation of such XFEL pulses has been demonstrated recently at LCLS using the electron beam nonlinear compression in the magnets (Duris et al. [2020]). The FEL simulation code Genesis (Reiche [1999]) is used to simulate the X-ray laser-enhanced attosecond pulse generation (XLEAP) at LCLS. The XLEAP pulses with peak intensity at 6×10^{16}, 4×10^{18} and 4×10^{19} W/cm^2, and pulse duration ~ 0.5 fs are generated. The averaged pulse profile of 20 shots is shown in Fig. 2.12 by blue lines. These shots are fed into our TDSE-MWE code as inputs with photon energy centered at 867.5 eV, resonant with the neon $1s \rightarrow 3p$ transition. The outputs of single-shot passing through a 1 bar 1 cm neon gas cell are represented by the grey lines. The averaged output is plotted in red lines. For low intensity ($\sim 6 \times 10^{16}$ W/cm^2), due to the resonant absorption, the pulse is reshaped in the temporal domain to have the ringing tails. At intermediate intensity ($\sim 4 \times 10^{18}$ W/cm^2), the stimulated Raman and XRL emission appears and the pulse obtains fine temporal oscillating structures. At high intensity ($\sim 4 \times 10^{19}$ W/cm^2), the emission spectrum becomes broad, and the pulse is relatively short in the temporal domain. Overall, the outputs are close to the simulation results of a Gaussian pulse.

The temporal reshaping of the XLEAP pulse resonant propagating through the neon can be monitored by the laser streaking technique at LCLS (Li et al. [2018]). The reshaped pulse ionizes a dilute gas, and the photoelectrons are kicked around by the IR laser pulse. The photoelectron momentum distribution is measured to obtain the pulse spectrum and temporal profile. The streaking simulation results of 3 reshaped XLEAP pulses are shown in Fig. 2.13. Clearly, the photoelectron momentum distribution measured looks different for different reshaped pulses. Some reconstruction algorithms can be used to extract the spectral and temporal information of the reshaped pulse (Li et al. [2018]).

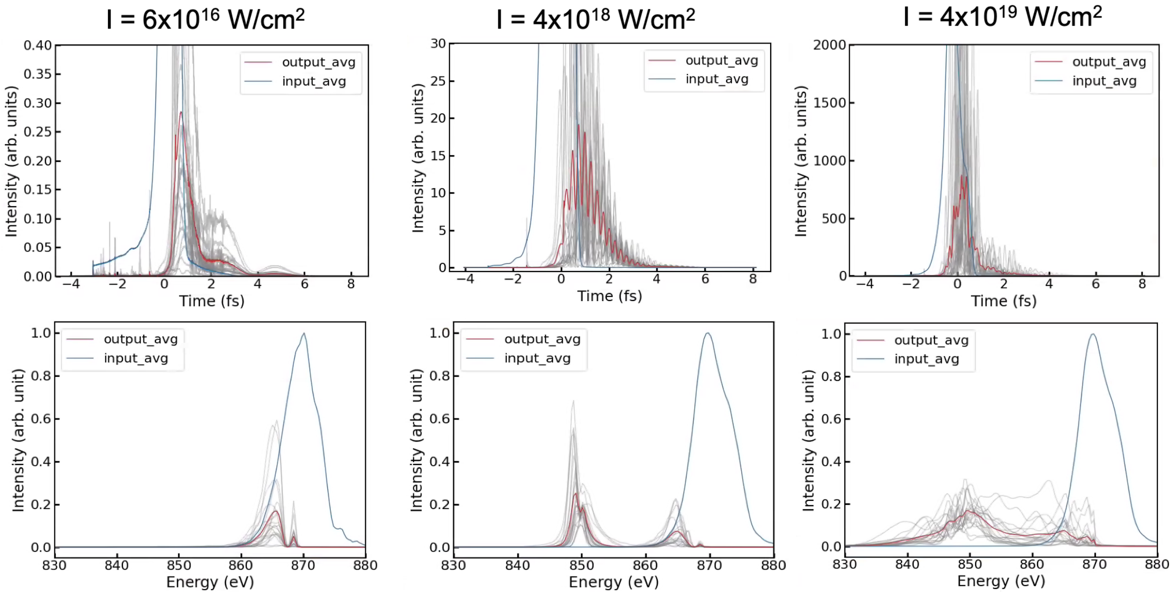

Figure 2.12: The resonant propagation simulation results for XLEAP pulses with different peak intensities: 6×10^{16}, 4×10^{18} and 4×10^{19} W/cm^2.

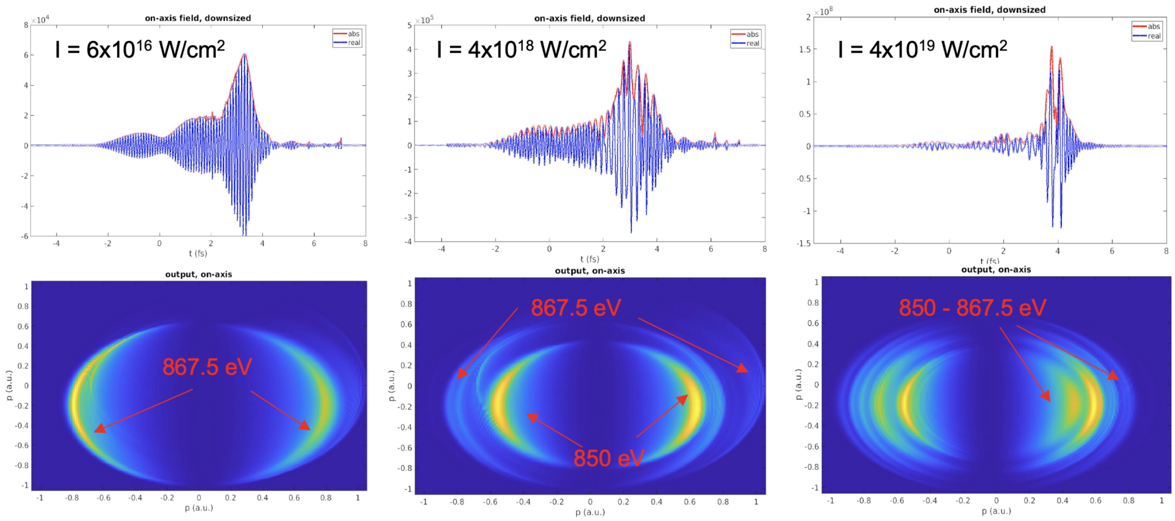

Figure 2.13: The single shot XLEAP pulses at different intensities and their corresponding simulated IR laser streaking momentum distribution.

CHAPTER 3

HIGH-RESOLUTION STIMULATED X-RAY RAMAN SPECTROSCOPY (SXRS)

Optical Raman spectroscopy has proved to be a powerful tool in probing molecular vibronic states. Extending this technique to the x-ray regime would benefit studies of valence electronic states. Due to the extremely small x-ray inelastic scattering cross-section, x-ray spontaneous Raman spectroscopy is a photon-hungry technique. With stimulated emission, the exponentially amplified SXRS in dense media is demonstrated with a signal increase of eight orders of magnitude. The energy resolution of the Raman spectroscopy is determined by the incident pulse bandwidth. To obtain a high-resolution SXRS, the covariance function between SASE spectrum and stimulated Raman is realized.

An experimental demonstration of SXRS in dense neon gas with SASE pulses was performed in the European XFEL SQS endstation. The photon spectrum of the transmitted SASE and stimulated Raman emission are measured by a grating spectrometer. The covariance analysis reveals the SXRS with unprecedented energy resolution. A supercomputer simulation was used to confirm our observation as well as provide more insights into the SXRS physics and point ways to further improve the SXRS.

3.1 Principle of SXRS using stochastic SASE pulses

In quantum optics, the Raman scattering cross-section is calculated by the Kramers–Heisenberg formula:

$$\frac{d^2\sigma}{d\omega_f d\Omega} = \alpha^4 \frac{\omega_f}{\omega_i} \left| \sum_m \frac{\langle f| \mu_{fm} |m\rangle \langle m| \mu_{mi} |i\rangle}{E_i - E_m + \omega_i - i\Gamma_m/2} \right|^2 \delta(E_f + \omega_f - E_i - \omega_i) \tag{3.1}$$

which uses perturbation theory to describe the differential cross-section for scattering an incident photon $|k_i\rangle$ to state $|k_f\rangle$ with a corresponding atomic transfer from initial state

$|i\rangle$ to $|f\rangle$. In the equation, α is the fine structure constant, ω_i and ω_f is the incident and scattered photon energy. μ is the atomic transition dipole moment. E_i, E_m and E_f are the initial, intermediate and final energies of the atomic state. Γ_m is the decay rate of the core-excited states. Since there is no electron ejected to carry away the energy, the total energy of the atom+photon system should be conserved. This is enforced by the δ function at the end of the formula.

One important feature of x-ray Raman scattering or resonant inelastic x-ray scattering (RIXS) is that the resolution of the scattered photon spectrum is not limited by the lifetime of the core-excited states, since the Raman process promotes electrons from the ground state to the valence-excited states, which have lifetimes beyond our energy resolution. Instead, the energy resolution is determined by the incident beam bandwidth. This is essentially due to the energy conservation. To see this, we consider the incident beam spectral density as a Gaussian function:

$$I_i(\omega_i) = I_0 \exp\left(-\frac{(\omega_i - \omega_0)^2}{2\sigma_0^2}\right) \tag{3.2}$$

with center photon energy ω_0 and bandwidth σ_0. The photon number around energy ω_i is $n_{k_i} = I_i(\omega_i)\, d\omega_i$. Since each photon scatter according to the Kramers–Heisenberg formula, the total beam scattering differential cross-section is:

$$\begin{aligned}\frac{d^2\sigma}{d\omega_f d\Omega} &= \alpha^4 \int \frac{\omega_f}{\omega_i} \left| \sum_m \frac{\langle f|\, \mu_{fm} \,|m\rangle \,\langle m|\, \mu_{mi} \,|i\rangle}{E_i - E_m + \omega_i - i\Gamma_m/2} \right|^2 \\ &\qquad \times I_i(\omega_i)\, \delta(E_f + \omega_f - E_i - \omega_i) d\omega_i \\ &= \alpha^4 \frac{\omega_f}{E_f - E_i + \omega_f} \left| \sum_m \frac{\langle f|\, \mu_{fm} \,|m\rangle \,\langle m|\, \mu_{mi} \,|i\rangle}{E_f - E_m + \omega_f - i\Gamma_m/2} \right|^2 \\ &\qquad \times I_0 \exp\left(-\frac{(E_f - E_i + \omega_f - \omega_0)^2}{2\sigma_0^2}\right)\end{aligned} \tag{3.3}$$

which means the scattering cross-section is essentially a Gaussian function, centered at the incident minus the energy loss and bandwidth equals the incident, modulated by the broad Lorenzian profile centered at the atomic resonance with bandwidth determined by core-excited states lifetime. It clearly shows that the scattering spectrum ω_f can have a bandwidth close to the incident, which might be smaller than the core-excited states' lifetime broadening.

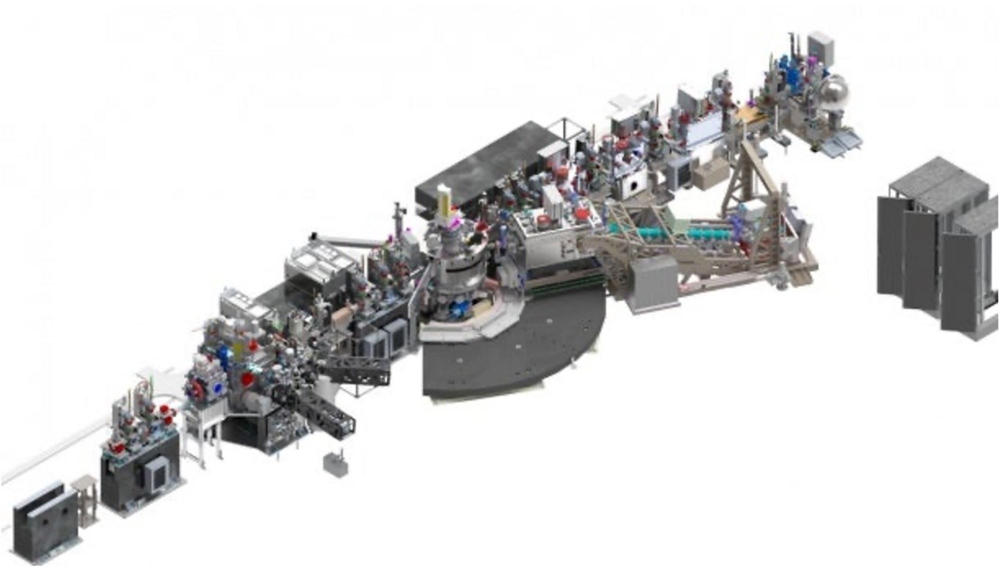

Figure 3.1: The schematic of the experimental setup of RIXS spectroscopy (chem-RIXS/qRIXS at LCLS). The monochromator is used to get a narrow incident beam from the SASE pulses. The movable spectrometer is employed to measure the scattered photon spectrum.

RIXS spectroscopy is a powerful technique based on the Kramers–Heisenberg formula to measure the electronic, magnetic and structural properties of quantum materials and molecules. A typical experimental setup includes an incident monochromator to get a narrow bandwidth incident beam, a photon sample interaction chamber, and an adjustable spectrometer to measure the spectrum of the scattered photon. To measure the spectrum with a sub-lifetime resolution, a high-resolution monochromator with resolving power 50000 to 2000 is required. Another high-energy resolution spectrometer is needed to obtain a high-resolution spectral measurement. The energy of the incident monochromatic beam is scanned to cover the spectral area of interest. Due to the very small spontaneous inelastic scattering cross-section, RIXS spectroscopy is usually very photon-hungry and time-consuming.

Stimulated X-ray Raman Spectroscopy (SXRS) has a cross-section that is orders of magnitude higher than the spontaneous x-ray Raman scattering. The ultrafast SXRS has been proposed in Zhang et al. [2014], where multiple coherent attosecond x-ray pulses are required. However, the generation of delay-controllable multiple coherent attosecond XFEL pulses is challenging and not available yet.

An alternative way is to use SASE XFEL pulses with covariance analysis to obtain a high-resolution x-ray spectrum (Kimberg and Rohringer [2016], Cavaletto et al. [2021]). As shown in Fig. 3.2, the incident SASE pulse contains many spikes, each individual spike acts as an ultrashort Gaussian pulse and makes a stimulated signal itself. Due to energy conservation, the stimulated Raman signal has a specific energy loss corresponding to excitations in the target with respect to the photon that induced the Raman transition. As a result, the stimulated Raman signal resembles the incident SASE pulse. This correlation between the incident SASE and the stimulated Raman signal can be used to obtain a high-resolution spectrum.

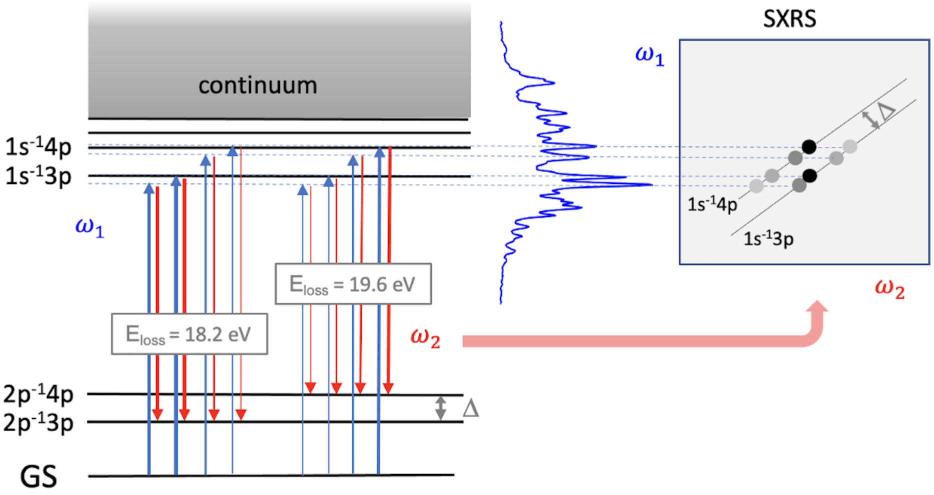

Figure 3.2: The principles of the high energy resolution stimulated x-ray Raman spectrum using stochastic pulses. The incident SASE pulse covers the transitions from the ground state to the core-excited states. The emitted stimulated Raman spectrum resembles the incident SASE. Each SASE spike generates a corresponding Raman emission spike. The covariance analysis can be used to extract a dispersive line with constant energy loss for each energy level.

Instead of plotting the averaged output stimulated Raman as a function of the incident SASE central photon energy, which gives poor energy resolution ($\sim 7eV$) determined by the broad SASE (Weninger et al. [2013]), the covariance function between incident photon spectrum $I(\omega_i)$ and stimulated Raman spectrum $I(\omega_r)$ can be calculated $Cov(I(\omega_i), I(\omega_r)) \equiv \langle I(\omega_i)I(\omega_r)\rangle - \langle I(\omega_i)\rangle\langle I(\omega_r)\rangle$. This covariance analysis is expected to give a stimulated Raman spectrum with energy resolution limited by the SASE spike bandwidth (~ 0.1 eV), which is the inverse of the pulse duration ($\sim h/\tau \sim 4.13\text{eV} * \text{fs}/40\text{fs} \sim 0.1\text{eV}$).

3.2 Experiment in European XFEL

The experiment of resonant propagation of SASE XFEL pulses in the neon gas is performed at the European XFEL (Decking et al. [2020], Tschentscher et al. [2017]) SQS (small quantum system) endstation (Mazza et al. [2023]). The experimental setup is shown in Fig. 3.3. The center photon energy of the incident SASE pulses is around 867.5 eV, resonant with the neon $1s \rightarrow 3p$ transition. The averaged pulse energy is 3 mJ with $\sim 3\%$ fluctuation from shot to shot. The pulse energy on the sample is controlled by the gas attenuator (GATT), where the incident pulse is attenuated by photoabsorption. The Kirkpatrick–Baez mirror (K-B mirror) is applied to focus the x-ray to a 1-2 µm spot size at the center of the gas cell. The gas cell with 4.5 mm length can hold neon gas with pressure up to ~ 6 bar. The transmitted x-ray beam is further attenuated by Al filters with thicknesses 3.5, 5, and 10 µm (transmission equals 0.173, 0.081, and 0.006 at 850 eV). The beam is transversely confined by a slit ~ 10 µm, before being dispersed by a grating. The spectrum is measured by a soft X-ray Andor detector with 2048*512 active pixels and a 13.5*13.5 um pixel size.

In the experiment, the central photon energy of the incident SASE pulse is scanned from 840 eV up to 960 eV. Considering the ~ 7 eV bandwidth of the SASE, a 5 eV scanning step was taken. The pressure of the neon gas is adjusted from 0.05 bar (the single atom response regime) up to 6 bar (the propagation pulse reshaping regime). The pulse energy ranging

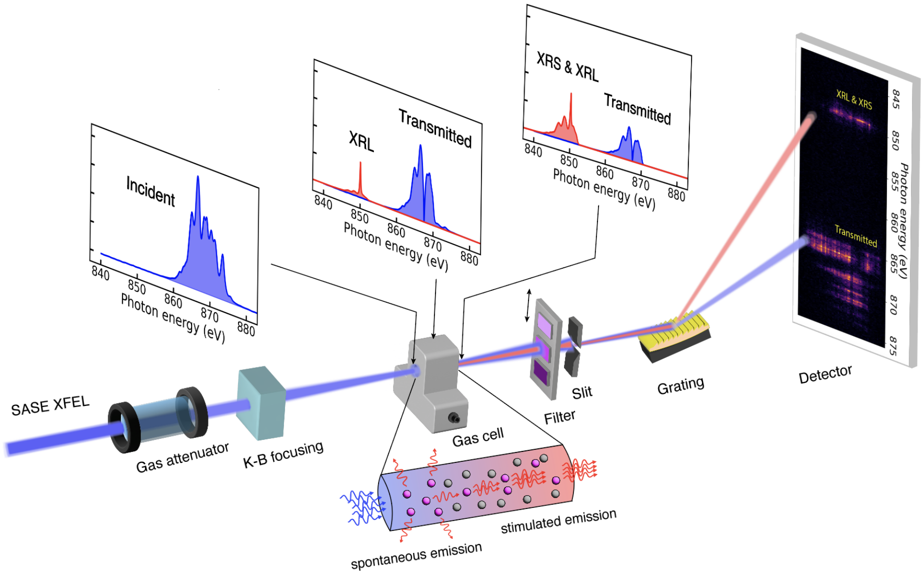

Figure 3.3: The schematic of experimental setup for the resonant propagation of SASE pulses through dense neon gas. The incident pulse intensity is adjusted by the gas attenuator (GATT), and then focused on the center of the gas cell by the K-B mirror. The transmitted and emitted photons pass through the Al filter and slit before being measured by a grating spectrometer. A typical spectrum recorded contains the transmitted incident around 867.5 eV and the XRL+stimulated Raman emission around 849 eV.

from 1% to 100% is controlled by the GATT. The matrix of data taken is represented in Fig. 3.4.

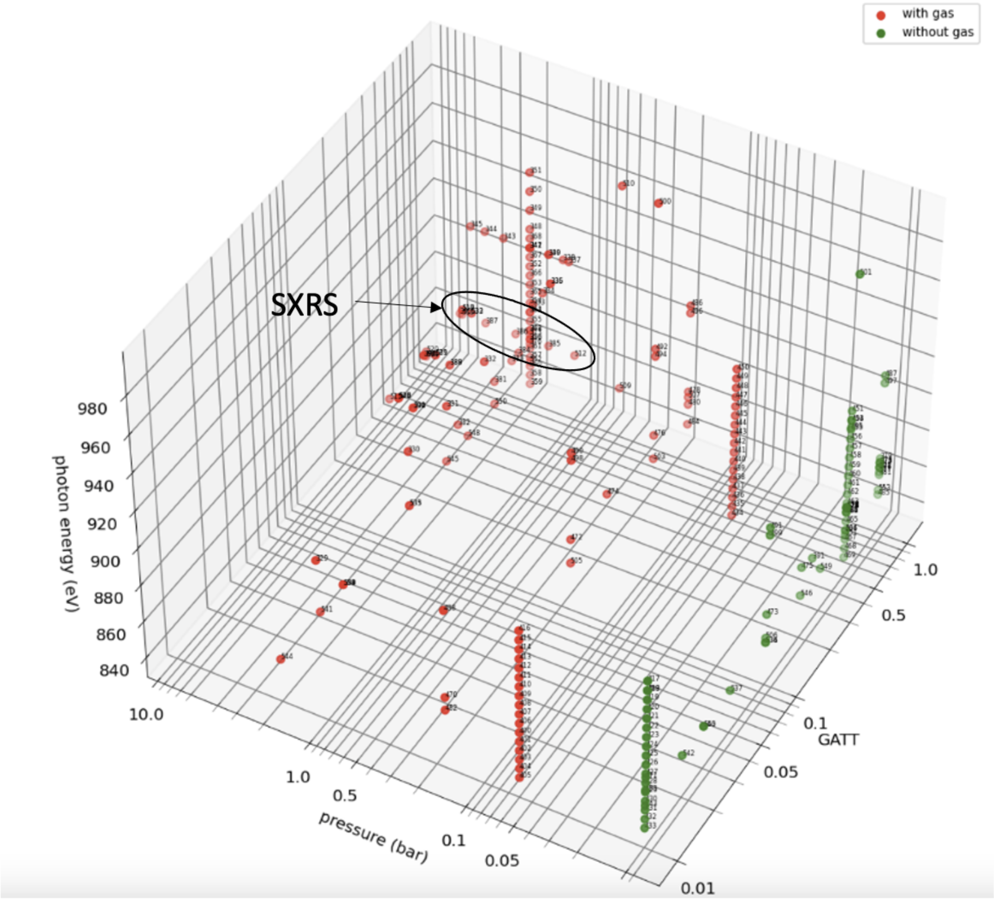

Figure 3.4: The 3D matrix of the experimental conditions where the data is taken. We scanned the neon gas pressure from 0.05 bar (single atom response) up to ∼ 6 bar (propagation regime). The central photon energy is adjusted from 840 eV to 860 eV with ∼ 5 eV steps. The gas attenuator is set in the range from 1% (linear response) up to 100% (nonlinear response).

Covariance analysis requires the spectra of thousands of shots. To record the spectra with 10 Hz repetition rate, the 2d detector with 512 pixels along the non-dispersive spatial direction was binned into 64 bins. The 2048 active pixels along the dispersive direction are kept to ensure a high energy resolution (∼ 0.2 eV). Spectra of around 18,000 shots, which take 30 mins, are recorded for each SXRS run.

3.3 Experimental results

With high-intensity SASE XFEL pulses ($\sim 10^{18}$ W/cm^2), a 1s core hole is created which can be refilled by spontaneous radiation and be amplified exponentially via propagation. The incident SASE pulse resonantly populates the core-excited $1s^{-1}3p$ state, which decays either by ejecting an Auger electron or emitting a photon through a spontaneous Raman transition $1s^{-1}3p \rightarrow 2p^{-1}3p$. The spontaneous Raman stimulates a Raman transition in the atoms and the emission signal is amplified exponentially as the pulse propagates through the neon gas. The incident SASE has a broad bandwidth ($\sim$ 7 eV) that covers the 867.5 eV $1s \rightarrow 3p$ transition as well as the 870 eV K-edge. The incident photons with energy above the photoionization threshold will create a population inversion between $1s^{-1}$ and $2p^{-1}$ in the Ne^{+1}. The spontaneous emission from the ion can stimulate the transition in the atoms and the XRL signal is amplified exponentially.

The pulse energy contained in XRL+SXRS as a function of different incident peak intensities is shown in Fig. 3.5. The blue dots represent the total emission energy of single shots, with the average of the top 10% shown in the red line. The XRL and SXRS pulse energy are shown in purple and green, respectively. As expected, the emission pulse energy grows exponentially as the peak incident intensity increases. The simulation results with 0.25 fs Gaussian pulse and with pulse energy are shown in grey dots and squares, respectively. These two lines track each other with the SASE $\sim$ 20 times bigger than the Gaussian, which indicates that the resonant propagation of a SASE pulse mimics the propagation of a set of Gaussian pulses.

The absolute emission yield is obtained by energy calibration of the detection system by varying the incident pulse energy without the neon gas. As shown in Fig. 3.6, the GATT is used to modify the incident SASE pulse energy, and different Al filters are applied to optimize the signals on the detector. The incident pulse energy detected by the GMD (gas monitor detector) as a function of the integral signal on the detector shows a linear relation.

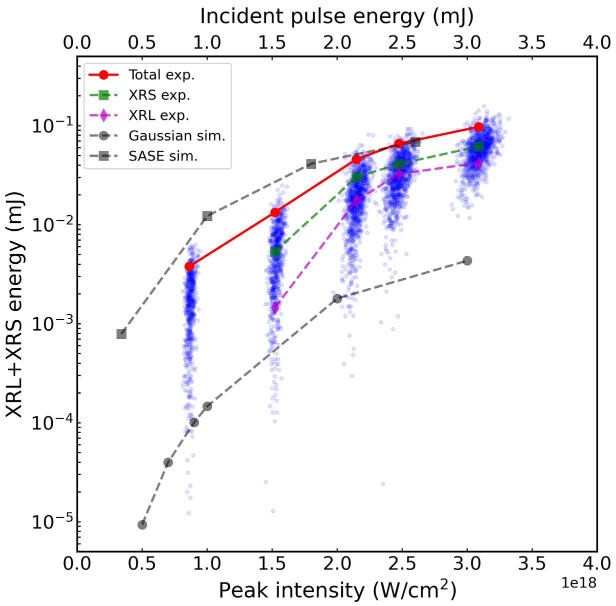

Figure 3.5: The XRL+SXRS pulse energy as a function of the incident SASE peak intensity. The experimental single-shot results are shown by the blue dots. The average of the top 10% emission is shown in red dots, which can be separated by the contributions from XRL (purple diamond) and SXRS (green square). The simulation results with the SASE pulse are close to the experimental measurements. The emission from SASE is around 20 times bigger than the emission from a Gaussian pulse with 0.25 fs duration. This implies that the SASE pulse can be represented by multiple Gaussian pulses during the interaction.

A linear fit to the data gives a calibration from the signal detected to the pulse energy, which is then used to obtain the XRL+SXRS emission energy. An alternative way to estimate the yield is by calculating the detector counts as a function of the incident photon number. This approach gives a result close to our calibration.

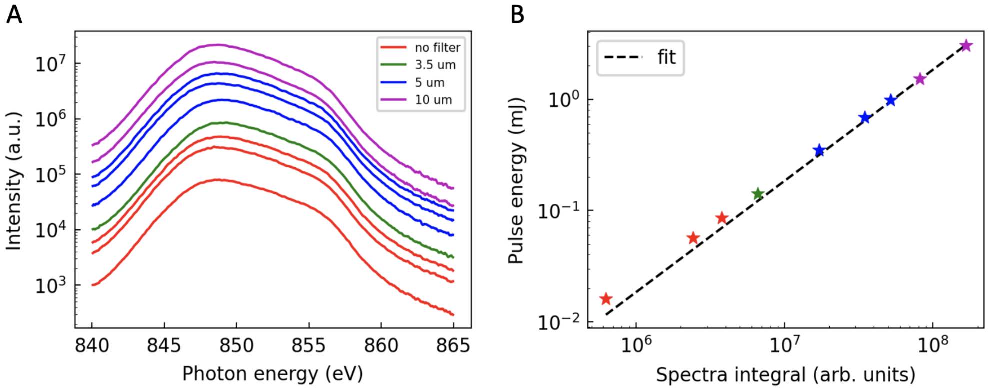

Figure 3.6: The averaged SASE spectra with different GATT and the Al filters. The integral spectral signal is linearly proportional to the pulse energy characterized by the gas monitor detector. This relation is used to calibrate the XRL+SXRS pulse energy.

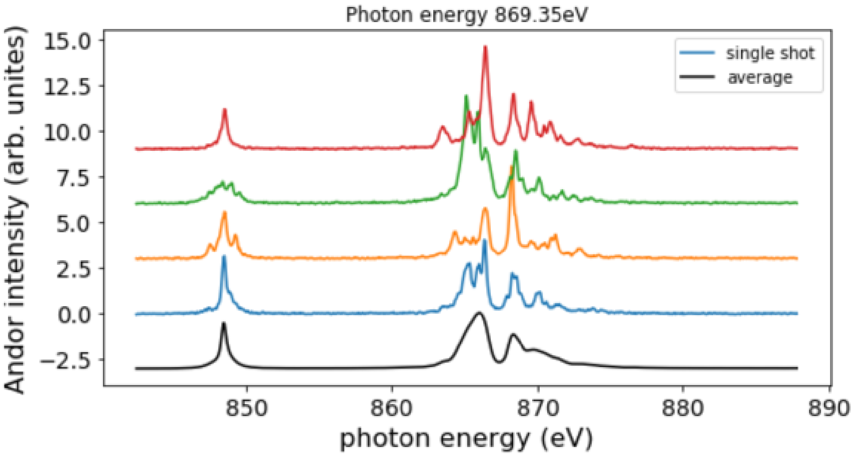

Figure 3.7: The typical single shots and averaged spectrum measured. The incident SASE is centered around 870 eV, the gas pressure is 2 bar and the GATT=100%.

In the experiment, the incident SASE photon spectrum varied from shot to shot. The incident spectrum was not characterized. The only observable is the transmitted spectrum. A typical averaged and single-shot output spectrum are shown in Fig. 3.7. With incident center photon energy at 869 eV, the resonant absorption of $1s \rightarrow 3p$ and $1s \rightarrow 4p$ transition appears in the averaged spectrum. For the conditions of 2 bar pressure, 4.5 mm path length, and GATT=100% incident intensity, the stimulated emission has an intensity comparable to the transmitted incident. The single-shot spectrum contains random spikes that fluctuate from shot to shot.

A good way to extract information from the random fluctuation shots is by covariance analysis. Since the incident SASE spectrum is not characterized, we calculate the covariance of the transmitted incident $I(\omega_1)$ and the Raman $I(\omega_1)$:

$$Cov(I(\omega_1), I(\omega_2)) \equiv \langle I(\omega_1)I(\omega_2)\rangle - \langle I(\omega_1)\rangle\langle I(\omega_2)\rangle \tag{3.4}$$

where the symbol $\langle\rangle$ denotes the ensemble average over different SASE shots. To gain insight into the covariance calculated, we express the covariance function in terms of the incident spectra $I_i(\omega)$:

$$\begin{aligned} Cov(I(\omega_1), I(\omega_2)) &\propto Cov(I_i(\omega_1) * Tr(\omega_1), I_i(\omega_1) * \sigma_R(\omega_1, \omega_2)) \\ &= Tr(\omega_1) * \sigma_R(\omega_1, \omega_2) * Cov(I_i(\omega_1), I_i(\omega_1)) \\ &= Tr(\omega_1) * \sigma_R(\omega_1, \omega_2) * Var(I_i(\omega_1)) \end{aligned} \tag{3.5}$$

where $Tr(\omega_1)$ represents the transmission of the neon gas, $\sigma_R(\omega_1, \omega_2)$ denotes the stimulated Raman scattering cross-section of the neon gas from a photon at ω_1 to ω_2, and $Var(I_i(\omega_1))$ represents the variation of the incident spectrum. From this, we can obtain the stimulated

Raman cross-section as follows:

$$
\begin{aligned}
\sigma_R(\omega_1, \omega_2) &\propto Cov(I(\omega_1), I(\omega_2))/(Tr(\omega_1) * Var(I_i(\omega_1))) \\
&= Cov(I(\omega_1), I(\omega_2))/(Tr(\omega_1) * Std(I_i(\omega_1))^2) \\
&\propto Cov(I(\omega_1), I(\omega_2))/(Tr(\omega_1) * \langle I_i(\omega_1)\rangle^2) \\
&= Cov(I(\omega_1), I(\omega_2))/\langle I(\omega_1)\rangle * \langle I_i(\omega_1)\rangle \\
&\approx Cov(I(\omega_1), I(\omega_2))/\langle I(\omega_1)\rangle \qquad (3.6)
\end{aligned}
$$

where $Std(I_i(\omega_1))$ is the standard deviation of the incident spectra. The standard deviation is assumed to follow Poisson distribution and is frequency independent, thus can be approximated by the averaged spectral value. In the last step, we ignored the dividing of the averaged incident spectrum $\langle I_i(\omega_1)\rangle$ since we are focusing on the high-resolution spectrum and they only gave a broad background.

The covariance between the transmitted incident and the Raman normalized to the averaged transmitted spectrum (normalized covariance) is calculated according to Eq. (3.6) and shown in Fig. 3.8. The incident SASE pulse has 6 mJ energy. The beamline transmission is around 0.5, thus the SASE pulse on target has 3 mJ energy. The neon pressure was set to be 1.0, 1.5 and 2.0 bar.

As shown in Fig. 3.8, the normalized covariance reveals the 3p dispersive line at an energy loss of 18.7 eV. The 4p Raman signal centered at 868.93 eV incident energy and 20.3 eV energy loss. The continuum emission line above 870 eV is the XRL signal. The normalized covariance map varies as the neon pressure changes. The 3p resonant Raman dispersive line resembles the spontaneous RIXS map at low pressure. The Raman signal extends over a larger energy region as the pressure goes up. Instead of a resonant enhancement at 867.29 eV incident energy, there is a hole interrupting the Raman dispersive line. With gas pressure above 1.5 bar, all signals above 868 eV disappeared for SASE pulses centered at 867.5 eV.

These artifacts are due to the absorption of the photons on and above the resonances, which leaves no transmitted signal to correlate with the Raman emission.

To recover the signals above the resonances, we combine the data from two runs with center photon energy 867.5 eV and 870 eV. The single-shot spectra from these two runs are added together to form a single-shot spectrum for the combined. These combined single-shot spectra are used to calculate the normalized covariance as shown in Fig. 3.9. With the central photon energy at 870 eV, more incident photons are above the ionization threshold, thus a stronger XRL signal is produced. Meanwhile, more signals are transmitted, which can be used to calculate the covariance. The resonant enhancement of the Raman from Rydberg states 4p 5p and 6p appears in the 869 to 870 eV incident photon area. Interestingly, a new dispersive line with 19.8 eV energy loss shows up. This feature is suspected to be related to the $3p \rightarrow 4s$ transition, which generates emission through $1s^{-1}4s$ intermediate state.

It is worth noting that different normalizations of the covariance generate the RIXS that highlight different features and convey different information. As shown in Fig. 3.10 (A). The normal covariance function $Cov(I(\omega_1), I(\omega_2)) \equiv \langle I(\omega_1)I(\omega_2)\rangle - \langle I(\omega_1)\rangle\langle I(\omega_2)\rangle$, reveals a clear 3p x-ray stimulated Raman dispersive line. However, some weak signal features, due to absorption, are not observable above the resonances and K-edge.

The covariance function, normalized to the average of the transmitted incident, according to Eq. (3.6), shown in Fig. 3.10 (B), provides a more detailed view of the stimulated Raman scattering cross-section. Notably, the 4p Raman scattering and the XRL lines are visible. However, due to the strong resonant absorption and the small on-resonant transmitted incident signals, it is challenging to observe the resonance enhancement signals. As a result of the normalization, artificial horizontal bands appear around the 3p, and 4p resonances.

Another way to normalize the covariance is by dividing both the average emission $I(\omega_2)$ and the transmitted incident $I(\omega_1)$, shown in Fig. 3.10 (C). While this formula preserves the symmetry of the covariance function and yields results similar to the Pearson correlation, it

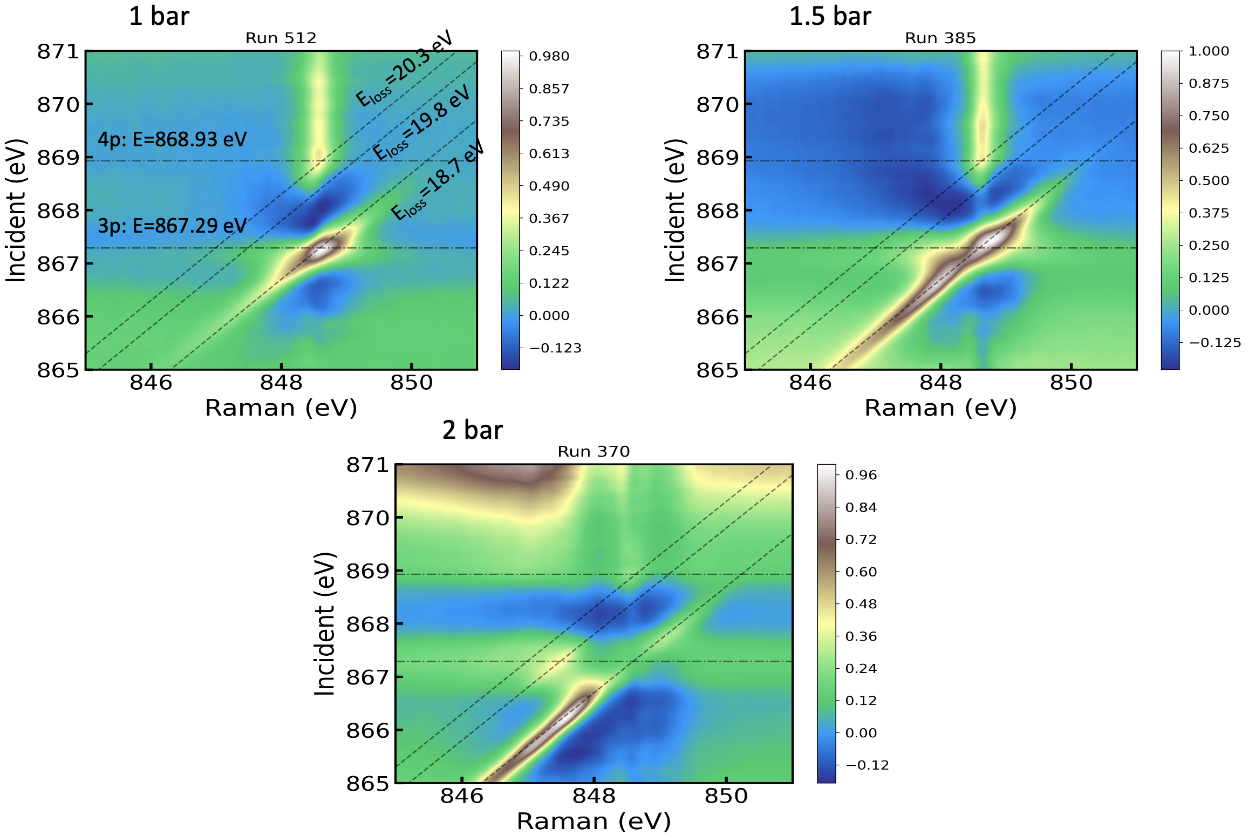

Figure 3.8: The normalized covariance map with different gas pressures (1.0, 1.5 and 2.0 bar). The covariance is calculated between the transmitted incident and the stimulated Raman signals, then normalized to the average spectrum of the transmitted.

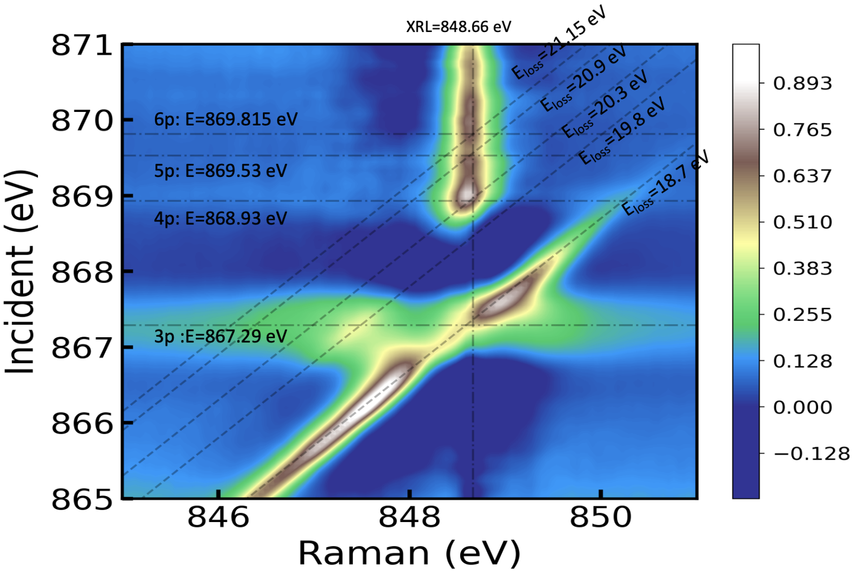

Figure 3.9: The normalized covariance for the spectra combined the runs with photon energy centered at 867.5 and 870 eV.

amplifies the background excessively and obscures the resonance-enhanced dispersive Raman and XRL lines.

The normalization of the covariance to the square of the averaged transmitted incident ($\langle I(\omega_1) \rangle$) is presented in Fig. 3.10 (D). This normalization yields values that can be interpreted as the square of the percentage fluctuation, i.e. the standard deviation over the mean. Notably, this double normalization of the covariance reveals clear resonance enhancement of Raman scattering with a peak amplitude of around 0.09, which is close to the square of the peak percentage fluctuation 33%.

The energy resolution of the Raman spectroscopy is measured by the FWHM of the dispersive line. A Gaussian fit is applied to the horizontal lineouts of the normalized covariance. The FWHM of the Raman line is found to be 0.41 eV. According to Lutman et al. [2012], the FWHM of the correlation $\sim \sqrt{\frac{1}{2\,\sigma_t^2} + 2\,\sigma_s^2}$. Where σ_t is the FWHM of the SASE pulse duration; σ_s is the FWHM of spectrometer instrumental broadening. With $\sigma_t \sim 40$ fs and $\sigma_s \sim 0.2$ eV, the calculation gives FWHM ~ 0.3 eV, which is 0.1 eV different from the measurements.

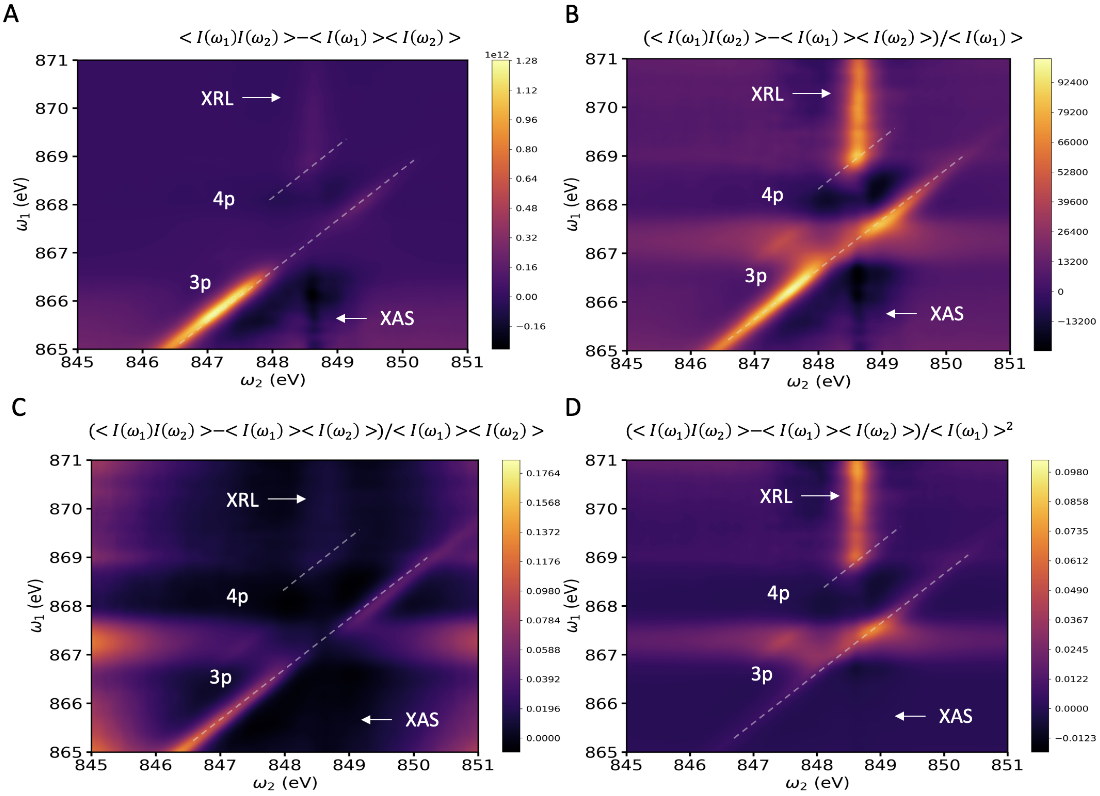

Figure 3.10: The covariance map with different normalizations combining two SASE runs centered at 867.5 and 870.0 eV. (A) The normal covariance function; (B) the covariance normalized to the average transmitted incident; (C) the covariance normalized to the average transmitted incident and the average emission; (D) the covariance doubly normalized to the average transmitted incident.

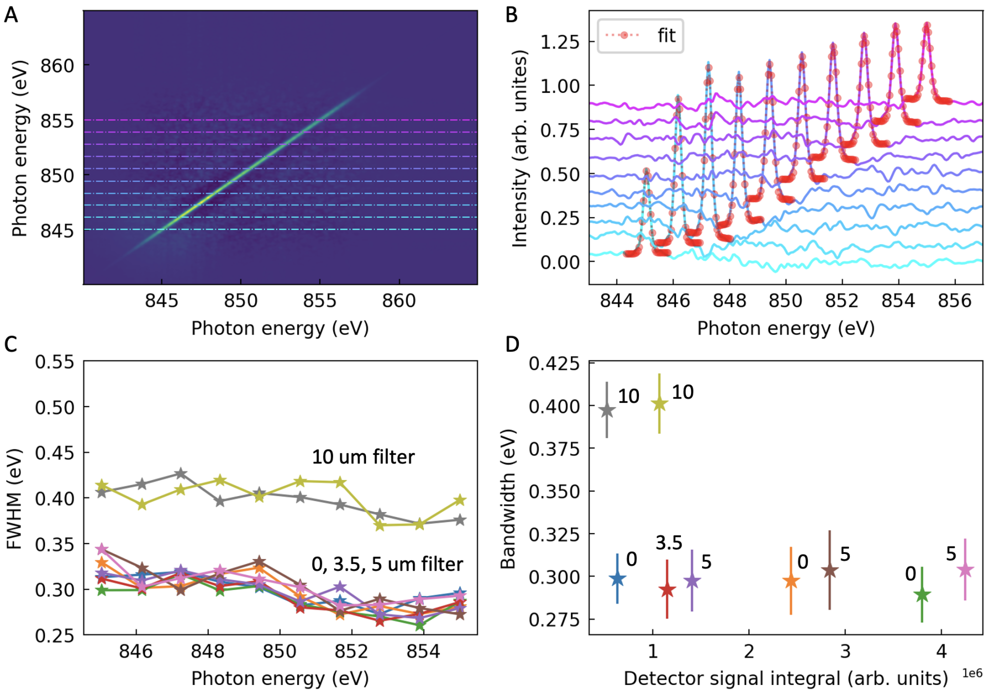

Figure 3.11: The bandwidth analysis of the SASE spikes with different filters and no neon gas in the cell. (A) the autocorrelation of the SASE spectra; (B) the Gaussian fit of the lineouts of the autocorrelation; (C) (D) the bandwidth of the autocorrelation function at different photon energies with different Al filters. It is clear that the bandwidth broadened from 0.3 eV to 0.4 eV when 10 μm filter is applied.

The deviation between the calculation and the experimental result can be explained by the extra broadening of the SASE pulse by the 10 µm Al filter. The influence of the different filters on the SASE pulse autocorrelation without interacting with gas is shown in Fig. 3.11. Gaussian fit is applied to the autocorrelation lineouts at different photon energies. Regardless of the incident pulse energy, the FWHM of the runs with 0, 3.5, and 5.0 µm Al filters give an FWHM ~ 0.3 eV, while the runs with 10 µm filters give 0.4 eV bandwidth. The extra ~ 0.1 eV broadening might be due to the nonlinear attenuation of the 10 µm filter that broadened the bandwidth of the SASE spikes.

Without the extra 0.1 eV broadening from the 10 µm filter, the FWHM of the correlation is 0.3 eV, which equals the one calculated above. The FWHM of the Raman line as a function of gas pressure (1.5, 2.0, 2.5, 4.0 bar) is shown in Fig. 3.12. With gas pressure increase, the bandwidth first drops from 0.375 eV to 0.3 eV, and then bounces back to 0.35 eV, and stays around 0.34 eV in the saturation regime. This narrowing of the bandwidth due to stimulated lasing is predicted in Weninger and Rohringer [2014]. Note that, the 0.3 eV bandwidth means that the Raman spectrum displays an energy resolution beyond the neon core-excited state lifetime broadening ($\Gamma \sim 0.27$ eV), which predicts the FWHM $\sqrt{\frac{1}{2\,\Gamma^2} + 2\,\sigma_s^2} \sim 0.35$ eV.

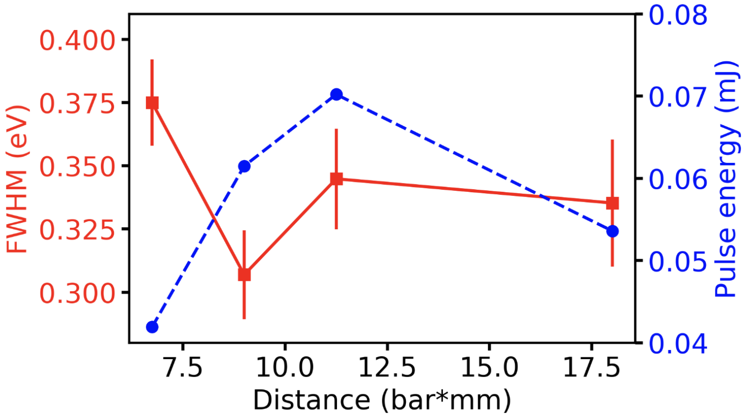

Figure 3.12: The bandwidth of the stimulated Raman signal evolves with the target thickness. The pressure of the gas is changed to obtain the results (1.5, 2.0, 2.5, 4.0 bar).

3.4 Supercomputer simulations

The TDSE-MWE code is used to simulate the SASE XFEL pulse resonant propagation through neon gas. The gas pressure is set to be 2 bar and the propagation length is 4.5 mm. There are 100 propagation steps applied in the calculation with a spacing of 0.045 mm. The code generates an output of the propagating spectrum every 5 steps. The SASE is generated by the stochastic pulse modeling code described in Section 2.3. The pulse duration is 40 fs (FWHM) and the bandwidth is 7.5 eV. The incident pulse is focused at the center of the gas cell with beam waist $\sim$ 2 µm. The peak intensity of the SASE spikes is $\sim 10^{18}$ W/cm^2.

In order to calculate the covariance map, the simulation of thousands of SASE shots is required. To cover the whole SASE pulse, the time window of the calculation is set to 100 fs. There are 30 grid points within each wave cycle ($\sim$ 0.00476 fs). Thus 100/0.00476$\sim$ 21000 grid points are used for the calculation of the field at each radial point. The transverse spatial window is set to be 10 µm, and 50 transverse grid points are used. There are 100 propagation steps in the 4.5 mm gas cell.

With such a large amount of grid points used, the propagation simulation for each SASE takes $\sim$ 72 core*hour. This makes the calculation for thousands of SASE shots impossible for a personal computer. The Open MPI is incorporated into our code to parallelize the independent TDSE calculations for different transverse points. Ideally, 50 threads are used to compute the TDSE at every radial point simultaneously. This shrinks the computing time to 6 hours. The Theta supercomputer at Argonne National Laboratory is used to perform the propagation calculation for 4096 SASE shots. In total, 4096 shots*32 threads*6 hour=786432 thread*hour is required for a full simulation at a specific condition. The output 3d fields are post-processed and analyzed by the local cluster (find details in the appendix).

Due to the limitation of the computational resources, the energy levels in the simulation are limited to the 9 levels. The parameters used are listed in Fig. 3.13. The energies of the core-excited states ($1s^{-1}$) are from Müller et al. [2017] , and the energies for the valence excited states ($2p^{-1}$) are from CCSD calculation performed by our cooperator Lan Cheng (Liu et al. [2018]). The transition dipole moments are calculated by CCSD, and then scaled with a factor of 1.5 to match the results in Suleiman [2023] and the XAS in Müller et al. [2017].

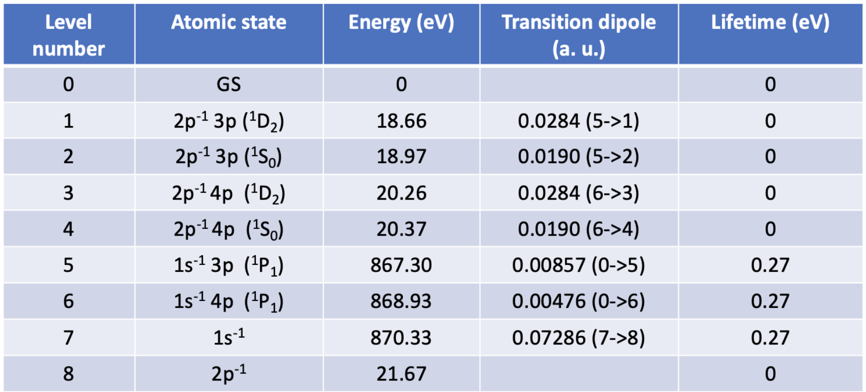

Level number	Atomic state	Energy (eV)	Transition dipole (a. u.)	Lifetime (eV)
0	GS	0		0
1	$2p^{-1}3p$ ($^1D_2$)	18.66	0.0284 (5->1)	0
2	$2p^{-1}3p$ ($^1S_0$)	18.97	0.0190 (5->2)	0
3	$2p^{-1}4p$ ($^1D_2$)	20.26	0.0284 (6->3)	0
4	$2p^{-1}4p$ ($^1S_0$)	20.37	0.0190 (6->4)	0
5	$1s^{-1}3p$ ($^1P_1$)	867.30	0.00857 (0->5)	0.27
6	$1s^{-1}4p$ ($^1P_1$)	868.93	0.00476 (0->6)	0.27
7	$1s^{-1}$	870.33	0.07286 (7->8)	0.27
8	$2p^{-1}$	21.67		0

Figure 3.13: The parameters used in the simulation. Only 7 energy levels in neutral and 2 levels in ion are included in our SASE simulations.

A typical full simulation result is shown in Fig. 3.14. The averaged incident SASE spectrum is close to a Gaussian with 7.5 eV bandwidth. The averaged output spectrum has 3p and 4p resonant absorption dips and the stimulated Raman and XRL emission. The small narrow spike around 848.6 eV is XRL emission, while the broad peak is the stimulated Raman signal, which has a dip at 850 eV and resembles the transmitted incident.

The combined normalized covariance of two full simulations with photon energy centered at 867.5 eV and 870 eV is shown in Fig. 3.15. The simulation results resemble the experimental results closely. The normalized covariance of the transmitted incident and the Raman shows the 3p and 4p Raman dispersive lines and the XRL above the ionization threshold. In the simulation, we have the incident SASE spectrum recorded, thus the normalized covariance of the incident and the Raman can be calculated. This covariance removes the artificial backgrounds due to the resonant absorption, thus giving much cleaner Raman signals. As a result, the Raman emission to the two multiplet $2p^{-1}3p$ states $^1D_2$ and $^1S_0$ are identified.

The traditional spontaneous RIXS map has signal intensity proportional to the square

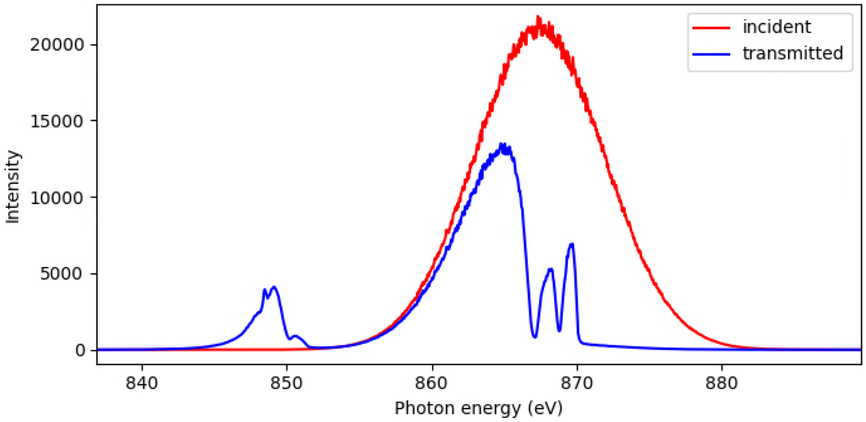

Figure 3.14: The averaged incident and transmitted spectrum of SASE simulation with 4096 shots. The 40 fs SASE pulse has peak intensity $\sim 2.5 \times 10^{18}$ W/cm^2. The gas pressure is 2 bar and the propagation distance is 4.5 mm.

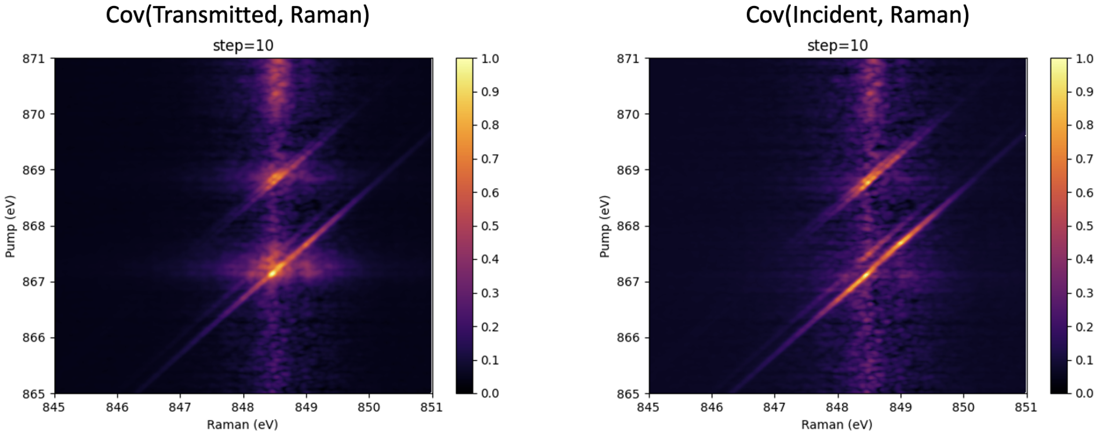

Figure 3.15: The normalized covariance map obtained by combining the simulations with canter photon energy at 867.5 and 870 ev.

of the transition dipole moments. The spontaneous RIXS map calculated by Eq. (3.3) is shown in Fig. 3.16. The incident Gaussian pulse has 0.2 eV bandwidth. The core excited to 3p, 4p, 5p and 6p states are included and all the spontaneous Raman transition channel with different polarization is also included. Overall the spontaneous Raman looks close to the normalized covariance obtained with SASE pulses with 1 bar pressure.

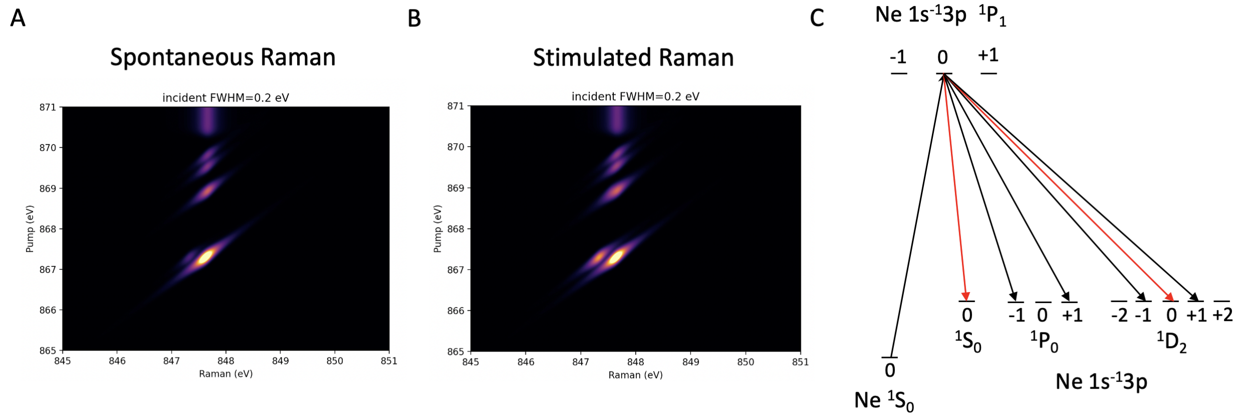

Figure 3.16: The spontaneous and stimulated Raman RIXS map calculated by Kramers–Heisenberg formula. The stimulated Raman is different from the spontaneous Raman. The polarization of the Raman down transition is the same as the incident, thus the Raman channels can be selectively probed by changing the incident pulse polarization.

This similarity motivated us to explore the physical meaning of the signal intensity in the normalized stimulated Raman covariance. Specifically, will the exponential amplification due to stimulated emission preserve the linearly proportional relationship between the square of dipole transition and the signal intensity? The averaged Raman signal plotted against the energy loss is shown in Fig. 3.17. The different lines represent the Raman signal as a function of the propagation distance. There are 11 outputs through the 4.5 mm gas cell. The Raman signal of the 3p grows as the pulse propagates and is saturated at step 4 ($\sim$ 1.80 mm). The 4p Raman signal is much smaller than the 3p, due to the smaller $1s \rightarrow 4p$ transition dipole moment. With slower growth, the 4p Raman saturated at step 5 ($\sim$ 2.25 mm). The ratio of the 4p to 3p integral Raman signal is shown in the right panel. The ratio saturated at around 0.025 after step 8 ($\sim$ 3.60 mm).

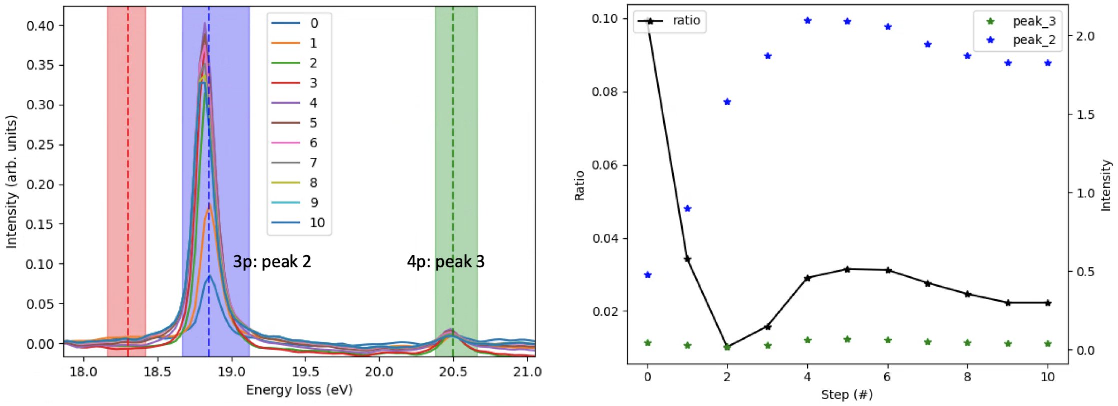

Figure 3.17: Left: The Raman spectrum as a function of propagation distance. The gas pressure is 2 bar for the simulation and the total propagation distance is 4.5 mm with 11 outputs. Right: The integral of 3p and 4p Raman peak and their ratio as a function of propagation distance in the number of output steps.

The same simulation is carried out with the ratio of $1s \rightarrow 4p/1s \rightarrow 3p$ transition dipole moments equalling 0.57, 1.0, and 1.3. The ratio of the Raman signal intensities of 4p and 3p at saturation from the normalized covariance as a function of the transition dipole moment ratio square is plotted in Fig. 3.18. At the saturation regime, the Raman signal intensity is still linearly proportional to the square of the transition dipole, which could be very helpful for directly connecting the Raman signal to the atomic transition properties. It is interesting that even after the exponential growth, the nice relation is still preserved. This could be explained by the competition between spontaneous and stimulated Raman emission. For a fixed amount of atoms being populated to the core-excited state, the stimulated Raman dominates over the spontaneous Raman in the saturation regime. The original spontaneous Raman decay is replaced by the stimulated Raman emission in the forward direction. In other words, the stimulated Raman is an analogy to a magical focusing mirror that constrains all the spontaneous Raman from all directions to the forward. Thus the saturated Raman signal preserved the relation held by the spontaneous Raman.

Another advantage of the stimulated Raman is the polarization sensitivity. As shown in Fig. 3.16, after the incident pumps the atom to a core-excited state, the spontaneous Raman

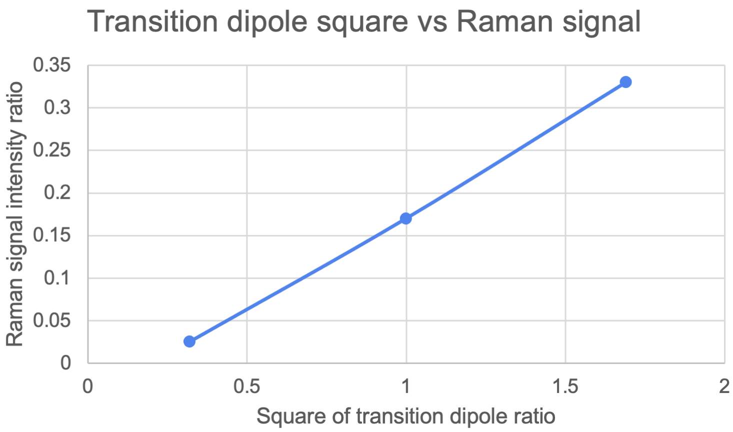

Figure 3.18: The Raman signal intensity is linearly proportional to the square of the transition dipole.

emits from all the relaxation channels, since there is no limitation on the polarization of the spontaneous Raman photon. However, in the case of a single SASE pulse impulsively stimulating Raman scattering, the emission occurs only through the channels that generate the photon with the polarization the same as the incident. For example, the only valence excited states populated through stimulated Raman are Ne $1s^{-1}3p\,(^1S_0)$ and $(^1D_2)$ with the magnetic quantum number $m = 0$. The ratio between spontaneous and stimulated scattering cross-section at the beginning of the propagation can be adjusted by changing the central photon energy of the incident SASE. Here, in stimulated x-ray Raman experiments, the polarization of the two photons (usually called pump and dump) can be adjusted to select the valence-excited states to probe.

CHAPTER 4

NON-INVASIVE SPECTRAL CHARACTERIZATION OF SASE PULSES

Ghost-imaging (GI) uses the correlation between low-resolution signals from the object beam, which interacts with the sample, and high-resolution signals from the reference beam, which doesn't interact with the sample, to make a high-resolution "image" of the sample. GI-based methods have been demonstrated in spatial, temporal, and spectral domains. Here, the GI method is applied to extract the response matrix of the photoelectron spectrometer (PES) array from the correlation between spectra measured by PES and by grating spectrometer. The response matrix obtained can be applied to the PES signals of the yet-to-be-characterized SASE shots to reconstruct a photon spectrum with better resolution.

A demonstration experiment was carried out at European XFEL, where spectra of thousands of SASE shots are simultaneously characterized by the PES array and the grating spectrometer. The GI reconstructed spectrum shows a better match with the grating spectrum. The influence of the number of shots included, the number of eToF signals, and gas densities on GI reconstruction are investigated.

4.1 Principle of ghost-imaging (GI) method

GI is an imaging technique that works without "interaction" with the object. Instead of measuring the light directly scattered from the sample, the statistical properties of stochastic incident pulses are used to extract the information from the sample. As shown in Fig. 4.1, in GI, an object is imaged using correlations between the intensities of two light beams: an "object beam" that interacts with the object and reaches a single pixel ("bucket") detector, and a "reference beam" that does not hit the object and arrive at a multi-pixel detector.

The first GI experiment was the observation of unusual interference fringes in the coin-

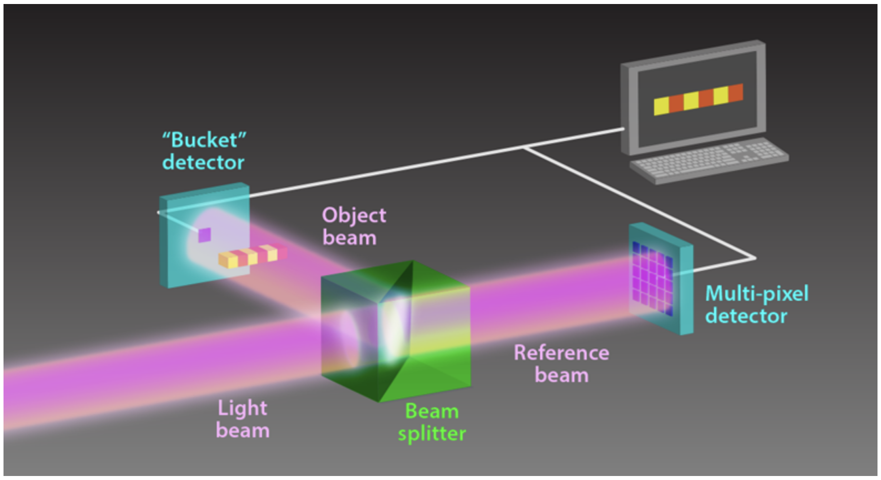

Figure 4.1: The schematic of the ghost-imaging experimental setup. The incident stochastic beam is split into two replicas: one object beam passes through the target and is measured by the low-resolution "bucket" detector, and the other reference beam is measured by the high-resolution multi-pixel detector as a characterization of the incident beam. Many measurements from the different incident beams are recorded and the correlation between the objective and reference signals is calculated to obtain the image of the sample. Figure from Saldin [2016].

cidence counts of photon pairs (Strekalov et al. [1995]). The theoretical paper explains the photon coincidence imaging which emphasizes the essential role of two-photon entanglement was published by Abouraddy et al. [2001]. However, the experimental demonstration of the GI with thermal light dissolved the requirement of the entangled photon source (Bennink et al. [2002]). The first GI in the x-ray regime was realized with synchrotron radiation (Yu et al. [2016], Pelliccia et al. [2016]). It is worth mentioning that the idea of using intensity correlation to obtain information using stochastic light dates back to 70 years ago when the Hanbury Brown and Twiss effect was used to measure the size of the planet (Brown and Twiss [1956]).

The GI method exploits the relation between the objective measurement and the reference measurements to extract the desired information. A typical GI algorithm describes the bucket detector signal b as a linear combination of the reference signal A with coefficients proportional to the unknown object property x:

$$b = A * x \tag{4.1}$$

where b is a $n \times 1$ row vector with each element representing a bucket detector reading from one shot; A is a $n \times m$ matrix constructed by n measurements with m signals from the pixellated detector; x is a $m \times 1$ row vector with the unknown variables to be solved. This formula includes all the information collected by n realizations of the detection. For example, the total light transmitted through the object is the sum of the object beam times the transmission of the sample. For a half-half beam splitter, the object beam can be replaced by the reference beam measured by the multi-pixel detector. Thus we have the typical GI formula: total light transmitted (b) = reference light (A) * object transmission (x). The incident beam fluctuates randomly, thus the row vectors of the matrix A are assumed to be linearly independent of each other. According to linear algebra, this means that there should be a unique solution of x to fulfill the equation. In the real calculation, solution x is found by minimizing the difference $|b - A * x|^2$ by least square fitting.

GI has several advantages over transitional imaging. Conventional imaging methods capture an image of an object by recording the intensity and color of light scattered from the object. In GI, the object only experiences a small part of the incident light from the beam splitter. Since the “bucket” detector is applied to collect the total scattered light, the object does not have to receive a high dose of radiation. This is very helpful in medical imaging, where the dose should be limited. The GI is also very robust against the fluctuations in the image pathway. For example, it is widely explored and applied in mapping for satellite imaging, where the random scattering from atmospheric turbulence and clouds is averaged out and only the intensity correlations between the object beam and the reference beam are retained (Saldin [2016]). The application of the GI had been expanded from the spacial imaging to the measurements in the spectral and temporal domains. The SASE XFELs, with spectral and temporal spikes that randomly fluctuate from shot to shot, are suitable for GI.

In the spectral domain, GI can be used to improve the energy resolution of the attosecond transient absorption spectrum. For example, as a demonstration, GI is applied in measuring the $1s \rightarrow 2p^*$ resonance absorption of the oxygen atom in NO (Driver et al. [2020], Li et al. [2021b]). The incident attosecond XLEAP pulses interact with the NO molecule and the electron spectrum is recorded by the co-axis velocity map imaging (c-VMI) detector. The NO molecular plays the rule of the beam splitter: the 1s photoline of the N atom is used to characterize the incident XLEAP pulse spectrum (reference measurement); the resonant Auger signal of O is integrated to represent the absorption of the O atom (object measurement). The GI algorithm is used to get an oxygen XAS spectrum with sub-XLEAP bandwidth resolution.

In the temporal domain, GI is proposed to track the ultrafast molecular dynamics with improved temporal resolution (Ratner et al. [2019]). The traditional way of pump-probe experiments requires ultrashort pulses as well as precise control of the delay between pulses. The SASE pulse has ultrashort temporal spikes, the interaction between SASE pulse and the sample resembles many pump-probe experiments with random delays. The GI algorithm is proposed to extract information on the dynamics. It is predicted that the new method will enable the reconstruction of ultrafast dynamics down to the coherence length of the SASE pulse.

4.2 Non-invasive characterization of the SASE spectrum by GI

The core-level x-ray transient absorption spectroscopy (XTAS) with ultrafast XFEL pulses has become a workhorse in following photoinduced electronic and nuclear dynamics on their intrinsic femtosecond timescales via pump/probe techniques. The XTAS projects core electronic states onto unoccupied valence/Rydberg states, thereby capturing the evolution of valence electronic motion following an excitation pulse. However, with the broad bandwidth of ultrashort XFEL pulses, the realization of XTAS with stochastic SASE pulses is challenging.

In traditional methods, the absorption spectrum is obtained by measuring the light intensity transmitted while scanning the incident photon energy. The resolution of the absorption spectrum is determined by the bandwidth of the incident beam. The broad bandwidth of the attosecond pulse leads to poor energy resolution using this traditional XAS method. Also, the monochromator applied stretches the pulse in the temporal domain which compromised the pump-probe time resolution.

An alternative approach to realizing the attosecond transient absorption spectrum (ATAS) is by measuring the difference between transmitted and incident spectra. With this approach, one may obtain the XAS across the entire SASE bandwidth without compromising the temporal resolution. Taking advantage of the stochastic nature of the SASE XFEL pulses, the correlation between incident and transmitted spectra can be exploited to obtain the XAS spectrum with high energy resolution. Without the energy loss due to the monochromator, the new method is suitable for exploring the ultrafast nonlinear x-ray matter interactions.

The new approach of ATAS requires the characterization of the incident SASE spectrum. Several diagnostic tools have demonstrated well-resolved spectral measurements on a single-shot basis without compromising the quality of the x-ray beam. The common element required in these methods is a x-ray beamsplitter, which takes a sample of the incident x-ray to measure the spectrum. Crystal Bragg diffraction (Zhu et al. [2012]) and gratings (Engel et al. [2020]) are used as a beamsplitter in hard x-ray and soft x-ray regimes, respectively.

An alternative way is to use the photoelectrons from the dilute gas. The incident photon energy is retrieved by measuring the kinetic energy of the ejected photoelectrons. The dilute gas is the natural beamsplitter, so no additional elements are needed. Meanwhile, no 2D photon detector is required, the photoelectron spectrum is one dimension and is compatible with the high repetition rate XFELs. The electron time-of-flight spectrometers (eTOFs) are widely applied to measure the photoelectron spectrum. The photoelectron spectrometer array (PES array) has enabled the measurement of the position, polarization, and central energy of an x-ray photon beam as demonstrated at the PETRA-P04 beamline (Viefhaus et al. [2013]). Although the PES array has been employed to monitor the incident center photon energy (Laksman et al. [2019], Serkez et al. [2020]), the characterization of the incident photon spectrum, especially the single shot spectrum, is very challenging.

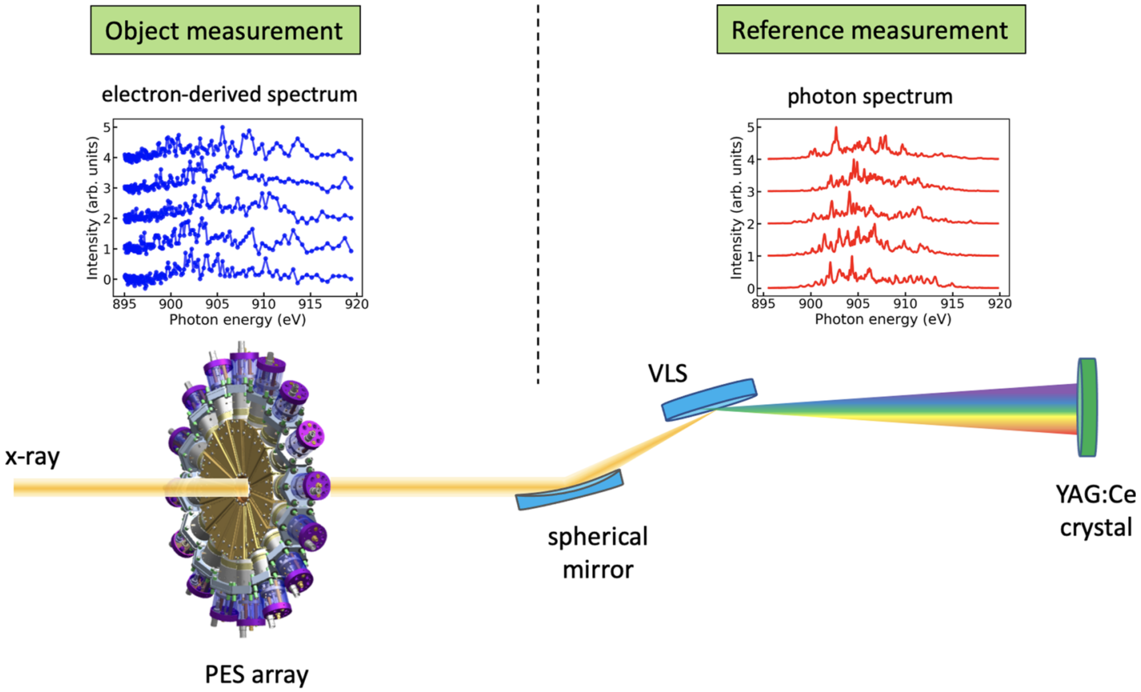

Figure 4.2: The schematic of the experimental setup to demonstrate the GI-enhanced PES spectrum method. The incident SASE XFEL passes through the PES array, where the dilute neon gas is ionized and the photoelectron time-of-flight is measured. For these measurements, one obtains the electron-derived spectrum as the object measurements in GI. The transmitted x-ray is focused on a VLS grating and the dispersed beam hits the YAG:Ce crystal screen and the image is recorded by CCD. The photon spectrum from the grating spectrometer plays the role of reference measurement in GI. Figure from Li et al. [2022].

The ghost-imaging algorithm can be used to improve the energy resolution of the raw PES array measurements (Li et al. [2022]). The photoelectron spectra and photon spectra of thousands of SASE shots are measured simultaneously by a PES array and a grating spectrometer. GI is used to calculate the response matrix of PES array by correlating the signals from the two detectors. The response matrix is then applied to reconstruct the photon spectrum of the yet-to-be-measured SASE pulses with high resolution from the PES signal.

The experiment to demonstrate this method was performed at the European XFEL SQS branch of the SASE3 beamline. The experimental setup is shown in Fig. 4.2. The incident SASE soft x-rays were centered at 910 eV with an averaged FWHM bandwidth $\sim$ 9 eV. The standard deviation of pulse energy fluctuation is 3% for an average pulse energy of 3.8 mJ as measured with an x-ray gas monitor detector (XGM). Taking into account the CCD image recording speed, the SASE shot was coming at a 10 Hz repetition rate.

The SASE XFEL pulses from the undulator penetrate through the dilute neon gas in the PES array, where the photoelectron spectrum is measured. The PES array is located far from any x-ray focus points and the SASE beam spot size was estimated to be $\sim$ 5 mm in diameter, which ensures the photoionization remains within the linear regime. The amount of photoelectrons generated is controlled by the pressure of the gas jet. The background pressure in the interaction chamber is 1×10^8 mbar and the pressure of the gas injected was adjustable from 1×10^7 mbar to 1×10^5 mbar. The gas density was set to be 2.5×10^7 to obtain enough photoelectrons as well as avoid space charge effects. Note that this dilute gas is almost transparent to the XFEL pulses, and should have almost no influence on the temporal and spectrum intensity of the incident pulse. Thus it is naturally a beamsplitter for soft x-rays.

The electron time-of-flight (eToF) of the photoelectrons ejected from the core-shell of neon is recorded by a microchannel plate (MCP) stack. The retardation voltage of the eToF is chosen to be 30 eV, which reduces the photoelectron kinetic energy of 1s neon from an initial 40 eV to 10 eV. The distance between the interaction point and the MCP detector is 13.5 cm and the average time for the retarded electron to fly through the eToF tube is 60 ns. Note that there are 16 eToF installed on the plane perpendicular to the incident x-ray beam.

A typical measurement of the single-shot and averaged eToF signal is plotted in Fig 4.3. The photoionization of different atomic sub-shell electrons and Auger decay lead to different peaks as denoted in the figure. With 2.4×10^{7} mbar gas density and 0.3 Mbarn Ne 1s photoionization cross section at 910 eV, an incident x-ray pulse with an average of 2.6×10^{13} photons would generate around 144,000 photoelectrons. Given the geometry of the PES array (Laksman et al. [2019]), around 300 Ne 1s photoelectrons are detected by each eToF along the polarization direction. The eToF of the 1s photoelectron peak ranges from 40 ns to 100 ns. The MCP registers the signal every 0.5 ns, thus around 120 data points are taken in the 1s photoelectron peak. The eToF signal fluctuates shot-to-shot due to the fluctuation of the incident SASE spectrum. The standard deviation of the eToF signal at each point is represented by $\sigma_y(\omega)$. The average value between 100 and 120 ns is taken as a background, which is subtracted in a shot-to-shot manner. Since the photoelectron yield is proportional to the gas density, we normalized the PES signal to the gas density.

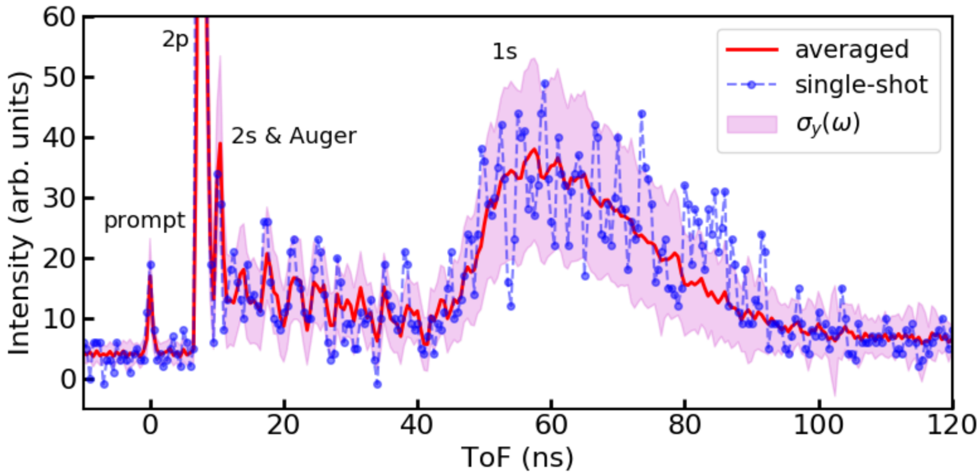

Figure 4.3: The single-shot and averaged eToF signal. The photoelectron peaks corresponding to the ionization of electrons from different atomic energy shells are denoted. Figure from Li et al. [2022].

The photon spectrum of the SASE pulse is characterized by a grating spectrometer.

The x-rays passing through the PES array is focused by a spherical mirror to a variable-line spacing (VLS) grating. The light is dispersed on a YAG:Ce crystal and the induced fluorescence is recorded by a charge-coupled device (CCD). The number of photons that arrive at the YAG:Ce crystal is adjusted by the gas attenuator before the spherical mirror to ensure the linear response of the crystal. The average pulse energy of the incident FEL beam is 3.8 mJ. The Kr gas attenuator has a transmission of 35.5%. With 36% reflecting efficiency of the grating, 0.49 mJ x-ray hits the screen. The 120 mm grating has a groove density of 150 lines/mm. The incidence angle of the beam is 12.3 mrad, and the imaging screen is located 99 m downstream. The spectral range recorded on the YAG screen is from 895.5 to 919.8 eV which spreads over 1900 pixels. The estimated resolving power for the spectrometer, based on independent measurements, is $E/\Delta E = 10,000$. This allows resolving the single spikes of the SASE pulses, which have a minimum spacing of $\sigma = 90$ meV, as shown in Fig. 4.4.

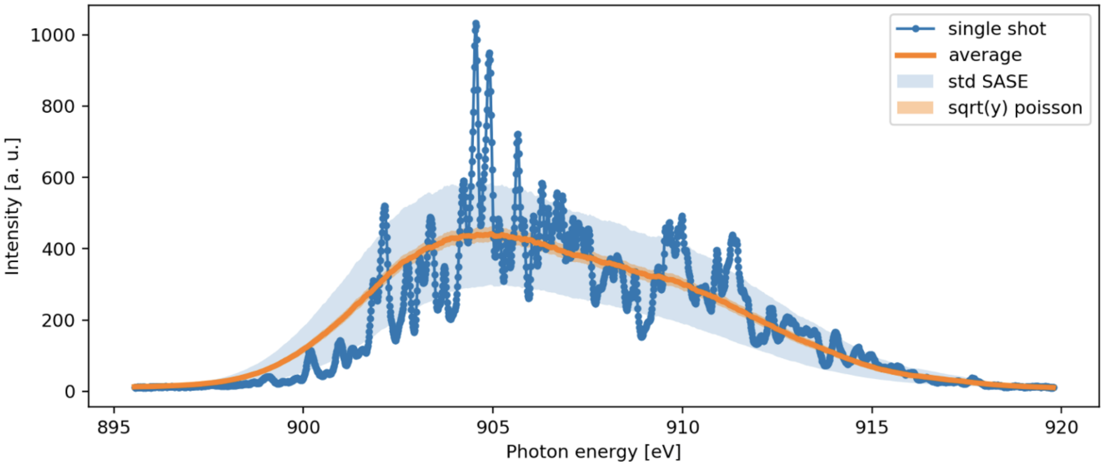

Figure 4.4: The SASE single-shot and averaged photon spectrum measured by the grating spectrometer.

The correlation between the measurements from PES array and the grating spectrometer is used in the GI algorithm to improve the SASE spectrum characterization by the PES array. As shown in the inserted figures in Fig. 4.2, the single shot PES signal plays the role of object measurement, while the spectrometer spectra are the reference measurements.

Since the same SASE pulse is measured, the photoelectron signal c (after normalization to the gas density) is proportional to the incident photon spectrum s as measured by the spectrometer:

$$c = A\,s \tag{4.2}$$

where A is the PES array response matrix with dimension $m \times n$, where m is the eToF points and n is the spectrograph pixels. This equation resembles the basic formula in GI which is usually used to obtain the sample information by solving for A. However, here we want to predict the high-resolution incident SASE spectrum s based on the PES array signals c. We formally write the equation (4.2) as:

$$s = R\,c \tag{4.3}$$

where the matrix R is a formal reverse of Matrix A. R is a mapping between low-resolution PES array spectra to high-resolution grating spectra. In other words, R is a calibration matrix of PES array from the eToF signal to the incident photon spectrum. It contains the information that characterizes the response of eToF to the incident x-ray photon.

To solve Eq. (4.3), we take into account all the N independent measurements obtained. Each shot with measured value s_i and c_j provides a realization of:

$$s_i = \sum_{j=1}^{m} R_{ij}\,c_j \tag{4.4}$$

the N measurements are assumed to be independent of each other and form N independent linear equations since SASE spectrum fluctuates randomly. With a fixed index i, there are m unknown variables R_{ij}. With enough single-shot measurements, one can achieve $N > m$, and the N independent equations have a set of unique solutions R_{ij}.

In the experiment, the data was taken for 30 mins with 10 Hz SASE XFEL, $\sim$ 15,337 single-shot spectra were measured. These measurements form 15,337 equations. To cover the whole SASE with center photon energy at 910 eV, the spectrometer measurements are selected within 895 and 920 eV, which contains $n = 1900$ data points. With a linearly polarized x-ray, the photoelectron distribution follows $\cos^2(\theta)$, with the maximum intensity along the polarization direction. To optimize the signal from the PES array as well as avoid contamination from the noisy signals, the spectra from 6 eToFs along the polarization direction are used. Each eToF signal is selected within the range [40, 100] ns. Thus the PES array measurement vector c has dimension $m = 6 \times 137 = 822$. In summary, as shown in Eq. (4.4), for each fixed index i of s, there are $N = 15,337$ equations to solve $m = 822$ unknown variables R_{ij}.

Instead of directly solving these equations, the response matrix elements R_{ij} are determined by least square regression, i.e. by minimizing the quantity $|s - Rc|^2$. The *scipy.optimize* module in Python is used for finding the least square solution. The result of the PES array response matrix is shown in Fig. 4.5. As expected, there are six parabolic lines that stand out on the map corresponding to the calibrations of the six eToFs, whose signals are included. The values of the response matrix for the eToFs are different, which indicates the different contributions from them to the reconstructed high-resolution SASE spectrum. Note that, the response matrix gives the lines that resemble the traditional calibration function between the eToF τ and the photon energy E_{ph}:

$$E_{ph} - E_{bind} \propto \frac{1}{2} m_e \left(\frac{L}{\tau} \right)^2 \tag{4.5}$$

where E_{bind} is the binding energy of the photoelectron; m_e is the mass of the electron, and L is the length of the eToF tube. However, the response matrix is a 2D mapping, which contains more information. For example, the width of the parabolic lines relates to the energy resolution of the PES. There are negative elements in the matrix, which means there are signals from eToF that contribute negatively to the spectral reconstruction. The response matrix essentially takes into account the broadening of the spectrum and deducts the "bad" signals of PES, which eventually reproduce a better spectrum.

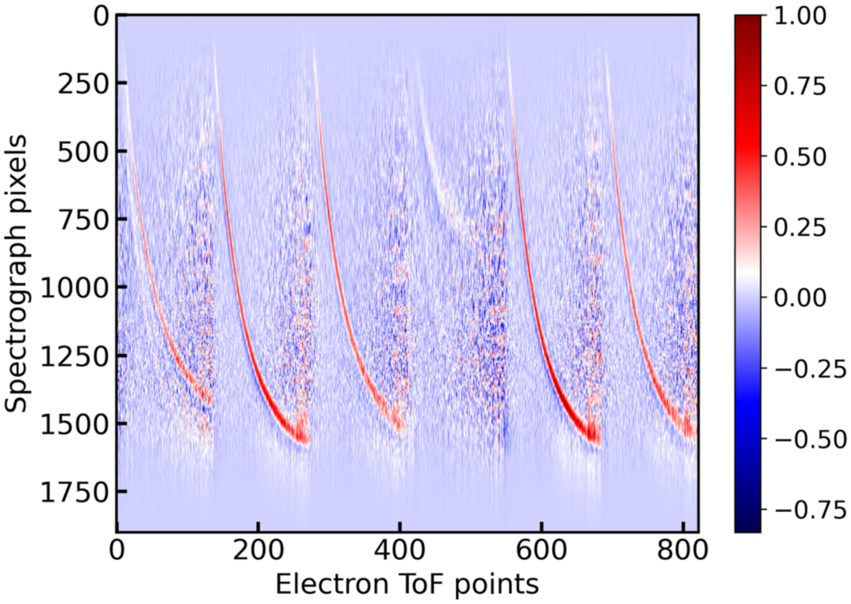

Figure 4.5: The response matrix of PES array calculated from Eq. (4.4). The six parabolic lines represent the calibration line of the six eToF, whose signals are included in the calculation. Figure from Li et al. [2022].

It is reasonable to assume the response matrix of the PES array does not change for given photon energy, gas target, photoelectron energy range, and PES array configuration (fixed retardation, bias voltage...); thus the calculated R can be used to predict the spectra of yet-to-be-measured shots. The high-resolution reconstructed x-ray spectrum is obtained by multiplying the PES measurement with the matrix R.

The original single-shot PES spectrum and the photon spectrum are shown in Fig. 4.6 a. The electron-derived spectrum is from the eToF measurement with the traditional calibration function Eq. (4.5). The photon spectrum is measured by the grating spectrometer. The two spectra both have random spikes, yet they do not match with each other. Specifically, the electron-derived spectrum has less resolution than the photon spectrum. The bottom panel shows the GI reconstructed spectrum and the photon spectrum convolved with a $\sigma = 0.2$ eV Gaussian function $e^{-x^2/2\sigma^2}$. The spikes of these two spectra match with each other. Thus the GI reconstructed spectrum is a better measurement of the incident SASE spectrum and GI reconstruction is used to enhance the performance of the PES array. Note that the

0.2 eV is chosen based on the resolution difference between PES and the spectrometer. The spectrometer records 1900 spectrograph pixels, while the PES only registers 137 eToF points, the resolution differs $1900\,\text{pixel}/137 * 0.013$ eV/pixel ≈ 0.2 eV. Where 0.013 eV/pixel is the resolution of the spectrometer.

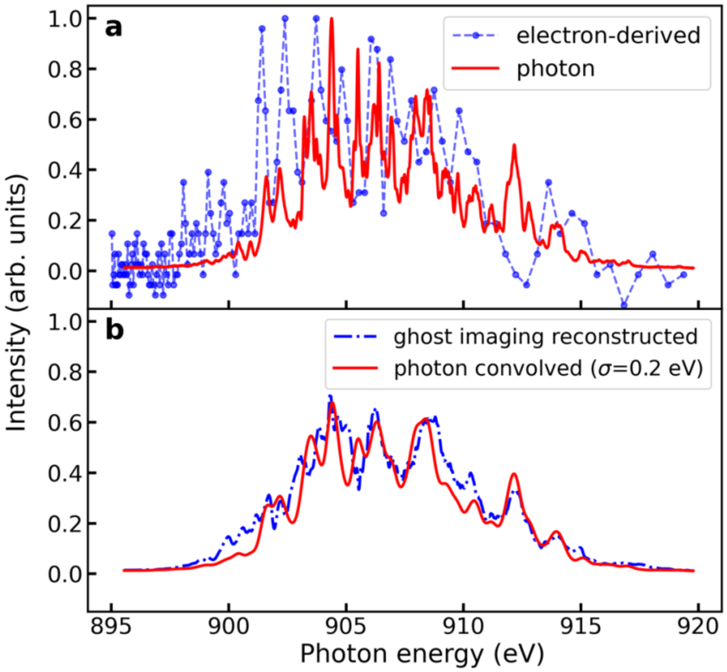

Figure 4.6: The single-shot spectrum from PES and spectrometer (a). The GI reconstructed spectrum and the Gaussian convolved grating spectrum (b). Figure from Li et al. [2022].

As mentioned above, one function of the reconstruction is to remove the instrumental broadening. Thus a higher resolution reconstructed spectrum, which matches well with the convolved grating spectrometer measurement is obtained. To quantify the performance of the reconstruction, we calculate the standard deviation of the difference $\Delta\sigma_{\mathrm{e-p}}$ between the electron-derived spectrum and the photon spectrum before and after GI reconstruction:

$$\Delta\sigma_{\mathrm{e-p}} = \sqrt{\frac{\sum_{i=1}^{n} |(c_i - \bar{c}_i) - (s_i - \bar{s}_i)|^2}{n}} \tag{4.6}$$

where $\bar{s}$ and $\bar{c}$ are the mean value of spectrometer and PES array measurement, respectively,

n is the number of spectrometer pixels. Basically, the electron-derived spectrum and photon spectrum differ at each photon energy, this formula computes the standard deviation of these differences across the spectrum. The result is only sensitive to the deviation of the spikes since the averaged spectrum is subtracted to remove the contributions of the overall deviation. This avoids the contributions from any backgrounds or mismatch of the central photon energy of the two spectra compared.

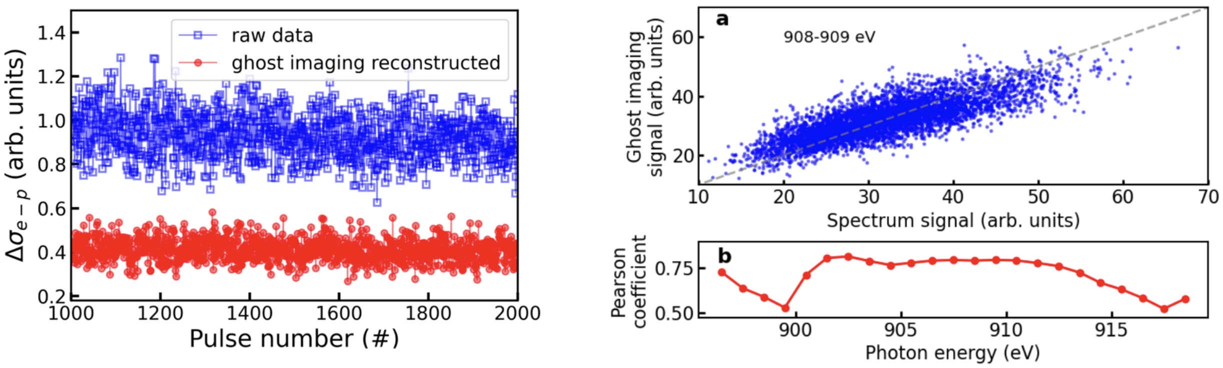

Figure 4.7: The standard deviation of the difference between PES/GI reconstructed spectrum and the grating spectrum. There is an average of more than half a decrease in the deviation for the GI reconstructed spectrum. The GI reconstructed spectra also show a good correlation with the photon spectrum. Figure from Li et al. [2022].

The standard deviation of the difference between the raw data and the GI reconstructed $\Delta\sigma_{e-p}$ is shown in Fig. 4.7. Each point represents the deviation for a single-shot measurement calculated according to Eq. (4.6). Overall, the GI reconstruction gives a much better PES spectrum that matches with the SASE spectrum characterized by the spectrometer. The deviation reduced from 1.0 for the raw PES data to 0.4 for the GI reconstructed spectra. The enhancement of PES performance can also be confirmed by the good linear correlation, with a Pearson coefficient of up to 0.75, between the GI spectrum and the grating spectrum.

One essential property of the GI reconstruction method is the capability of predicting a high-resolution spectrum from the PES measurement. The GI algorithm gains the predictive

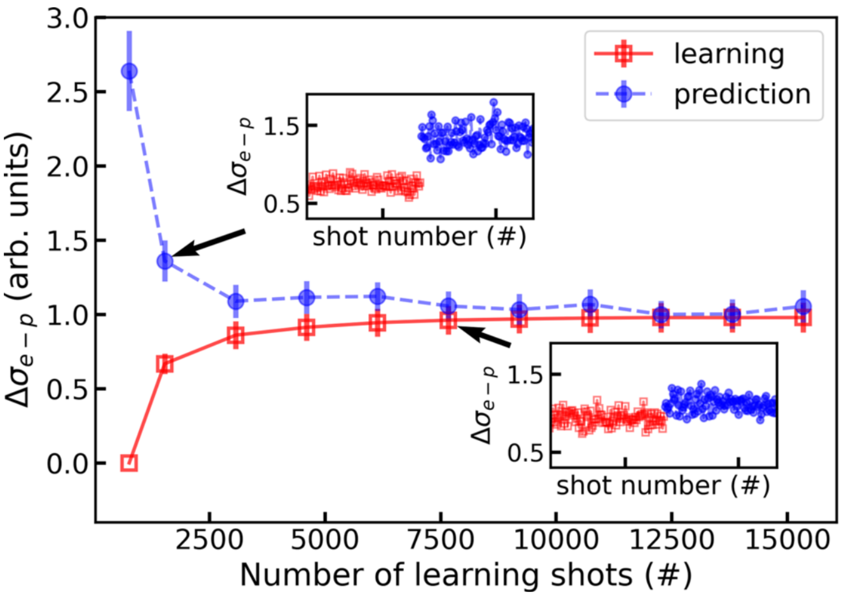

Figure 4.8: The deviation $\Delta\sigma_{e-p}$ of the learning shots and the predicted shots as a function of number of shots included in the GI algorithm. The results converge at around 8,000 shots when the deviation of leaning and prediction matches each other. The number of shots required to achieve convergence is roughly 10 times the number of unknown variables $m = 822$. Figure from Li et al. [2022].

capability by "learning" from the numerous shots measured. As mentioned above, the least-square fit is used to solve the response matrix of the PES. In general, the more shots included in the least-square regression, the better performance of the fit. Thus the number of shots needed to converge the fitting is important.

The deviation of the difference between the reconstructed spectrum and the photon spectrum is calculated for GI reconstruction with different numbers of learning shots used. In order to quantify the predictive capability, we left 100 shots out of the learning process, and they are used to show the performance of the prediction. As shown in Fig. 4.8, the deviation of the learning shots is very small when only a small amount of shots are used for learning. This over-fitting happens when the number of shots is smaller or close to the number of fitting parameters, i.e. the number of unknown variables $m = 822$. The predictive power is very poor in the over-fitting regime. As more and more shots are included in the learning process, the regression performs better, since the fitting captures more and more important information of the PES. The learning process was saturated with around 8000 shots used, where the deviation of the predicted shots met with the deviation of the learning shots.

There are several ways to increase the performance of the GI reconstruction method. In general, the GI method is based on the PES measurement and according to the linear relation in Eq. (4.3), the signal-to-noise ratio of the PES measurements c would directly pass to the reconstructed spectrum s. Thus more precise measurements from the PES would increase the performance of the reconstruction. Meanwhile, a better PES signal means more useful information is included in the learning of response matrix. According to Eq. (4.3), the reconstructed spectrum would be better with a better response matrix R.

The influence of the number of eToF signals included in the GI reconstruction is shown in Fig. 4.9. The upper panel represents the reconstructed spectrum with one eToF signal. The lower panel displays the reconstructed spectrum with six eToF signals. A random single-shot is used to compare the reconstructions with the convolved photon spectrum. Apparently, the GI reconstruction with six eToF gives a spectrum that matches better with the photon spectrum. The standard deviation of the difference $\Delta\sigma_{e-p}$ as a function of the number of eToF used is plotted in the inserted figure. The relative deviation drops continuously from a value of 1.0 to 0.87 as the number of eToF increases from one to six. This result makes sense because the more eToF used, the more information of the incident SASE pulse is recorded, thus a better measurement from the PES. In addition, more eToF signal means larger vector c, and more unknown variables to be solved. With more degrees of freedom, a better fitting is obtained that can offer better performance for the reconstruction.

The effects of the PES array chamber gas pressure on the GI reconstruction are shown in Fig. 4.10. The deviation of the reconstructed spectrum from the convolved photon spectrum decreases as the pressure increases. The reconstructed single shot and the convolved photon

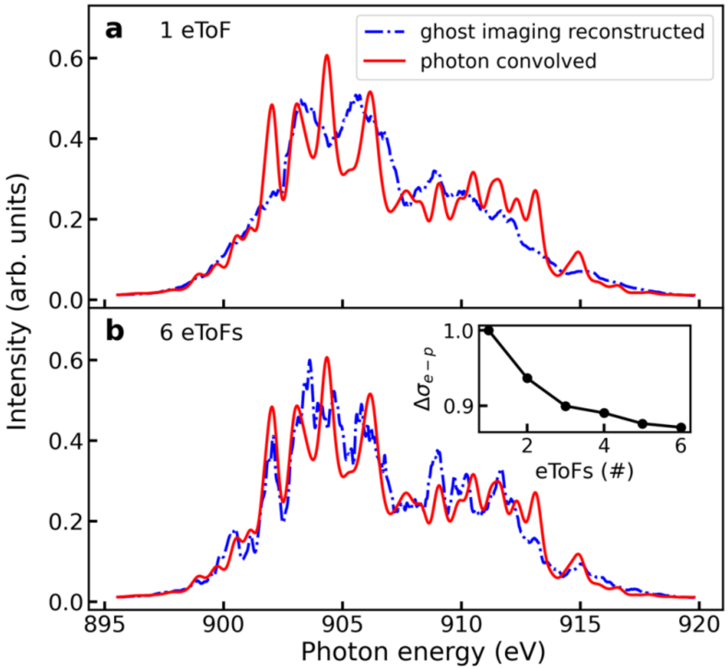

Figure 4.9: The reconstructed spectrum with one eToF signal (a) and six eToF signals (b). The inserted plot shows the deviation decreases as more eToF signals are included. Figure from Li et al. [2022].

spectrum with gas density equals 1.7×10^{-7} mbar and 3.2×10^{-7} mbar are shown in the subpanel b and c, respectively. This result is not surprising, since the more gas in the interaction, the more photoelectrons are generated, thus a better signal-to-noise ratio of the PES measurements and a better GI reconstructed spectrum.

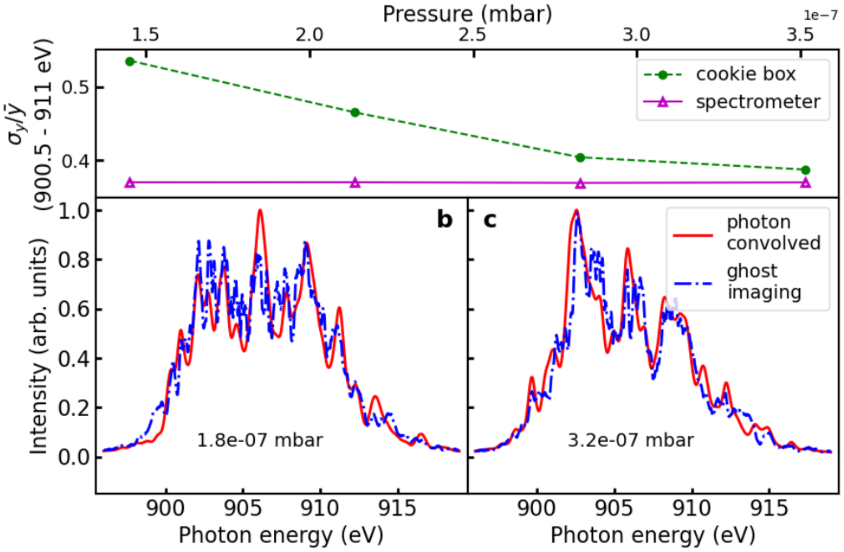

Figure 4.10: The influence of the gas pressure on the GI reconstruction performance. The higher the gas density in the PES array, the more photoelectron are generated, thus a smaller signal-to-noise ratio. The reconstructed spectrum with 3.2×10^{-7} mbar gives a better matching spectrum than the reconstruction with 1.8×10^{-7} mbar. Figure from Li et al. [2022].

Another way to improve GI reconstruction is by increasing the retardation voltage of the eToF. With a fixed incident SASE photon energy, the initial kinetic energy of the photoelectron is fixed. Increasing the retardation voltage of the eToF would reduce the kinetic energy of the flying electrons. The time taken for the slower electron to travel from the interaction point to the detector is elongated, which leads to an eToF peak with a larger bandwidth. As shown in Fig. 4.11, a broader 1s photoelectron peak is observed when increasing the retardation to push the eToF peak from ~ 50 ns to ~ 60 ns. With a fixed 0.5 ns data recording rate, more data points are collected. The PES would measure the incident SASE spectrum with more data points and smaller energy spacing. The better PES signal c obtained is helpful for improving the learning process and, as a result, achieves a better reconstruction of the spectrum.

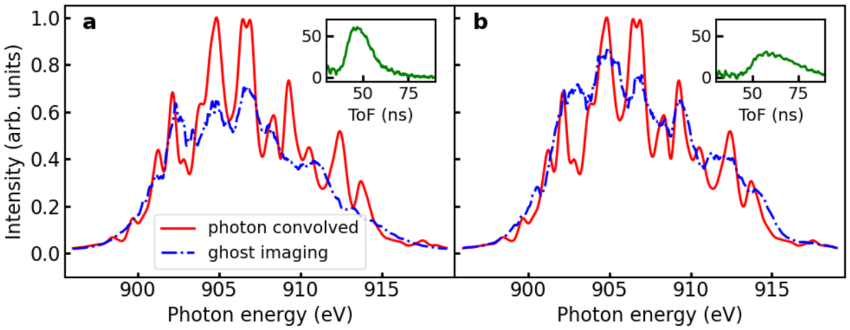

Figure 4.11: The influence of the retardation voltage on GI reconstruction method. The eToF peak is shifted to a larger value with a larger retardation voltage that slows the photoelectrons. The broad eToF peak contains more data points, which benefits the GI reconstruction. Figure from Li et al. [2022].

The GI-enhanced non-invasive characterization of the incident spectrum can increase the accuracy of the measurement of the average spectrum. Since the XFEL pulse fluctuates randomly from one shot to another, in an ATAS experiment, numerous shots are taken and the average spectrum is used to reduce the noise. The response matrix calculated by GI method produces a better calibration of the PES array, with the broadening and artifacts removed, the averaged spectrum matches much better with the averaged photon spectrum. As shown in Fig. 4.12 a, using 1000 shots of the reconstructed spectra, the average spectrum overlaps with the average photon spectrum. The reconstruction removed the noisy signals as well as the bandwidth broadening of the PES. The percentage deviation across the spectrum is limited to around 1%. The deviation remains high ($\sim 4\%$) specifically at the lower energy part of the spectrum, these could be explained by the small signals at this region due to photoelectron loss induced by the retardation voltage. Further analysis reveals that the retardation voltage should be set to leave the average kinetic energy of the photoelectrons equal to or bigger than the XFEL bandwidth. The percentage deviation drops as the number of shots n included in the averaging increases. For a random process, the noise-signal ratio is expected to decrease according to $1/\sqrt{n}$. A fit of the percentage deviation as a function of the number of shots gives $1/n^{0.45}$, which is close to 0.5 for random noise. This means that the GI reconstruction method is able to correct most of the systematic errors in the PES and push the spectrum uncertainty down to the random measurement noise regime.

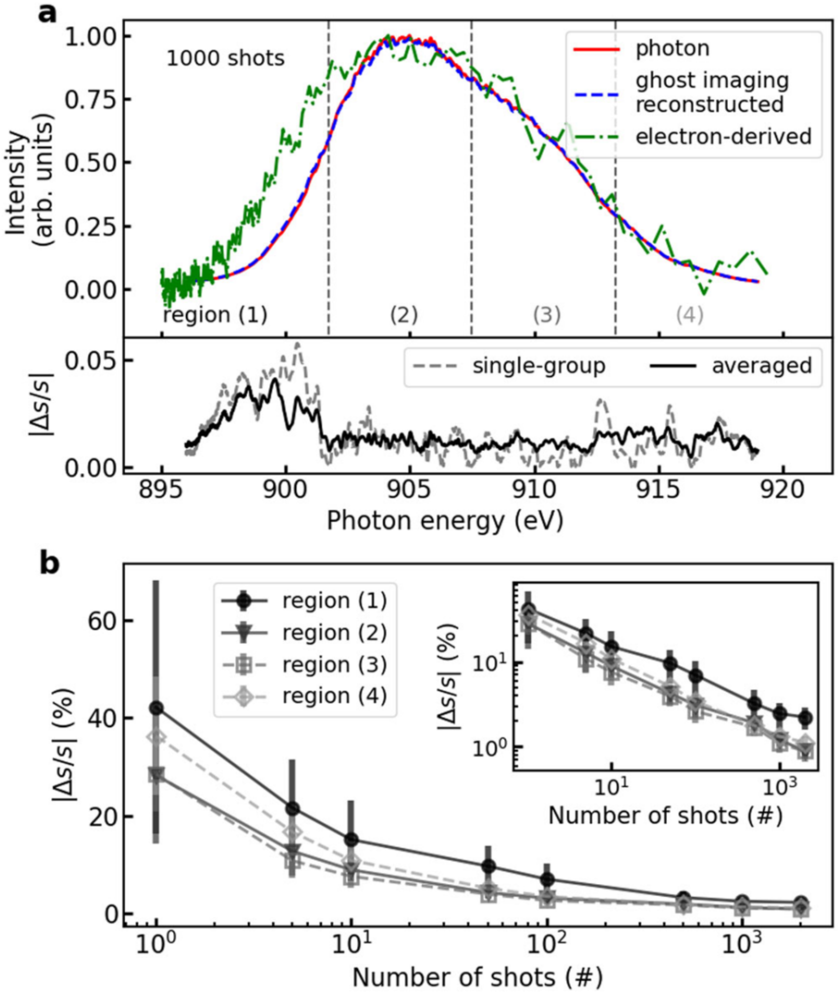

Figure 4.12: The performance of the GI reconstruction in the averaged spectrum. The GI reconstruction removes the systematic errors from the PES array and produces the averaged spectrum that overlaps with the photon spectrum. The percentage deviation as a function of number of shots n averaged is shown in (b). The inserted logarithm scale figure gives the deviation $\propto 1/n^{0.45}$, which is close to the behavior of random measurement noise $\propto 1/\sqrt{n}$. Figure from Li et al. [2022].

The GI reconstruction method demonstrated here is easy to apply for better calibration and resolution improvement in other instruments for XFEL diagnostics. For example, the newly inaugurated angle-resolved photoelectron spectroscopy (ARPES) the instrument at LCLS (Walter et al. [2021]) has eToFs three times the length of the one used in European XFEL. With this enlarged size, the PES spectrum has higher energy resolution as well as a larger number of eToF points recorded, which would greatly benefit GI reconstruction. The traditional ways of incident spectral characterization require an x-ray beamsplitter and a 2d imaging detector. The GI reconstruction method takes advantage of the existing photon diagnosis tool (PES) as both the beamsplitter and bucket detector. The 1d eToF signal is compatible with the MHz high repetition rate XFELs. With this high-resolution high repetition rate characterization tool, breakthrough is expected which enables a deeper understanding of the machine operation and allows for a fast-feedback on SASE-formation characteristics.

CHAPTER 5

SUMMARY AND OUTLOOK

In this thesis, we developed a 3D theoretical model for the resonant propagation of x-ray through a gaseous medium. The coupled time-dependent Schrodinger equation and Maxwell wave equation (TDSE-MWE) are solved. Interesting nonlinear x-ray phenomena such as self-induced transparency, self-focusing, SXRS, and XRL are investigated. An experiment studying the resonant propagation of SASE XFEL through dense neon gas is carried out at the European XFEL. The results presented here are focusing on the SXRS and XRL. The spectral covariance between transmitted incident SASE and the stimulated emission is computed, which gives an unprecedented high resolution (~ 0.2 eV) SXRS spectrum.

The supercomputer Theta at Argonne National Laboratory was employed to simulate the SXRS with SASE shots. The simulation matches with the experimental results. It also reveals that the SXRS spectrum can be further improved by calculating the covariance of Raman with the incident SASE spectrum. Therefore, we also demonstrated a new non-invasive method to characterize the single-shot SASE spectrum. The correlation between the photoelectron spectroscopy (PES) signal and the photon spectrum measured by a grating spectrometer was analyzed by the ghost-imaging formula. A response matrix of the PES array was obtained that contains detailed information about the eToFs. The response matrix is then applied to reconstruct a SASE spectrum with increased energy resolution.

In the future, the resonant propagation of strong XFEL pulses through a dense medium will be investigated from other aspects. The x-ray temporal reshaping revealed by the TDSE-MWE simulations with Gaussian pulse has motivated an experiment at LCLS. The resonant propagation of ~ 0.5 fs XLEAP pulse through a dense neon gas was studied. The temporal pulse profile after the propagation was detected by the laser streaking technique. The photoelectron ejected by the reshaped pulse is kicked into a different direction and measured by a cVMI. The pulse profile is extracted from the reconstruction algorithm.

Meanwhile, the polarization of the emission is also explored by the cVMI measurements (Li et al. [2018]).

Another experiment at European XFEL takes advantage of the newly commissioned 1D imaging spectrometer to view the emission spectrum from the side during resonant propagation. This is expected to reveal more details on the spatial reshaping of the resonant propagation. For example, the stimulated emission in the forward direction grows and becomes a competing process to the spontaneous emission/scattering and Auger decay. As a result, the spatial distribution of the scattered photons at 90 degrees might be modified. These phenomena could play an important role in resonant photon scattering imaging.

In general, the resonant propagation of strong XFEL pulses in a dense medium induces many interesting phenomena that are of fundamental interest and have the potential for wide applications.

APPENDIX A

SUPERCOMPUTER SIMULATION

Theta supercomputer in Argonne National Laboratory is used to perform the propagation simulations for 4096 SASE shots for a given set of parameters. The TDSE-MWE code is installed in folder "/lus/eagle/projects/XMultiImage/kai/new_code4_no_out_files", which requires packages: *gfortran, fftw3, OpenMPI, lapack*. Details of the packages included can be found in "Makefile".

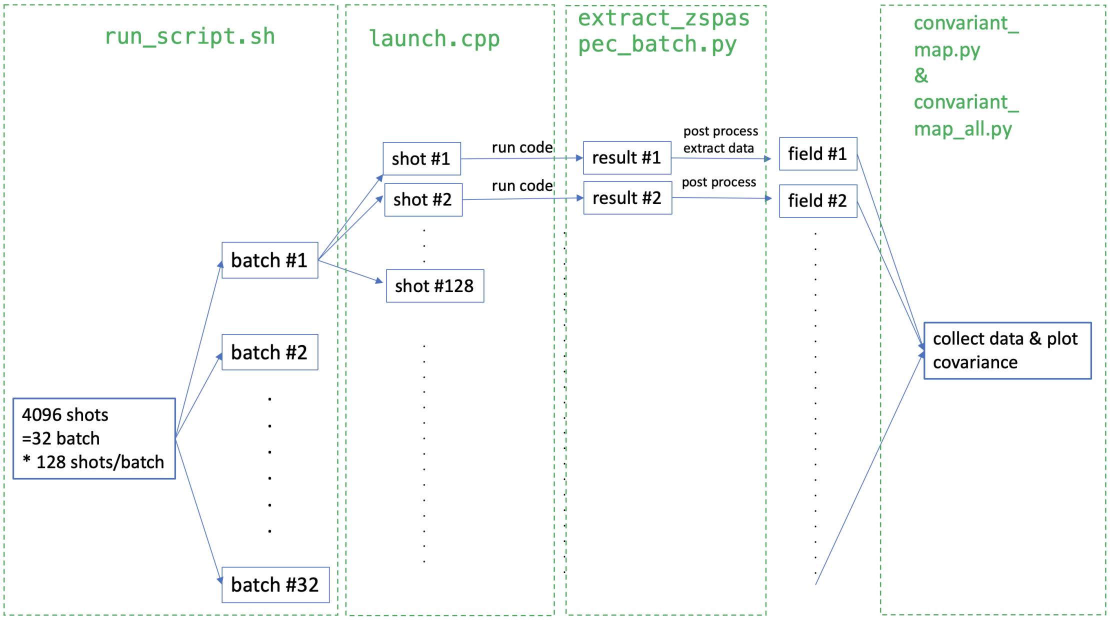

Figure A.1: The framework of the resonant propagation of SASE pulses in supercomputer and the data analysis in the local cluster.

All the calculations are done in the folder "/lus/eagle/projects/XMultiImage/kai/test". Each run contains files:

1. Run_script.sh: This is a bash file. It creates 32 parent folders (batches) with 128 shots in each folder. It copies the SASE pulse generation file "SASE_generation_new.py" to each batch folder and runs it to generate 128 shots for each batch. Basically, this file would launch the calculations with specified ranks, cores, and threads. There is

a 30 s sleep between each batch launched. This file also calls “a.out” generated by “launch.cpp”. Parameters:

   (a) -n: total num of jobs
   (b) -N: job per node
   (c) -j: num of cores per node
   (d) OMP_NUM_THREADS: threads per job

   There are 64 threads per core. Thus we should have:

   OMP_NUM_THREADS*n=n/N*4*64

   For example for each batch: 32*128=128/8*4*64

   Total threads: 32batch*128shotd/batch*32 thread/shot=131072 threads

2. launch.cpp: This is c++ file. It manages the calculation for each shot. Basically, it creates a folder for each shot according to the Openmpi setup. And then copy the SASE pulses generated to each folder. Then it automatically runs the code with specified input file “system(“/lus/eagle/projects/XMultiImage/kai/new_code4_no_out_files/PropFS_ion /lus/eagle/projects/XMultiImage/kai/test/867.5eV/0.09mJ_um2_prop/prop_7levels.in > std.txt”);”.

   This runs the code “PropFS_ion” with input file “prop_7lelvels.in”. The files should be compiled by “CC launch.cpp -DMPICH_IGNORE_CXX_SEEK”.

3. We can submit the calculation by “qsub -n 512 -t 360 -A XMultiImage -q default run_script.sh”, which use 512 ranks for 6 hours.

4. extract_zspaspec_batch1.py: After the runs are finished, we use this python3 code to extract the spectrum from the output files. This post-process would drastically shrink the size of the output files. In the code, nz is the number of propagation steps, nr is the

transverse profile grid points, and *nw* is the number of frequency points. These should be specified according to the input parameters. A folder with the name "results_npy" to store the output should be made before running the code.

5. The output spectrum data would be in the folder "results_npy". The ".npy" files are named by "field_#step_#shot.npy". The results are then copied to the local cluster (Plack or Dirac) for covariance analysis.

Plotting the covariance maps: the data is copied to the local cluster and Python codes are used to plot out the covariance maps. The python codes are in, for example, the folder "/home/oxygen/KAIL/TDSE/post_exp/SASE_prop_results/867.5eV/0.09mJ_um2_prop". Within which there are files:

1. convariant_map.py: it extracts and arranges the shots to a 2D array and saves the array for the covariance analysis.
2. convariant_map_all.py: this would take the output from the "convariant_map.py" and plot the covariance maps for each output propagation step. It also rotates the map, plots the projection, and fits the FWHMs of the peaks.

REFERENCES

Ayman F Abouraddy, Bahaa EA Saleh, Alexander V Sergienko, and Malvin C Teich. Role of entanglement in two-photon imaging. *Physical review letters*, 87(12):123602, 2001.

Sergei Aleksandrovich Akhmanov, Anatolii P Sukhorukov, and Rem Viktorovich Khokhlov. Self-focusing and diffraction of light in a nonlinear medium. *Soviet physics USPEKHI*, 10 (5):609, 1968.

E Allaria, Roberto Appio, L Badano, WA Barletta, S Bassanese, SG Biedron, A Borga, E Busetto, D Castronovo, P Cinquegrana, et al. Highly coherent and stable pulses from the fermi seeded free-electron laser in the extreme ultraviolet. *Nature Photonics*, 6(10): 699–704, 2012.

Edward Anderson, Zhaojun Bai, Christian Bischof, L Susan Blackford, James Demmel, Jack Dongarra, Jeremy Du Croz, Anne Greenbaum, Sven Hammarling, Alan McKenney, et al. *LAPACK users' guide.* SIAM, 1999.

A Arico, Giuseppe Rodriguez, and S Seatzu. Numerical solution of the nonlinear schrödinger equation, starting from the scattering data. *Calcolo*, 48:75–88, 2011.

John S Bell. On the einstein podolsky rosen paradox. *Physics Physique Fizika*, 1(3):195, 1964.

Ryan S Bennink, Sean J Bentley, and Robert W Boyd. “two-photon” coincidence imaging with a classical source. *Physical review letters*, 89(11):113601, 2002.

R Bonifacio, Federico Casagrande, and G Casati. Cooperative and chaotic transition of a free electron laser hamiltonian model. *Optics Communications*, 40(3):219–223, 1982.

Christoph Bostedt, Sébastien Boutet, David M Fritz, Zhirong Huang, Hae Ja Lee, Henrik T Lemke, Aymeric Robert, William F Schlotter, Joshua J Turner, and Garth J Williams. Linac coherent light source: The first five years. *Reviews of Modern Physics*, 88(1):015007, 2016.

Dik Bouwmeester, Jian-Wei Pan, Klaus Mattle, Manfred Eibl, Harald Weinfurter, and Anton Zeilinger. Experimental quantum teleportation. *Nature*, 390(6660):575–579, 1997.

Robert W Boyd, Alexander L Gaeta, and Enno Giese. Nonlinear optics. In *Springer Handbook of Atomic, Molecular, and Optical Physics*, pages 1097–1110. Springer, 2008.

Marianne Breinig, Mau Hsiung Chen, Gene E Ice, Fernando Parente, Bernd Crasemann, and George S Brown. Atomic inner-shell level energies determined by absorption spectrometry with synchrotron radiation. *Physical Review A*, 22(2):520, 1980.

R Hanbury Brown and Richard Q Twiss. Correlation between photons in two coherent beams of light. *Nature*, 177(4497):27–29, 1956.

David C Burnham and Raymond Y Chiao. Coherent resonance fluorescence excited by short light pulses. *Physical Review*, 188(2):667, 1969.

Stefano M Cavaletto, Christian Buth, Zoltán Harman, Elliot P Kanter, Stephen H Southworth, Linda Young, and Christoph H Keitel. Resonance fluorescence in ultrafast and intense x-ray free-electron-laser pulses. *Physical Review A*, 86(3):033402, 2012.

Stefano M Cavaletto, Daniel Keefer, and Shaul Mukamel. High temporal and spectral resolution of stimulated x-ray raman signals with stochastic free-electron-laser pulses. *Physical Review X*, 11(1):011029, 2021.

Z Chen, DJ Higley, M Beye, M Hantschmann, V Mehta, O Hellwig, A Mitra, Stefano Bonetti, M Bucher, S Carron, et al. Ultrafast self-induced x-ray transparency and loss of magnetic diffraction. *Physical review letters*, 121(13):137403, 2018.

Raymond Y Chiao, E Garmire, and Charles H Townes. Self-trapping of optical beams. *Physical review letters*, 13(15):479, 1964.

P áB Corkum and Ferenc Krausz. Attosecond science. *Nature physics*, 3(6):381–387, 2007.

Paul B Corkum. Plasma perspective on strong field multiphoton ionization. *Physical review letters*, 71(13):1994, 1993.

Robert D Cowan. *The theory of atomic structure and spectra*. Number 3. Univ of California Press, 1981.

John Crank and Phyllis Nicolson. A practical method for numerical evaluation of solutions of partial differential equations of the heat-conduction type. In *Mathematical proceedings of the Cambridge philosophical society*, volume 43, pages 50–67. Cambridge University Press, 1947.

MD Crisp. Propagation of small-area pulses of coherent light through a resonant medium. *Physical Review A*, 1(6):1604, 1970.

David AG Deacon, LR Elias, John MJ Madey, GJ Ramian, HA Schwettman, and Ti I Smith. First operation of a free-electron laser. *Physical Review Letters*, 38(16):892, 1977.

W Decking, S Abeghyan, P Abramian, A Abramsky, A Aguirre, C Albrecht, P Alou, M Altarelli, P Altmann, K Amyan, et al. A mhz-repetition-rate hard x-ray free-electron laser driven by a superconducting linear accelerator. *Nature photonics*, 14(6):391–397, 2020.

Gilles Doumy, C Roedig, S-K Son, Cosmin Ioan Blaga, AD DiChiara, Robin Santra, Nora Berrah, Christoph Bostedt, JD Bozek, PH Bucksbaum, et al. Nonlinear atomic response to intense ultrashort x rays. *Physical Review Letters*, 106(8):083002, 2011.

Taran Driver, Siqi Li, Elio G Champenois, Joseph Duris, Daniel Ratner, Thomas J Lane, Philipp Rosenberger, Andre Al-Haddad, Vitali Averbukh, Toby Barnard, et al. Attosecond transient absorption spooktroscopy: a ghost imaging approach to ultrafast absorption spectroscopy. *Physical Chemistry Chemical Physics*, 22(5):2704–2712, 2020.

MA Duguay and PM Rentzepis. Some approaches to vacuum uv and x-ray lasers. *Applied Physics Letters*, 10(12):350–352, 1967.

Joseph Duris, Siqi Li, Taran Driver, Elio G Champenois, James P MacArthur, Alberto A Lutman, Zhen Zhang, Philipp Rosenberger, Jeff W Aldrich, Ryan Coffee, et al. Tunable isolated attosecond x-ray pulses with gigawatt peak power from a free-electron laser. *Nature Photonics*, 14(1):30–36, 2020.

Gisela Eckhardt, Robert W Hellwarth, Fred J McClung, Steven E Schwarz, Daniel Weiner, and EJ Woodbury. Stimulated raman scattering from organic liquids. *Physical Review Letters*, 9(11):455, 1962.

U Eichmann, H Rottke, S Meise, J-E Rubensson, Johan Söderström, Marcus Agåker, C Såthe, M Meyer, TM Baumann, R Boll, et al. Photon-recoil imaging: Expanding the view of nonlinear x-ray physics. *Science*, 369(6511):1630–1633, 2020.

Paul Emma, R Akre, J Arthur, R Bionta, C Bostedt, J Bozek, A Brachmann, P Bucksbaum, Ryan Coffee, F-J Decker, et al. First lasing and operation of an ångstrom-wavelength free-electron laser. *nature photonics*, 4(9):641–647, 2010.

Robin Y Engel, Piter S Miedema, Diego Turenne, Igor Vaskivskyi, Günter Brenner, Siarhei Dziarzhytski, Marion Kuhlmann, Jan O Schunck, Florian Döring, Andriy Styervoyedov, et al. Parallel broadband femtosecond reflection spectroscopy at a soft x-ray free-electron laser. *Applied Sciences*, 10(19):6947, 2020.

eg PA Franken, Alan E Hill, CW Peters, and Gabriel Weinreich. Generation of optical harmonics. *Physical review letters*, 7(4):118, 1961.

Andrea Fratalocchi and Giancarlo Ruocco. Single-molecule imaging with x-ray free-electron lasers: Dream or reality? *Physical review letters*, 106(10):105504, 2011.

Matteo Frigo and Steven G Johnson. The design and implementation of fftw3. *Proceedings of the IEEE*, 93(2):216–231, 2005.

KJ Gaffney and Henry N Chapman. Imaging atomic structure and dynamics with ultrafast x-ray scattering. *science*, 316(5830):1444–1448, 2007.

HM Gibbs, SL McCall, and TNC Venkatesan. Differential gain and bistability using a sodium-filled fabry-perot interferometer. *Physical Review Letters*, 36(19):1135, 1976.

Thornton E Glover, DM Fritz, Marco Cammarata, TK Allison, Sinisa Coh, JM Feldkamp, H Lemke, D Zhu, Y Feng, RN Coffee, et al. X-ray and optical wave mixing. *Nature*, 488 (7413):603–608, 2012.

Eleftherios Goulielmakis, Zhi-Heng Loh, Adrian Wirth, Robin Santra, Nina Rohringer, Vladislav S Yakovlev, Sergey Zherebtsov, Thomas Pfeifer, Abdallah M Azzeer, Matthias F Kling, et al. Real-time observation of valence electron motion. *Nature*, 466(7307):739–743, 2010.

Aliaksei Halavanau, Andrei Benediktovitch, Alberto A Lutman, Daniel DePonte, Daniele Cocco, Nina Rohringer, Uwe Bergmann, and Claudio Pellegrini. Population inversion x-ray laser oscillator. *Proceedings of the National Academy of Sciences*, 117(27):15511–15516, 2020.

Daniel J Higley, Zhao Chen, Martin Beye, Markus Hantschmann, Alex H Reid, Virat Mehta, Olav Hellwig, Georgi L Dakovski, Ankush Mitra, Robin Y Engel, et al. Stimulated resonant inelastic x-ray scattering in a solid. *Communications Physics*, 5(1):83, 2022.

Phay J Ho and Robin Santra. Theory of x-ray diffraction from laser-aligned symmetric-top molecules. *Physical Review A*, 78(5):053409, 2008.

Phay J Ho, Christoph Bostedt, Sebastian Schorb, and Linda Young. Theoretical tracking of resonance-enhanced multiple ionization pathways in x-ray free-electron laser pulses. *Physical review letters*, 113(25):253001, 2014.

Phay J Ho, Adam EA Fouda, Kai Li, Gilles Doumy, and Linda Young. Ultraintense, ultrashort pulse x-ray scattering in small molecules. *Faraday Discussions*, 228:139–160, 2021.

Zhirong Huang and Kwang-Je Kim. Review of x-ray free-electron laser theory. *Physical Review Special Topics-Accelerators and Beams*, 10(3):034801, 2007.

Heung-Sik Kang, Chang-Ki Min, Hoon Heo, Changbum Kim, Haeryong Yang, Gyujin Kim, Inhyuk Nam, Soung Youl Baek, Hyo-Jin Choi, Geonyeong Mun, et al. Hard x-ray free-electron laser with femtosecond-scale timing jitter. *Nature Photonics*, 11(11):708–713, 2017.

EP Kanter, Bertold Kraessig, Yongjin Li, AM March, P Ho, Nina Rohringer, Robin Santra, SH Southworth, LF DiMauro, G Doumy, et al. Unveiling and driving hidden resonances with high-fluence, high-intensity x-ray pulses. *Physical review letters*, 107(23):233001, 2011.

Kwang-Je Kim. An analysis of self-amplified spontaneous emission. *Nuclear Instruments and Methods in Physics Research Section A: Accelerators, Spectrometers, Detectors and Associated Equipment*, 250(1-2):396–403, 1986a.

Kwang-Je Kim. Three-dimensional analysis of coherent amplification and self-amplified spontaneous emission in free-electron lasers. *Physical review letters*, 57(15):1871, 1986b.

Kwang-Je Kim, Yuri Shvyd'ko, and Sven Reiche. A proposal for an x-ray free-electron laser oscillator with an energy-recovery linac. *Physical review letters*, 100(24):244802, 2008.

Kwang-Je Kim, Zhirong Huang, and Ryan Lindberg. *Synchrotron radiation and free-electron lasers*. Cambridge university press, 2017.

Victor Kimberg and Nina Rohringer. Amplified x-ray emission from core-ionized diatomic molecules. *Physical Review Letters*, 110(4):043901, 2013.

Victor Kimberg and Nina Rohringer. Stochastic stimulated electronic x-ray raman spectroscopy. *Structural Dynamics*, 3(3), 2016.

Victor Kimberg, Song Bin Zhang, and Nina Rohringer. X-ray lasing in the co molecule. *Journal of Physics B: Atomic, Molecular and Optical Physics*, 46(16):164017, 2013.

Victor Kimberg, Song Bin Zhang, and Nina Rohringer. X-ray lasing in diatomic molecules. In *Journal of Physics: Conference Series*, volume 488, page 012025. IOP Publishing, 2014.

Victor Kimberg, Alvaro Sanchez-Gonzalez, Laurent Mercadier, Clemens Weninger, Alberto Lutman, Daniel Ratner, Ryan Coffee, Maximilian Bucher, Melanie Mucke, Marcus Agåker, et al. Stimulated x-ray raman scattering–a critical assessment of the building block of nonlinear x-ray spectroscopy. *Faraday discussions*, 194:305–324, 2016.

AM Kondratenko and EL Saldin. Generating of coherent radiation by a relativistic electron beam in an ondulator. *Part. Accel.*, 10:207–216, 1980.

Peter M Kraus, Benoît Mignolet, Denitsa Baykusheva, A Rupenyan, Lubos Hornỳ, Emmanuel F Penka, Guido Grassi, Oleg I Tolstikhin, Johannes Schneider, Frank Jensen, et al. Measurement and laser control of attosecond charge migration in ionized iodoacetylene. *Science*, 350(6262):790–795, 2015.

Thomas Kroll, Clemens Weninger, Roberto Alonso-Mori, Dimosthenis Sokaras, Diling Zhu, Laurent Mercadier, Vinay P Majety, Agostino Marinelli, Alberto Lutman, Marc W Guetg, et al. Stimulated x-ray emission spectroscopy in transition metal complexes. *Physical review letters*, 120(13):133203, 2018.

Thomas Kroll, Clemens Weninger, Franklin D Fuller, Marc W Guetg, Andrei Benediktovitch, Yu Zhang, Agostino Marinelli, Roberto Alonso-Mori, Andy Aquila, Mengning Liang, et al. Observation of seeded mn k β stimulated x-ray emission using two-color x-ray free-electron laser pulses. *Physical review letters*, 125(3):037404, 2020.

Philipp Kukura, David W McCamant, and Richard A Mathies. Femtosecond stimulated raman spectroscopy. *Annu. Rev. Phys. Chem.*, 58:461–488, 2007.

Paul G Kwiat, Klaus Mattle, Harald Weinfurter, Anton Zeilinger, Alexander V Sergienko, and Yanhua Shih. New high-intensity source of polarization-entangled photon pairs. *Physical Review Letters*, 75(24):4337, 1995.

Joakim Laksman, Jens Buck, Leif Glaser, Marc Planas, Florian Dietrich, Jia Liu, Theophilos Maltezopoulos, Frank Scholz, Jörn Seltmann, Gregor Hartmann, et al. Commissioning of a photoelectron spectrometer for soft x-ray photon diagnostics at the european xfel. *Journal of synchrotron radiation*, 26(4):1010–1016, 2019.

Jie Li, Jian Lu, Andrew Chew, Seunghwoi Han, Jialin Li, Yi Wu, He Wang, Shambhu Ghimire, and Zenghu Chang. Attosecond science based on high harmonic generation from gases and solids. *Nature Communications*, 11(1):2748, 2020a.

Kai Li, Marie Labeye, Phay J Ho, Mette B Gaarde, and Linda Young. Resonant propagation of x rays from the linear to the nonlinear regime. *Physical Review A*, 102(5):053113, 2020b.

Kai Li, Dimitris Koulentianos, Gilles Doumy, Linda Young, Mette Gaarde, Zhaoheng Guo, James Cryan, and Agostino Marinelli. Temporal profile reshaping of high-intensity attosecond x-ray pulses by resonant propagation through dense gas. *Bulletin of the American Physical Society*, 66, 2021a.

Kai Li, Joakim Laksman, Tommaso Mazza, Gilles Doumy, Dimitris Koulentianos, Alessandra Picchiotti, Svitozar Serkez, Nina Rohringer, Markus Ilchen, Michael Meyer, et al. Ghost-imaging-enhanced noninvasive spectral characterization of stochastic x-ray free-electron-laser pulses. *Communications Physics*, 5(1):191, 2022.

Siqi Li, Zhaoheng Guo, Ryan N Coffee, Kareem Hegazy, Zhirong Huang, Adi Natan, Timur Osipov, Dipanwita Ray, Agostino Marinelli, and James P Cryan. Characterizing isolated attosecond pulses with angular streaking. *Optics express*, 26(4):4531–4547, 2018.

Siqi Li, Taran Driver, Oliver Alexander, Bridgette Cooper, Douglas Garratt, Agostino Marinelli, James P Cryan, and Jonathan P Marangos. Time-resolved pump–probe spectroscopy with spectral domain ghost imaging. *Faraday Discussions*, 228:488–501, 2021b.

Junzi Liu, Yue Shen, Ayush Asthana, and Lan Cheng. Two-component relativistic coupled-cluster methods using mean-field spin-orbit integrals. *The Journal of Chemical Physics*, 148(3), 2018.

Z-H Loh, G Doumy, C Arnold, Ludvig Kjellsson, SH Southworth, A Al Haddad, Y Kumagai, M-F Tu, PJ Ho, AM March, et al. Observation of the fastest chemical processes in the radiolysis of water. *Science*, 367(6474):179–182, 2020.

AA Lutman, Y Ding, Y Feng, Z Huang, Marc Messerschmidt, J Wu, and J Krzywinski. Femtosecond x-ray free electron laser pulse duration measurement from spectral correlation function. *Physical Review Special Topics-Accelerators and Beams*, 15(3):030705, 2012.

John MJ Madey. Stimulated emission of bremsstrahlung in a periodic magnetic field. *Journal of Applied Physics*, 42(5):1906–1913, 1971.

Theodore H Maiman et al. Stimulated optical radiation in ruby. 1960.

Tommaso Mazza, Thomas M Baumann, Rebecca Boll, Alberto De Fanis, Patrik Grychtol, Markus Ilchen, Jacobo Montaño, Valerija Music, Yevheniy Ovcharenko, Nils Rennhack, et al. The beam transport system for the small quantum systems instrument at the european xfel: optical layout and first commissioning results. *Journal of Synchrotron Radiation*, 30(2), 2023.

Samuel Leverte McCall and Erwin L Hahn. Self-induced transparency by pulsed coherent light. *Physical Review Letters*, 18(21):908, 1967.

Katsumi Midorikawa. Ultrafast dynamic imaging. *Nature Photonics*, 5(11):640–641, 2011.

Christopher J Milne, Thomas Schietinger, Masamitsu Aiba, Arturo Alarcon, Jürgen Alex, Alexander Anghel, Vladimir Arsov, Carl Beard, Paul Beaud, Simona Bettoni, et al. Swissfel: the swiss x-ray free electron laser. *Applied Sciences*, 7(7):720, 2017.

RW Minck, RW Terhune, and WG Rado. Laser-stimulated raman effect and resonant four-photon interactions in gases h2, d2, and ch4. *Applied Physics Letters*, 3(10):181–184, 1963.

Alfred Müller, Dietrich Bernhardt, Alexander Borovik, Ticia Buhr, Jonas Hellhund, Kristof Holste, AL David Kilcoyne, Stephan Klumpp, Michael Martins, Sandor Ricz, et al. Photoionization of ne atoms and ne+ ions near the k edge: Precisionspectroscopy and absolute cross-sections. *The Astrophysical Journal*, 836(2):166, 2017.

Heinz-Dieter Nuhn. Linac coherent light source (lcls) conceptual design report. Technical report, SLAC National Accelerator Lab., Menlo Park, CA (United States), 2002.

Jordan T O'Neal, Elio G Champenois, Solène Oberli, Razib Obaid, Andre Al-Haddad, Jonathan Barnard, Nora Berrah, Ryan Coffee, Joseph Duris, Gediminas Galinis, et al. Electronic population transfer via impulsive stimulated x-ray raman scattering with attosecond soft-x-ray pulses. *Physical review letters*, 125(7):073203, 2020.

Claudio Pellegrini and S Reiche. The development of x-ray free-electron lasers. *IEEE Journal of Selected Topics in Quantum Electronics*, 10(6):1393–1404, 2004.

Daniele Pelliccia, Alexander Rack, Mario Scheel, Valentina Cantelli, and David M Paganin. Experimental x-ray ghost imaging. *Physical review letters*, 117(11):113902, 2016.

Yoann Pertot, Cédric Schmidt, Mary Matthews, Adrien Chauvet, Martin Huppert, Vit Svoboda, Aaron Von Conta, Andres Tehlar, Denitsa Baykusheva, Jean-Pierre Wolf, et al. Time-resolved x-ray absorption spectroscopy with a water window high-harmonic source. *Science*, 355(6322):264–267, 2017.

Thomas Pfeifer, Yuhai Jiang, Stefan Düsterer, Robert Moshammer, and Joachim Ullrich. Partial-coherence method to model experimental free-electron laser pulse statistics. *Optics letters*, 35(20):3441–3443, 2010.

D Ratner, JP Cryan, TJ Lane, S Li, and G Stupakov. Pump-probe ghost imaging with sase fels. *Physical Review X*, 9(1):011045, 2019.

Sven Reiche. Genesis 1.3: a fully 3d time-dependent fel simulation code. *Nuclear Instruments and Methods in Physics Research Section A: Accelerators, Spectrometers, Detectors and Associated Equipment*, 429(1-3):243–248, 1999.

Nina Rohringer. X-ray raman scattering: A building block for nonlinear spectroscopy. *Philosophical Transactions of the Royal Society A*, 377(2145):20170471, 2019.

Nina Rohringer and Richard London. Atomic inner-shell x-ray laser pumped by an x-ray free-electron laser. *Physical Review A*, 80(1):013809, 2009.

Nina Rohringer and Robin Santra. X-ray nonlinear optical processes using a self-amplified spontaneous emission free-electron laser. *Physical Review A*, 76(3):033416, 2007.

Nina Rohringer and Robin Santra. Multichannel coherence in strong-field ionization. *Physical Review A*, 79(5):053402, 2009.

Nina Rohringer, Duncan Ryan, Richard A London, Michael Purvis, Felicie Albert, James Dunn, John D Bozek, Christoph Bostedt, Alexander Graf, Randal Hill, et al. Atomic inner-shell x-ray laser at 1.46 nanometres pumped by an x-ray free-electron laser. *Nature*, 481(7382):488–491, 2012.

Dilano Saldin. Ghost imaging with x rays. *Physics*, 9:103, 2016.

Jozsef Seres, Enikö Seres, Aart J Verhoef, Gabriel Tempea, Christina Streli, Peter Wobrauschek, Vladislav Yakovlev, Armin Scrinzi, Christian Spielmann, and Ferenc Krausz. Source of coherent kiloelectronvolt x-rays. *Nature*, 433(7026):596–596, 2005.

Svitozar Serkez, Winfried Decking, Lars Froehlich, Natalia Gerasimova, Jan Grünert, Marc Guetg, Marko Huttula, Suren Karabekyan, Andreas Koch, Vitali Kocharyan, et al. Opportunities for two-color experiments in the soft x-ray regime at the european xfel. *Applied Sciences*, 10(8):2728, 2020.

Claude E. Shannon. A mathematical theory of communication. *The Bell System Technical Journal*, 27(3):379–423, 1948. doi:10.1002/j.1538-7305.1948.tb01338.x.

YR Shen. Surface properties probed by second-harmonic and sum-frequency generation. *Nature*, 337(6207):519–525, 1989.

Sharon Shwartz, Matthias Fuchs, JB Hastings, Y Inubushi, T Ishikawa, T Katayama, DA Reis, T Sato, K Tono, M Yabashi, et al. X-ray second harmonic generation. *Physical review letters*, 112(16):163901, 2014.

Anthony E Siegman. *Lasers*. University science books, 1986.

Joachim Stöhr and Andreas Scherz. Creation of x-ray transparency of matter by stimulated elastic forward scattering. *Physical review letters*, 115(10):107402, 2015.

DV Strekalov, AV Sergienko, DN Klyshko, and YH Shih. Observation of two-photon "ghost" interference and diffraction. *Physical review letters*, 74(18):3600, 1995.

Donna Strickland and Gerard Mourou. Compression of amplified chirped optical pulses. *Optics communications*, 55(6):447–449, 1985.

S Suckewer and P Jaegle. X-ray laser: past, present, and future. *Laser Physics Letters*, 6 (6):411–436, 2009.

Jamal Suleiman. Single and double electron excitation transition rates and oscillator strengths calculations in the study of the x-ray absorption spectrum of neon. *Physica Scripta*, 98(1):015405, 2023.

Yu-Ping Sun, Ji-Cai Liu, Chuan-Kui Wang, and Faris Gel'mukhanov. Propagation of a strong x-ray pulse: Pulse compression, stimulated raman scattering, amplified spontaneous emission, lasing without inversion, and four-wave mixing. *Physical Review A*, 81(1):013812, 2010.

Kenji Tamasaku, Eiji Shigemasa, Yuichi Inubushi, Tetsuo Katayama, Kei Sawada, Hirokatsu Yumoto, Haruhiko Ohashi, Hidekazu Mimura, Makina Yabashi, Kazuto Yamauchi, et al. X-ray two-photon absorption competing against single and sequential multiphoton processes. *Nature Photonics*, 8(4):313–316, 2014.

Albert C Thompson, Douglas Vaughan, et al. *X-ray data booklet*, volume 8. Lawrence Berkeley National Laboratory, University of California Berkeley, CA, 2001.

Thomas Tschentscher, Christian Bressler, Jan Grünert, Anders Madsen, Adrian P Mancuso, Michael Meyer, Andreas Scherz, Harald Sinn, and Ulf Zastrau. Photon beam transport and scientific instruments at the european xfel. *Applied Sciences*, 7(6):592, 2017.

Joachim Ullrich, Artem Rudenko, and Robert Moshammer. Free-electron lasers: New avenues in molecular physics and photochemistry. *Annual review of physical chemistry*, 63: 635–660, 2012.

Giovanni Vannucci and Malvin Carl Teich. Computer simulation of superposed coherent and chaotic radiation. *Applied optics*, 19(4):548–553, 1980.

Jens Viefhaus, Frank Scholz, Sascha Deinert, Leif Glaser, Markus Ilchen, Jörn Seltmann, Peter Walter, and Frank Siewert. The variable polarization xuv beamline p04 at petra iii: Optics, mechanics and their performance. *Nuclear Instruments and Methods in Physics Research Section A: Accelerators, Spectrometers, Detectors and Associated Equipment*, 710:151–154, 2013.

Peter Walter, Andrei Kamalov, Averell Gatton, Taran Driver, Dileep Bhogadi, J-C Castagna, Xianchao Cheng, Hongliang Shi, Razib Obaid, James Cryan, et al. Multi-resolution electron spectrometer array for future free-electron laser experiments. *Journal of Synchrotron Radiation*, 28(5):1364–1376, 2021.

Clemens Weninger and Nina Rohringer. Stimulated resonant x-ray raman scattering with incoherent radiation. *Physical Review A*, 88(5):053421, 2013.

Clemens Weninger and Nina Rohringer. Transient-gain photoionization x-ray laser. *Physical Review A*, 90(6):063828, 2014.

Clemens Weninger, Michael Purvis, Duncan Ryan, Richard A London, John D Bozek, Christoph Bostedt, Alexander Graf, Gregory Brown, Jorge J Rocca, and Nina Rohringer. Stimulated electronic x-ray raman scattering. *Physical review letters*, 111(23):233902, 2013.

Norman Wright and Maurice C Newstein. Self-focusing of coherent pulses. *Optics Communications*, 9(1):8–13, 1973.

B Wu, T Wang, CE Graves, D Zhu, WF Schlotter, JJ Turner, O Hellwig, Z Chen, HA Dürr, Andreas Scherz, et al. Elimination of x-ray diffraction through stimulated x-ray transmission. *Physical review letters*, 117(2):027401, 2016.

Makina Yabashi, Hitoshi Tanaka, and Tetsuya Ishikawa. Overview of the sacla facility. *Journal of synchrotron radiation*, 22(3):477–484, 2015.

Linda Young, Elliot P Kanter, Bertold Kraessig, Yongjin Li, AM March, ST Pratt, Robin Santra, SH Southworth, Nina Rohringer, LF DiMauro, et al. Femtosecond electronic response of atoms to ultra-intense x-rays. *Nature*, 466(7302):56–61, 2010.

Hong Yu, Ronghua Lu, Shensheng Han, Honglan Xie, Guohao Du, Tiqiao Xiao, and Daming Zhu. Fourier-transform ghost imaging with hard x rays. *Physical review letters*, 117(11): 113901, 2016.

L-H Yu, M Babzien, I Ben-Zvi, LF DiMauro, A Doyuran, W Graves, E Johnson, S Krinsky, R Malone, I Pogorelsky, et al. High-gain harmonic-generation free-electron laser. *Science*, 289(5481):932–934, 2000.

Yu Zhang, Jason D Biggs, Niranjan Govind, and Shaul Mukamel. Monitoring long-range electron transfer pathways in proteins by stimulated attosecond broadband x-ray raman spectroscopy. *The journal of physical chemistry letters*, 5(21):3656–3661, 2014.

Zhentang Zhao, Dong Wang, Qiang Gu, Lixin Yin, Guoping Fang, Ming Gu, Yongbin Leng, Qiaogen Zhou, Bo Liu, Chuanxiang Tang, et al. Sxfel: a soft x-ray free electron laser in china. *Synchrotron Radiation News*, 30(6):29–33, 2017.

Diling Zhu, Marco Cammarata, Jan M Feldkamp, David M Fritz, Jerome B Hastings, Sooheyong Lee, Henrik T Lemke, Aymeric Robert, James L Turner, and Yiping Feng. A single-shot transmissive spectrometer for hard x-ray free electron lasers. *Applied Physics Letters*, 101(3), 2012.

ZY Zhu, ZT Zhao, D Wang, Z Liu, RX Li, LX Yin, and ZH Yang. Sclf: an 8-gev cw scrf linac-based x-ray fel facility in shanghai. *Proceedings of the FEL2017, Santa Fe, NM, USA*, pages 20–25, 2017.

Alfred Zong, Bailey R Nebgen, Sheng-Chih Lin, Jacob A Spies, and Michael Zuerch. Emerging ultrafast techniques for studying quantum materials. *Nature Reviews Materials*, 8(4): 224–240, 2023.